UNCLASSIFIED

AD NUMBER
ADB012128
LIMITATION CHANGES

TO:

Approved for public release; distribution is unlimited.

FROM:

Distribution authorized to U.S. Gov't. agencies only; Test and Evaluation; SEP 1975. Other requests shall be referred to Air Force Avionics Laboratory, AFAL/RWM-GPS, Wright-Patterson AFB, OH 45433.

AUTHORITY

WL/AFSC (IST) ltr, 26 Apr 1991

THIS PAGE IS UNCLASSIFIED

AFAL-TR-75-156

INVESTIGATION OF CRITICAL ISSUES FOR ARMY USERS OF THE NAVSTAR GLOBAL POSITIONING SYSTEM

THE ANALYTIC SCIENCES CORPORATION

Technical Report AFAL-TR-75-156

Final Report for Period October 1974 - June 1975

May 1976

Air Force Avionics Laboratory
Air Force Wright Aeronautical Laboratories
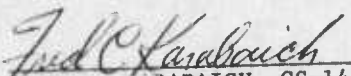Air Force Systems Command
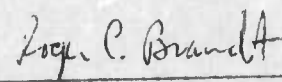Wright-Patterson Air Force Base
Ohio 45433

AD No.

DDC FILE COPY

ADR012128

DDC
RECEIVED
JUL 15 1976
A

This technical report has been reviewed and is approved for publication.

FRED C. KARABAICH, GS-14
AFAL/RWM-GPS
Project Engineer

ROGER C. BRANDT, Major, USAF
Program Manager, ADP-666A

CHARLES L. HUDSON, Lt Col. USAF.
Acting Chief, Reconnaissance and
Weapon Delivery Division

AIR FORCE - 9 JUNE 76 - 100

UNCLASSIFIED

REPORT DOCUMENTATION PAGE	READ INSTRUCTIONS BEFORE COMPLETING FORM

1. REPORT NUMBER	2. GOVT ACCESSION NO.	3. RECIPIENT'S CATALOG NUMBER
AFAL-TR-75-156		

4. TITLE (and Subtitle)	5. TYPE OF REPORT & PERIOD COVERED
Investigation of Critical Issues for Army Users of the NAVSTAR Global Positioning System.	Final Report. October 1974-June 1975
	6. PERFORMING ORG. REPORT NUMBER
	TASC — TR-589

7. AUTHOR(s)	8. CONTRACT OR GRANT NUMBER(s)
Robert H. Pyle Gregory L. Mealy	F33615-75-C-1112

9. PERFORMING ORGANIZATION NAME AND ADDRESS	10. PROGRAM ELEMENT, PROJECT, TASK AREA & WORK UNIT NUMBERS
The Analytic Sciences Corporation Six Jacob Way Reading, Massachusetts 01867	Advanced Development Program 666A, Task 2

11. CONTROLLING OFFICE NAME AND ADDRESS	12. REPORT DATE
Air Force Avionics Laboratory (RWM-GPS) Air Force Systems Command Wright-Patterson AFB, Ohio 45433	May 1976
	13. NUMBER OF PAGES
	170

14. MONITORING AGENCY NAME & ADDRESS(if different from Controlling Office)	15. SECURITY CLASS. (of this report)
Army Satellite Communications Agency Fort Monmouth, New Jersey 07703	Unclassified
	15a. DECLASSIFICATION/DOWNGRADING SCHEDULE

16. DISTRIBUTION STATEMENT (of this Report)

Distribution limited to U.S. Government agencies only; report contains information on test and evaluation of military hardware; September 1975. Other requests for this document must be referred to the Air Force Avionics Laboratory, AFAL/RWM-GPS, Wright-Patterson Air Force Base, Ohio 45433."

17. DISTRIBUTION STATEMENT (of the abstract entered in Block 20, if different from Report)

18. SUPPLEMENTARY NOTES

19. KEY WORDS (Continue on reverse side if necessary and identify by block number)

Satellite Navigation, Global Positioning System, Directional Antennas, ECM, ECCM, Receiver Clock Models, Error Analysis

AFAL-TR-74-294

20. ABSTRACT (Continue on reverse side if necessary and identify by block number)

This report addresses critical issues relative to the projected performance of Army users of the NAVSTAR Global Positioning System (GPS) in a battelfield environment. This study represents a continuation of an earlier Army user performance analysis conducted by TASC and reported in Ref. 1. An assessment is provided of the practicality and navigation performance obtainable with the deployment of directional receiver antennas by the Army.

DD FORM 1473 EDITION OF 1 NOV 65 IS OBSOLETE

UNCLASSIFIED

404 565

20.

manpack user. A realistic assessment of the vulnerability of this user to electronic jamming from both ground-based and airborne jammers is also provided. Several techniques available to the user for countering a jamming threat are discussed and evaluated. Lastly, an assessment is presented of the unique error effects of receiver crystal oscillators (clocks) on user navigation performance. Error effects considered in this study include those due to vibration, shock, warm-up, temperature variations and acceleration on the clock pattern.

FOREWORD

iii

TABLE OF CONTENTS

TABLE OF CONTENTS (Continued)

Page
No.

LIST OF FIGURES

LIST OF FIGURES (Continued)

LIST OF FIGURES (Continued)

LIST OF TABLES

1.   INTRODUCTION

A prevalent problem encountered by Army commanders is the lack of precise information on the location of their troops and equipment as well as that of adversary in a battlefield environment. The projected NAVSTAR Global Positioning System (GPS) is capable of providing this location information accurately through use of passive receiving equipment by the Army troops. However, as depicted in Fig. 1-1, there are several potential problems associated with the use of GPS in a battlefield environment. These problems include attenuation of the navigation signal by heavy foliage, intentional jamming of the navigation signal by the adversary and adverse environmental conditions affecting user equipment operation and navigation accuracy.

R-18435
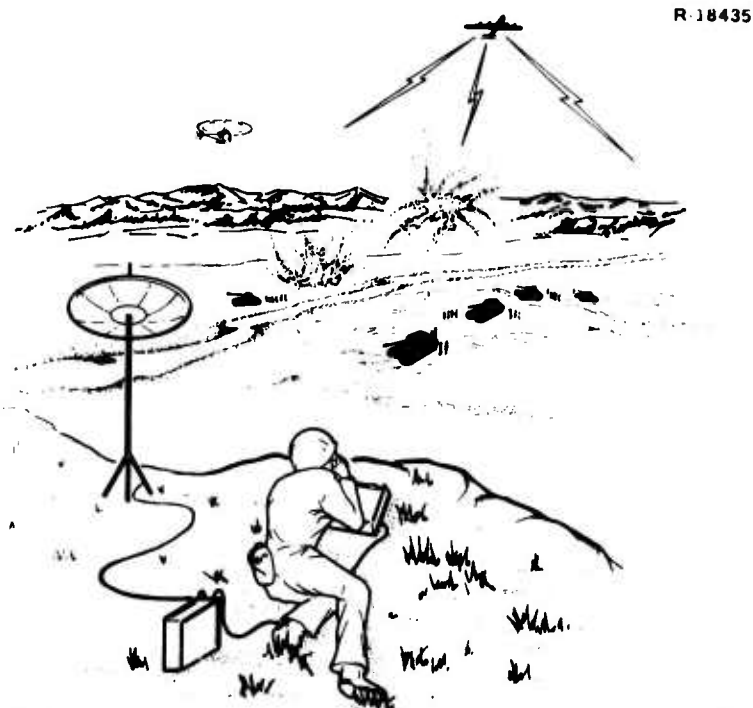
Figure 1-1   Army GPS Users in a Jamming Environment

This report addresses these problems. Included are assessments of the degradation in user location accuracy that may be experienced in a battlefield environment as well as actions which may be taken to alleviate or counteract these problems when encountered. The specific goals of this study are to:

- Assess the impact on the Army manpack GPS user navigation performance of the use of directional receiver antennas.

- Assess the vulnerability of the Army GPS user to electronic warfare and consider methods of countering this threat.

- Assess the impact on Army airborne GPS user navigation performance of the receiver clock crystal oscillator errors induced by the environment.

This study is an extension of a previous study of the Army GPS user performance described in Ref. 1. This reference is frequently cited in the present work and, wherever possible, the same notation is used.

This study uses analysis tools developed under previous studies. In particular, the previously developed GPS Direct Simulation (DSIM) computer program (Ref. 2) was used here for the assessment of user navigation performance in both the directional antenna and environmental clock modeling studies.

1.1 BACKGROUND

The development of a high-accuracy, world-wide, 24-hour navigation satellite system has been in progress for over a decade. Extensive studies and tests have proven the feasibility of the concept and that it could be configured

2

within the capabilities of current technologies. In 1973, TASC initiated a study of the performance of Army users of the GPS (Ref. 1). That effort consisted of the evaluation of the relevance of previous Air Force navigation satellite test programs to Army users, an analysis of the performance of selected Army users of the GPS, and a study of the impact of the GPS signal structure on Army users including consideration of vulnerability to electronic warfare.

The present study is an extension of the previous Army user study with consideration of the impact on navigation performance of directional antennas and adverse environments. The vulnerability study is extended with a more complete model of the propagation environment and consideration of possible countering techniques. The investigation of the environmental effects on receiver crystal oscillators is a new topic.

1.2   THE NAVSTAR GLOBAL POSITIONING SYSTEM

The NAVSTAR Global Positioning System is a satellite-based passive radio navigation system that, in its final operational phase, will be capable of providing highly accurate navigation information to properly equipped users on a continuous world-wide basis. The principal elements of the system are a set of satellites that transmit navigation signals, a network of ground monitoring stations and the various users. The GPS is to evolve in three phases with the final phase (Phase III) consisting of 24 satellites in a 3 x 8 (three planes, eight satellites per plane) constellation with each satellite in a 12-hour (altitude of 3.16 earth radii) orbit inclined 63 deg. The satellite-to-satellite in-plane spacing is uniform (45 deg spacing)

3

with a 15 deg inter-plane phasing. The plane-to-plane angular spacing is 120 deg.

The ground monitoring system tracks the satellites and computes the ephemerides of each satellite. These satellite ephemerides and related data are then "uploaded" to each satellite once a day for subsequent transmission to the users.

The satellites transmit coded navigation signals which enable a user to make range measurements between himself and the satellite. These measurements are made by comparing the time of arrival of the navigation signal with an assumed time of transmission as determined by the user's reference clock. This time difference is converted into a range measurement by means of a known propagation constant. The user's reference clock is not perfectly synchronized with the clock in the satellite that is used to generate the navigation signal. Thus, this range measurement differs from the geometrical range between user and satellite by the relative offset or bias between the user and satellite clock. The measured range is called "pseudo-range" to denote this fact.

The user obtains a three-dimensional position fix by making at least four independent pseudo-range measurements (to four separate satellites). These four measurements permit the simultaneous determination of the three unknown position coordinates and the unknown clock offset. In an analogous manner, velocity estimates are obtained from pseudo-range-rate measurements by extracting the doppler shift of the navigation signal carrier frequency. In order for the user to convert these measurements to position and velocity estimates, he must know the position and velocity of those satellites originating the navigation signals

4

used in the measurements. This information is sent by the satellites to the users via the navigation signals.

1.3 REPORT OVERVIEW

The major results of this study are contained in Chapters 2, 3 and 4. The appendices contain additional details of the mathematical models and analysis techniques used in the study.

The assessment of the impact of directional receiver antennas on Army user navigation performance is presented in Chapter 2. The number of satellites visible with directional antennas of different beamwidths is discussed first. Then performance projections are presented for users employing directional antennas. Next, the design of directional antennas using an array of discrete antenna elements is discussed. The optimum method of eliminating directional interference is presented along with theoretical performance projections. Applicability to the GPS manpack user is discussed. Finally, some antenna deployment procedures are considered.

The results of the vulnerability study are presented in Chapter 3. The threat model and scenario are outlined with a brief discussion of the propagation loss model. Threat countering techniques are then considered and their effectiveness evaluated. Finally, an evaluation of Army GPS user vulnerability to electronic warfare is presented for the threat model and scenario previously outlined. An assessment of the relative impact of the threat countering techniques is also made.

The effects of the environment on the user receiver, in particular, the receiver crystal oscillator is

5

discussed in Chapter 4. The environmental clock model is presented along with user performance projections for users employing this clock.

The report is summarized and some conclusions presented in Chapter 5. Several suggestions and recommendations, based on insights gained while generating the data of the previous chapters, are presented.

Characteristics of directional antennas are considered in Appendix A with emphasis placed on parabolic-type antennas. The GPS Phase III configuration and performance data used in the user performance projections are discussed in Appendix B. The error modeling technique used in developing a model for intrinsic clock stability is discussed in Appendix C. Details of the propagation loss model used in the vulnerability evaluation study are presented in Appendix D.

2.   DIRECTIONAL RECEIVER ANTENNAS

        GPS users may use directional antennas in order
to overcome some of the problems which could be encountered
in a battlefield environment. In particular, they can be
used to increase the received signal strength when operating
under heavy foliage and to reduce interfering signals such
as intentional signal jamming. However, directional antennas
restrict the user's visibility to satellites and thus may de-
grade his navigation accuracy and/or increase the time re-
quired to obtain high navigational accuracy.

        This chapter considers the use of directional re-
ceiving antennas by GPS users. A discussion of the number
of satellites visible with directional antennas of various
beamwidths and orientations is presented in Section 2.1.
Performance projections for users with directional antennas
are presented in Section 2.2. The results presented in this
section illustrate the advantages of using Kalman filters to
perform the processing for computing user position. Null
and beam steering techniques are discussed in Section 2.3.
A general theoretical discussion of electronic steering is
presented as well as an illustration of the performance
that can be expected with simple antenna arrays. Finally,
in Section 2.4, antenna deployment procedures are discussed
for typical manpack GPS user scenarios. Discussion of the
directional antenna characteristics used in this chapter
and the equations relating the various antenna parameters
are presented in Appendix A.

2.1 SATELLITE VISIBILITY WITH DIRECTIONAL ANTENNAS

The satellites that are visible to a GPS user depend not only upon his location and antenna orientation, but also upon the satellite configuration. This study uses the GPS Phase III satellite configuration that was discussed briefly in Section 1.2. Further details of this satellite configuration are presented in Appendix B.

The number of satellites visible to users with vertical boresight (or main lobe) directional antennas for various beamwidths is illustrated in Section 2.1.1. These satellite visibility results are extended to off-vertical boresight directional antennas in Section 2.1.2.

2.1.1 SATELLITE VISIBILITY WITH VERTICAL BORESIGHT ANTENNAS

The number of satellites visible to a GPS user with a directional receiving antenna are determined by his longitude and latitude, antenna orientation, and the time of day. Also, as the user makes measurements, visible satellites may drop from view and/or new satellites appear. In order to reduce the number of variables involved but still provide some idea of satellite visibility, the average number of satellites visible to users at different latitudes with vertical boresight directional antennas was computed. This was accomplished by averaging over a 24-hour period the number of satellites that a user could "see" at different latitudes with different directional antenna beamwidths. The results of this computation are illustrated in Fig. 2.1-1. These results indicate that the antenna beamwidth must be approximately 140 deg (or greater) in order to insure the visibility of four satellites simultaneously. This confirms similar results reported in Ref. 1. For users at latitudes

8

R-16008a
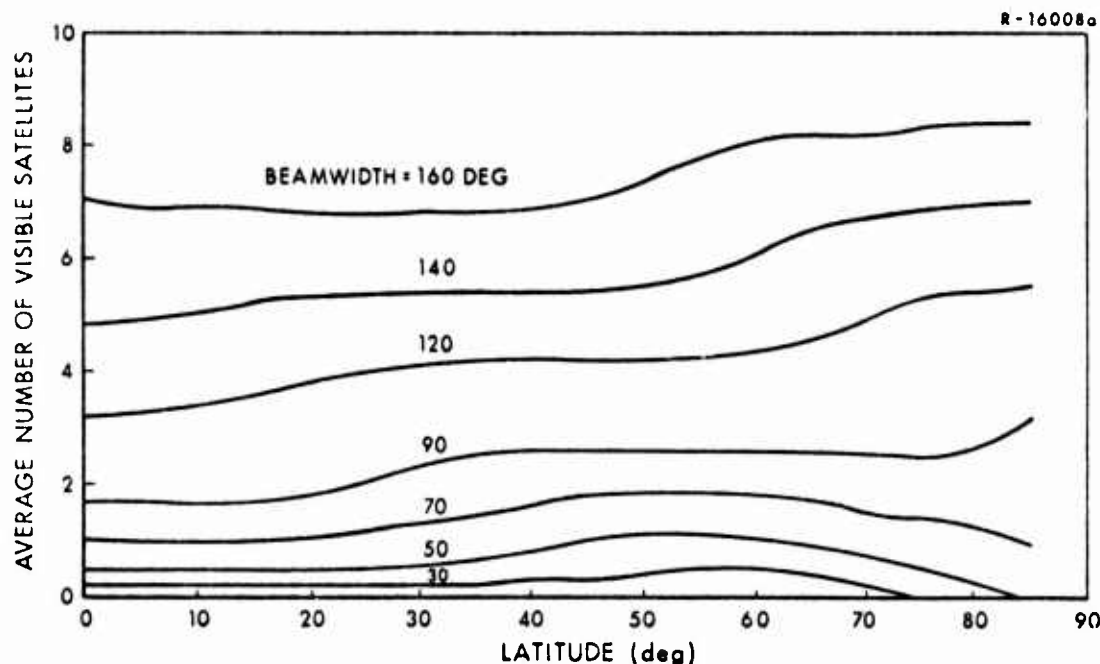
Figure 2.1-1   Satellite Visibility of Vertical
Boresight Directional Antennas

greater than 25 deg, a 120 deg beamwidth directional antenna
could be deployed and still retain visibility to four satel-
lites.

As can be expected, the narrower the beamwidth, the
fewer the satellites. Thus, a beamwidth of 90 deg usually
results in fewer than three visible satellites. However,
as observed in Ref. 1, a user can still obtain a position
fix with fewer than four satellites if he is willing to wait
for a significant change in satellite geometry.

These results are averages over a 24-hour period;
thus, there may be times and locations where four satellites
are visible with narrower beam (e.g., less than 120 deg)
directional antennas. However, since these regions and
times are isolated, they are difficult to rely on when
considering a continuous, 24-hour navigation capability.

9

Thus, these average results provide a realistic picture of satellite visibility with directional antennas.

2.1.2 Visibility With Off-Vertical Boresight Antennas

The visibility results of the preceding section can be extended to an off-vertical boresight directional antenna by referencing its beamwidth and elevation angle to a suitably located vertical boresight directional antenna. This enables the evaluation of any potential advantages of off-vertical antenna orientations using the results of Section 2.1.1. The relationship between vertical boresight (reference) and off-vertical boresight (user) directional antennas with the same satellite visibility or satellite orbit coverage is illustrated in Fig. 2.1-2. This figure shows that

R-16010
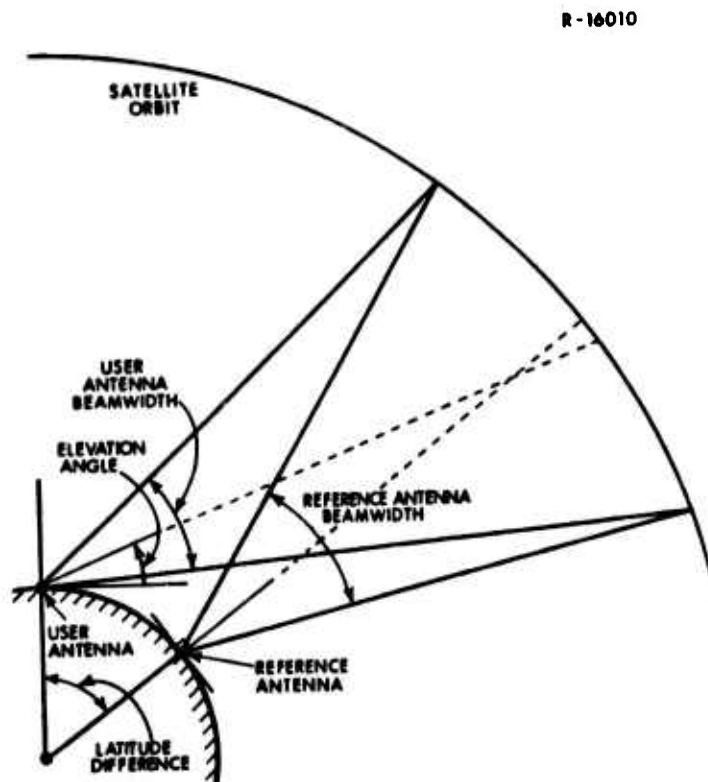
Figure 2.1-2   Antenna Beamwidth Comparisons

10

the "sky coverage" of an off-vertical (user) antenna can be adjusted so that it is the same as that of a vertical (reference) antenna of different beamwidth located directly under the "sky coverage" area.

As the user antenna elevation angle decreases, the latitude difference between the user and reference antennas increases and the user antenna beamwidth decreases slightly in order to maintain the same satellite visibility or "sky coverage" as the reference antenna. The relation between the user and reference antenna beamwidths is shown in Fig. 2.1-3. This figure indicates that the user antenna beamwidth does not change appreciably as the latitude difference increases. For a given reference antenna beamwidth, a point
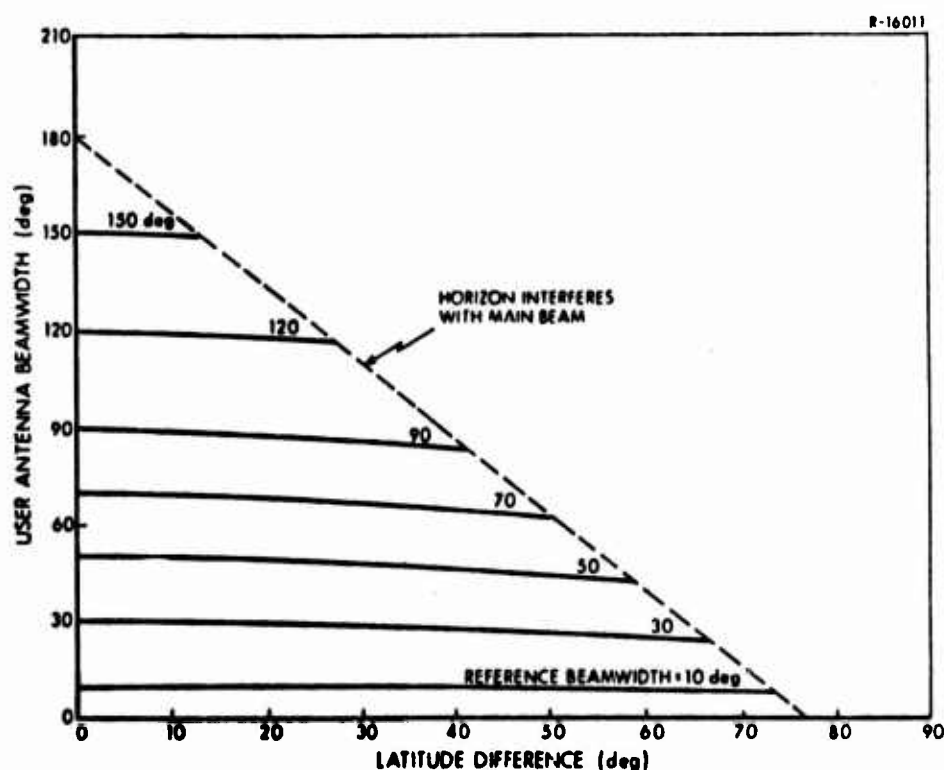
Figure 2.1-3   Vertical and Off-Vertical Boresight
Directional Antenna Relationship

11

will be reached where the horizon interferes with the user antenna main lobe or beam as the latitude difference increases; this point is indicated by the dashed line in Fig. 2.1-3.

Because the equivalent beamwidth of an off-vertical boresight (user) directional antenna does not change appreciably (within the applicable elevation angles) from that of a vertical reference directional antenna, the satellites visible to an off-vertical boresight antenna are approximately the same as those visible to a suitably-located vertical boresight antenna of the same beamwidth. Thus, any advantage gained by using off-vertical antennas would be derived by pointing to an advantageous sector of the sky. However, Fig. 2.1-1 indicates only a small advantage in pointing the user antenna to more advantageous "sky latitudes" (i.e., the curves are relatively flat). It thus appears that little is gained by the deployment of off-vertical boresight directional antennas for the simultaneous reception of four GPS navigation signals.

2.2 USER PERFORMANCE WITH DIRECTIONAL ANTENNAS

As illustrated in the preceeding section, the GPS users' satellite visibility is restricted with directional antennas. Depending upon the beamwidth of these antennas, the users' visibility may be restricted to four satellites that provide a relatively large GDOP (Geometric Dilution of Precision, Ref. 1) or to fewer than four satellites. Since the satellite-user geometry (as reflected in the GDOP) directly affects the accuracy with which a user may determine his position, a large GDOP may result in poor estimates of user position. If fewer than four satellites are visible with a particular directional antenna (e.g., with a very narrow beamwidth),

12

the user may have to wait for a significant change in the position of the satellites to obtain a navigation fix (Ref. 1) or, alternatively, point the antenna separately to four satellites.

This section considers the navigation performance of a user employing directional antennas. Two directional antennas are considered, one which restricts visibility to four satellites and one which restricts visibility to a single satellite. The scenario and models used in this study are discussed in Section 2.2-1. The satellite-user geometry effects or GDOP for this scenario are discussed in Section 2.2.2 along with the satellite visibility data. User performance projections are then presented in Section 2.2.3 for three user antenna beamwidths. These performance projections (as well as those of Chapter 4) were obtained using the DSIM computer program (Ref. 2) and the GPS tracking system performance data summarized in Appendix B. DSIM consists of a "real world" simulator as well as a simulation of the user navigation filter. The "real world" simulator generates actual satellite ephemerides, synthesizes noise-corrupted pseudo-range (and pseudo-range-rate, if required) measurements and generates the user trajectory, thus making possible an assessment of the performance of the user navigation filter implementation by providing time histories of estimated navigation states (e.g., position and velocity) for comparison with the true values. The real world models used in the DSIM program are discussed in Ref. 2, except for the satellite clock model, which is outlined in Appendix B, and the user clock model, which is discussed in Section 2.2-1.

13

2.2.1 User Scenario and Models

Scenario — The scenario assumed for this investigation consists of a stationary manpack user with one of three antennas: conventional (baseline), wide beam directional and narrow beam directional. The conventional antenna is a fixed hemispherical antenna with 170 deg beamwidth (5 deg masking angle) directed vertical. The wide beam directional antenna has a beamwidth of 120 deg directed vertically (main beam). With these two antennas, measurements are made sequentially to the four satellites (nos. 1, 2, 3, 5, which provide the best GDOP) at a 10 sec/satellite rate. The narrow beam directional antenna is assumed to provide visibility to only one satellite, and is slewed sequentially by the user to selected satellites. This antenna dwells on each satellite for 50 seconds during which time measurements are made at a rate of 10 sec/measurement. The direction in which this narrow beam antenna is to be pointed (which depends upon the selected satellite) is determined by the users' GPS computer. The user for the simulation runs presented here is assumed to be located at 50 deg north, 100 deg west.

Receiver — For purposes of this study, a manpack receiver was modeled as a sequential set utilizing pseudo-range measurements (no pseudo range rate). These measurements are corrupted by several error sources including receiver mechanization errors, signal propagation path delays and user clock errors, in addition to the satellite ephemeris and clock errors. The receiver mechanization errors modeled in this study include thermal noise and signal quantization. Thermal noise errors are modeled as a normally distributed, zero-mean, random sequence while the signal quantization errors are uniformly distributed. The parameter values associated with the receiver mechanization error sources, summarized in Table 2.2-1,

14

TABLE 2.2-1

GPS RECEIVER MECHANIZATION ERRORS

ERROR SOURCE	STANDARD DEVIATION OR RANGE
Pseudo-Range Thermal Noise (Normally Distributed)	1.4 m
Pseudo-Range Quantization (Uniformly Distributed)	±0.3 m

are based on previous studies (Ref. 2 and 31), concurrent studies (Ref. 32) and Air Force Specification (Ref. 24).

The propagation effects modeled in this study include residual ionospheric and tropospheric delays. The residual ionospheric delay errors are those remaining after two-frequency ionospheric compensation (Ref. 2). Residual tropospheric delay errors are those remaining after analytical compensation. The residual tropospheric delay errors are most significant near the horizon and thus are a function of the user-to-satellite elevation angle. The numerical values used in this study for the propagation path errors have been obtained from previous studies (Ref. 2 and 31) and are summarized in Table 2.2-2.

TABLE 2.2-2

PROPAGATION PATH DELAY ERRORS

ERROR SOURCE	STANDARD DEVIATION	CORRELATION TIME
Residual Ionospheric Delay	0.76 m	7200 sec
Residual Tropospheric Delay*	0.076 m	∞

*This value is multiplied by the cosecant of the user-to-satellite elevation angle.

User Clock — This clock is a quartz crystal oscillator with the intrinsic stability model developed in Appendix C. The fractional frequency stability plot for this clock model is shown in Fig. 2.2-1. This clock error model as depicted in Fig. 2.2-2, can be written in state variable form (Ref. 5) as

$$\underline{\dot{x}}_c(t) = F_c \, \underline{x}_c(t) + \underline{w}_c(t) \qquad (2.2-1)$$

where

$\underline{x}_c(t) = [\delta\phi, \delta f, \delta\dot{f}, x_{1f}, x_{2f}]^T$ is the 5x1 vector of error states defined in Table 2.2-3.

F_c is the clock error model dynamics matrix

$\underline{w}_c(t) = [w_1 \;\; 0 \;\; 0 \;\; w_2 \;\; w_3]^T$ is the 5x1 vector of white noise such that $E[\underline{w}_c(t)] = 0$, $\text{Cov}[\underline{w}_c(t)] = E[\underline{w}_c(t)\,\underline{w}_c^T(\tau)] = Q_c(t)\,\delta(t-\tau)$ and $\delta(t)$ is the Dirac delta function.
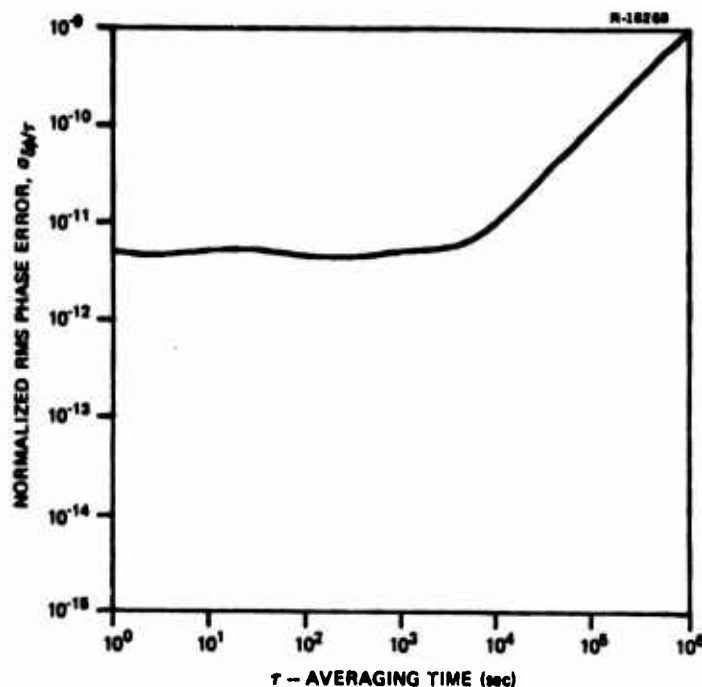
Figure 2.2-1   Fractional Frequency Stability Characteristic for Quartz Crystal Clock Model

16
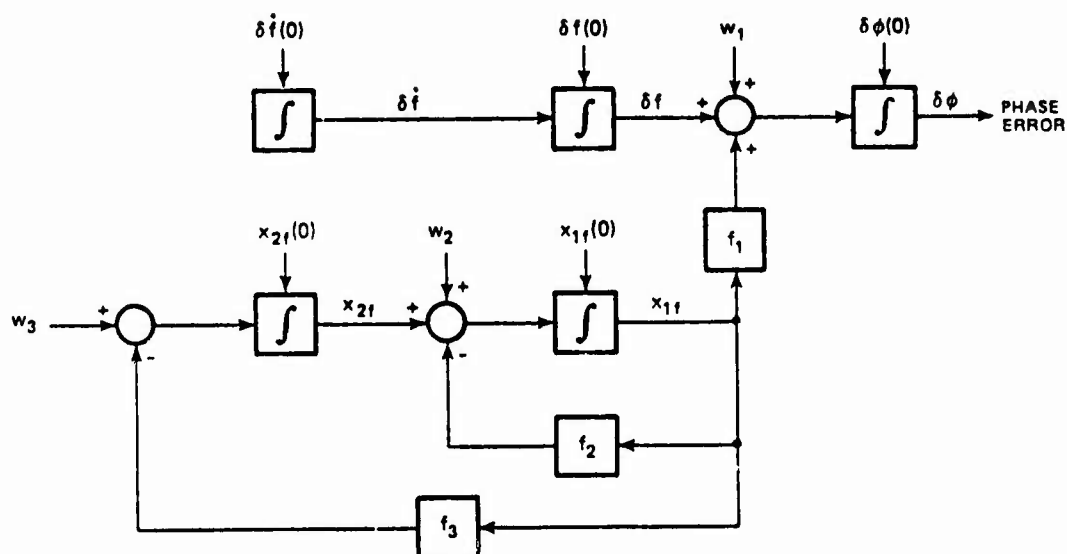
Figure 2.2-2   User Clock Model

TABLE 2.2-3

USER CLOCK ERROR STATE DEFINITIONS

SYMBOL	ERROR SOURCE DEFINITION	UNITS
$\delta\phi$	Phase Error	m
δf	Frequency Error	mps
$\delta\dot{f}$	Aging Error	m/sec^2
x_{1f}	Flicker Noise State 1	mps
x_{2f}	Flicker Noise State 2	m/sec^2

17

The clock error model dynamics matrix, F_c, is given by

$$F_c = \begin{bmatrix} 0 & 1 & 0 & f_1 & 0 \\ 0 & 0 & 1 & 0 & 0 \\ 0 & 0 & 0 & 0 & 0 \\ 0 & 0 & 0 & f_2 & 1 \\ 0 & 0 & 0 & f_3 & 0 \end{bmatrix} \qquad (2.2\text{-}2)$$

where f_1, f_2 and f_3 are defined in Eq. (C.3-7). The clock error model process noise matrix, Q_c, is given by

$$Q_c = \begin{bmatrix} 1.026 \times 10^{-6} & 0 & 0 & 9.324 \times 10^{-5} & 1.016 \times 10^{-6} \\ 0 & 0 & 0 & 0 & 0 \\ 0 & 0 & 0 & 0 & 0 \\ 9.324 \times 10^{-5} & 0 & 0 & 8.478 \times 10^{-3} & 9.234 \times 10^{-5} \\ 1.016 \times 10^{-6} & 0 & 0 & 9.234 \times 10^{-5} & 1.005 \times 10^{-6} \end{bmatrix}$$

$$(2.2\text{-}3)$$

Units of the Q_c-matrix elements are consistent with those given in Table 2.2-3 for the corresponding state variables.

Dashed line User Filter — The user navigation filter is a Kalmann mechanization (Ref. 5) which assumes the user is stationary. The user filter error model in state variable form can be written as

$$\underline{x}(t) = F \underline{x}(t) + \underline{w}(t) \qquad (2.2\text{-}4)$$

where

$\underline{x}(t) = [\delta R_u^T, \underline{x}_c^T]^T$ is the 8x1 column vector of user error states

F is the user error dynamics 8x8 matrix

18

$$\underline{w}(t) = \left[0,0,0, \underline{w}_c^T \right]^T \text{ is the 8x1 column}$$

vector of white process noise
such that $E\left[\underline{w}(t)\right] = 0$,
$\text{Cov}\left[\underline{w}(t)\right] = E\left[\underline{w}(t) \underline{w}^T(\tau)\right] =$
$Q(t) \delta(t-\tau)$

The user position error states are given by

$$\delta \underline{R}_u = \left[\delta R_n, \ \delta R_e, \ \delta h \right]^T \tag{2.2-5}$$

where δR_n, δR_e and δh are the north, east and altitude components. The user error dynamics matrix, F, is given by

$$F = \begin{bmatrix} 0_{3x3} & \vdots & 0_{3x5} \\ - - - - & -\vdots- & - - - \\ 0_{5x3} & \vdots & F_c \end{bmatrix} \tag{2.2-6}$$

where F_c is given by Eq. (2.2-2). The user process noise matrix, Q, is given by

$$Q = \begin{bmatrix} 0_{3x3} & \vdots & 0_{3x5} \\ - - - - & -\vdots- & - - - \\ 0_{5x3} & \vdots & Q_c \end{bmatrix} \tag{2.2-7}$$

where Q_c is given by Eq. (2.2-3).

The inputs to the filter are the pseudo-range measurements from the receiver. These measurements were assumed, by the filter, to contain 1.6 m white measurement error. This value is assumed to account for propagation delays, receiver errors, and satellite clock and ephemeris errors. The filter uses these measurements along with the initial values summarized in Table 2.2-4 to estimate the user's position (both horizontal and altitude) and the five states of the clock model.

During the course of this study, it was noted that the originally developed manpack navigation filter summarized

19

TABLE 2.2-4

MANPACK USER APRIORI STATE ERRORS AND FILTER STATISTICS

SYMBOL	STATE DEFINITION	INITIAL ESTIMATION ERROR		INITIAL FILTER STANDARD DEVIATION		CORRELATION TIME	PROCESS NOISE SPECTRAL DENSITY	
		VALUE	UNITS	VALUE	UNITS	VALUE	VALUE	UNITS
δR_n	North Position Error	-1000	m	2000	m	∞	0^*	m^2/sec
δR_e	East Position Error	1200	m	2000	m	∞	0^*	m^2/sec
δh	Altitude Error	150	m	2000	m	∞	0^*	m^2/sec
$\delta\phi$	Clock Phase Error	1800	m	2000	m	—	See Eq. (2.2-1)	
δf	Clock Frequency Error	0.3	mps	0.3	mps	∞		
$\delta\dot{f}$	Clock Aging Error	5×10^{-7}	m/sec^2	5.84×10^{-7}	m/sec^2	∞		
x_{1f}	Flicker Noise State 1	-0.2	mps	0.237	mps	9.9 sec		
x_{2f}	Flicker Noise State 2	5×10^{-3}	m/sec^2	7.13×10^{-3}	m/sec^2	—		
p_1	Pseudo-State No. 1	-8	m	10	m	∞	0	m^2/sec
p_2	Pseudo-State No. 2	+5	m	10	m	∞	0	m^2/sec
p_3	Pseudo-State No. 3	+2	m	10	m	∞	0	m^2/sec
p_4	Pseudo-State No. 4	-15	m	10	m	∞	0	m^2/sec

*This value is 1 m^2/sec for the process noise method of filter augmentation.

in the preceding paragraphs, <u>could produce significant errors</u> <u>due to the unmodeled errors in the satellite ephemeris and</u> <u>clock data</u>. Two methods of augmenting user filters to account for unmodeled errors were investigated during this study. One method uses process noise on the position states, while the other involved the addition of "pseudo-states" to the user filter. The <u>process noise method</u> of filter augmentation effectively accounts for the satellite ephemeris and clock errors as uncertainty in user position. This method changes the user filter process noise matrix, Eq. (2.2-7), as follows:

$$
Q_{pn} = \begin{bmatrix} q & 0 & 0 & \vdots & \\ 0 & q & 0 & \vdots & 0_{3 \times 5} \\ 0 & 0 & q & \vdots & \\ - & - & - & - & - \\ & 0_{5 \times 3} & & \vdots & Q_c \end{bmatrix} \tag{2.2-8}
$$

where q is the spectral density of the user position uncertainty. The value of q is best determined by simulation experiments.

The <u>pseudo-state method</u> of filter augmentation adds to the user filter model a pseudo-state for each satellite to effectively represents the combined ephemeris and clock errors for that satellite. The user position error states, $\delta \underline{R}_u$, are augmented with pseudo-states, $\underline{p}$, as follows (assuming m satellites are used for measurements):

$$
\delta \underline{R}_u' = \begin{bmatrix} \delta \underline{R}_u \\ \\ \underline{p} \end{bmatrix} \tag{2.2-9}
$$

21

where

$\delta \underline{R}_u$ is the 3x1 column vector of user position error states

$\underline{p} = [p_1, p_2, \ldots, p_m]^T$ is the mx1 column vector of pseudo-states

These pseudo-states are modeled as biases in the user filter and are dynamically uncoupled from the other filter states. The user filter error dynamics matrix, Eq. (2.2-6), is thus modified as follows,

$$F = \begin{bmatrix} 0_{(3+m) \ x \ (3+m)} & \vdots & 0_{(3+m) \ x \ 5} \\ - - - - - - - - - & \vdots & - - - - - - - \\ 0_{5 \ x \ (3+m)} & \vdots & F_c \end{bmatrix} \qquad (2.2-10)$$

The user filter process noise matrix, Eq. (2.2-6), is modified as follows,

$$Q = \begin{bmatrix} 0_{(3+m) \ x \ (3+m)} & \vdots & 0_{(3+m) \ x \ 5} \\ - - - - - - - - - & \vdots & - - - - - - \\ 0_{5 \ x \ (3+m)} & \vdots & Q_c \end{bmatrix} \qquad (2.2-11)$$

Since the pseudo-states are used to represent the combined satellite ephemeris and clock errors which occur in the pseudo-range measurements, they are used during the filter updates with these measurements; that is, if the true pseudo-range, δz_i, to the ith satellite is given by (Ref. 1)

$$\delta z_i = \underline{1}^T_{\rho_u^i} \ \delta \underline{R}_u + \delta \phi + n_i \qquad (2.2-12)$$

where

$\underline{1}^T_{\rho_u^i}$ is the unit vector between user and i^{th} satellite

n_i is the pseudo-range measurement error, including the ith satellite ephemeris and clock errors

22

then, the estimated pseudo-range measurement error, $\delta\hat{z}_i$, for this measurement is given by

$$\delta\hat{z}_i = \underline{1}^T_{\rho_u}{}_i \quad \delta\hat{\underline{R}}_u + \delta\hat{\phi} + \hat{p}_i \tag{2.2-13}$$

The difference between these two quantities (i.e., $\delta z_i - \delta\hat{z}_i$) is used to update the filter measurements. Note that the pseudo-states in Eq. (2.2-13) are basically accounting for the satellite ephemeris and clock errors in the measurement error of Eq. (2.2-12) (assumed to be included in the measurement error, n_i). Thus, this is a better method of accounting for the unmodeled satellite ephemeris and clock errors than to assume uncertainty in user position through use of process noise. However, this method increases the filter complexity and computational load. Also, whenever the satellite ephemeris and clock data is uploaded by the ground tracking system, there is an abrupt change in the resulting errors in the ephemeris and clock data in the measurements δz_i. This uploading could be modeled in the user filter by resetting the pseudo-states to zero and the pseudo-state variances and covariances to their initial (a priori) values after the upload. However, this might unacceptably complicate the software implementation, although this aspect of the pseudo-state argumentation technique has not been investigated.

The pseudo-states were initialized with the values summarized in Table 2.2-4. These values were chosen on the basis of the magnitudes of the ephemeris and clock errors illustrated in Appendix B. Comparison of user performance projections using the two methods of filter augmentation discussed above are presented in Section 2.2.3.

2.2.2 GDOP and Satellite Visibility

Geometric dilution of precision (GDOP) is a figure of merit common to radio navigation system performance eval-

23

uation. GDOP depends upon the satellite-user geometry and
thus changes as the satellites and user move relative to one
another. The lower the GDOP, the lower and sensitivity of
the pseudo-range measurements to measurement noise. Refer-
ence 1 contains a discussion of GDOP as used in this study.

The CEP* GDOP reflects the horizontal position fix
sensitivity to the pseudo-range measurement errors. This is
illustrated in Fig. 2.2-3 for a user located at 50 deg N,
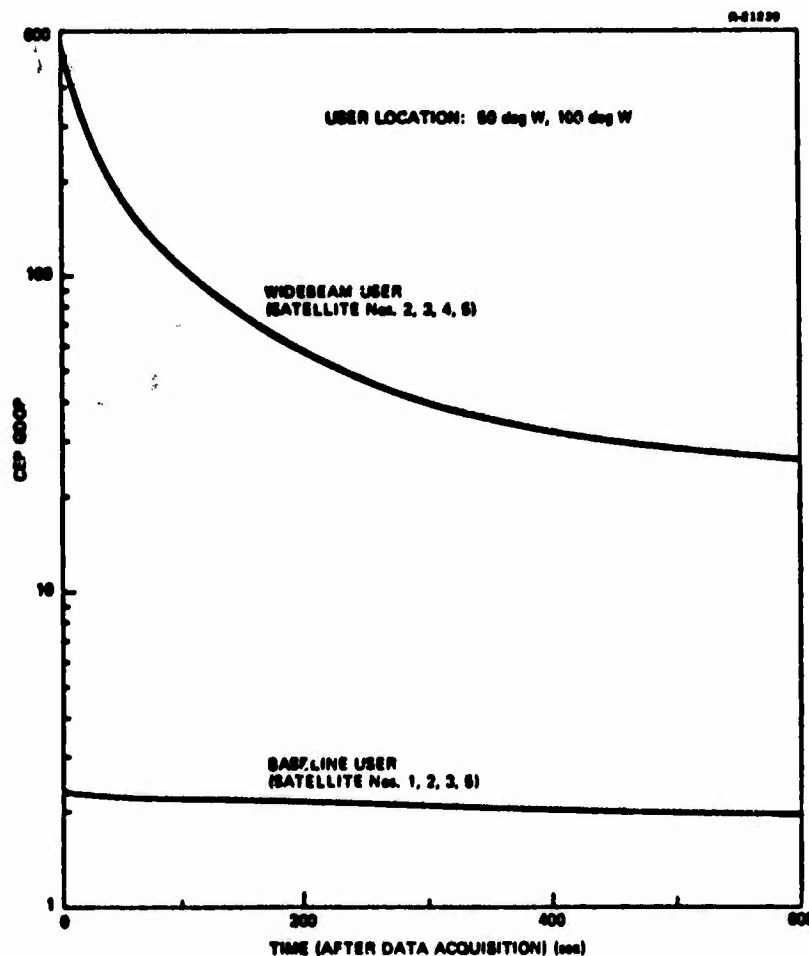
Figure 2.2-3   User GDOP and Satellite Visibility

*Circular Error Probable (CEP) resulting from uncorrelated
 unity-variance pseudo-range measurement errors from each
 satellite (using all visible satellites).

24

100 deg W using the five satellite subset of the 24-satellite Phase III configuration visible to the user, as discussed in Appendix B. Both the conventional and wide beam directional antenna cases are shown. Note that GDOP (as used in this study) is only defined when four or more satellites are visible.

A user with the conventional antenna (170 deg) can "see" all five satellites, so that he can select four which give the best GDOP as illustrated (Satellite Nos. 1, 2, 3 and 5). However, the wide beam directional antenna (120 deg) user only "sees" four satellites which, in this instance, provide relatively poor GDOP. However, as illustrated in the next section, <u>a user employing a Kalman filter may not be seriously penalized by this poor GDOP, depending on the time available for obtaining the GPS position fix.</u>

2.2.3 Performance Projections

Typical navigation performance projections of a GPS manpack user with a directional antenna are summarized in this section. These results are presented in the form of time histories of the <u>navigation filter estimation error</u> as well as the <u>navigation filter standard deviation boundary</u> for an error state. The standard deviation boundaries are computed by taking the square root of the diagonal element of the user navigation filter covariance matrix corresponding to the particular error of interest and plotting its plus and minus values. According to estimation theory (Ref. 5), if the real world physical processes are modeled properly in the filter, the estimation errors should not go outside the standard deviation boundaries more than 31.7% of the time. If this condition is not satisfied, then the filter

does not properly model the physcial process, and a filter redesign is in order.

The time required to acquire the satellite signals and to obtain the satellite ephemerides and other data from these signals has not been accounted for in these results. It is assumed that the signals have been acquired and data removed before the navigation filter solution is initiated at t = 0. Acquisition performance was analyzed previously (Ref. 1).

This discussion of user performance is initiated with a comparison of the two methods of filter augmentation described in Section 2.2.1. User performance projections for the scenario and models of Section 2.2.1 are presented next for three types of antennas: conventional (the baseline), wide beam directional and narrow beam directional.

Filter Augmentation — To investigate the two methods of augmenting the navigation filter to account for satellite ephemeris and clock errors as discussed in Section 2.2.1, the conventional antenna stationary user (baseline) scenario was used. A comparison of the root sum squared (rss) horizontal position error for these two methods is shown in Fig. 2.2-4. In order to clearly show the steady-state behavior of the filter, the large initial transient error which occurs before four measurements have been taken is not shown.

The addition of process noise in the filter gain computation causes the sawtooth pattern of the standard deviation boundary (illustrated in the top graph) and unrealistically limits the reduction of the uncertainty of the position estimates as additional measurements are taken.

26
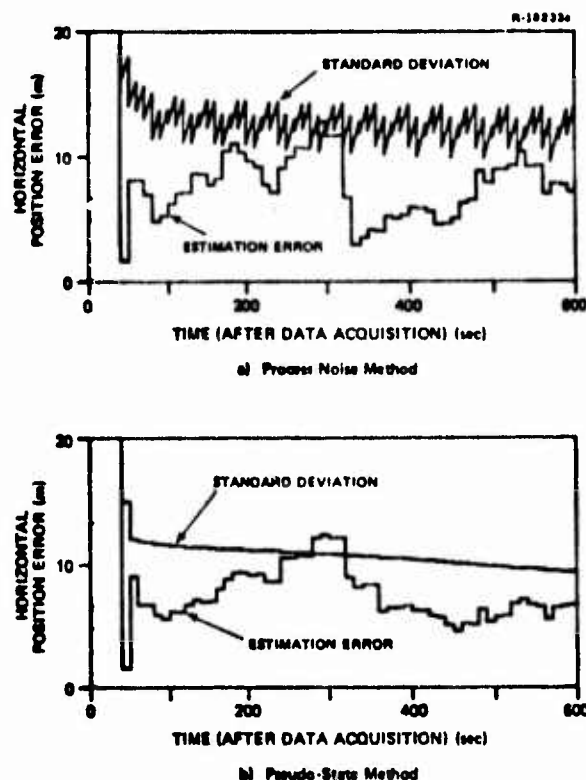
Figure 2.2-4   Filter Augmentation Comparison

The performance of the pseudo-state augmented filter
(bottom graph) is more realistic for the stationary user, since
the uncertainty in the estimates decreases with additional
measurements. These results indicate that the pseudo-state
augmentation is the better method of accounting for satellite
ephemeris and clock data error, although the relatively small
improvement shown in Fig. 2.2-4 may not justify the additional
filter complexity. Nonetheless, subsequent studies included
in this section incorporate pseudo-states.

Baseline — In order to provide a standard with which
to compare performance of users with directional antennas,
performance projections for a stationary user with a conven-
tional (hemispherical) antenna was generated, using the scen-
ario and models (e.g., receiver, clock, filter) given in Sec-
tion 2.2.1. Measurements were made sequentially to Satellite

27

Nos. 1, 2, 3 and 5, at a 10 sec/satellite rate. As illustra-
ted in Fig. 2.2-3, the CEP GDOP for this user varies between
1 and 3.

Performance for this baseline case is illustrated in
Fig. 2.2-5. Again, the initial transient errors are not shown
in order to clarify the steady-state performance of the filter.
Further design of the filter and, in particular, the selection
of the initial pseudo-state uncertainty, may improve this base-
line performance. However, detailed filter design was not the
objective of this study.

Wide Beam User — The directional antenna for this
user has a beamwidth of 120 deg and is pointed vertically.
Four satellites are visible to this user throughout the 10-
minute time duration of this case. However, this user experi-
ences poor GDOP, as shown in Fig. 2.2-3, with a corresponding
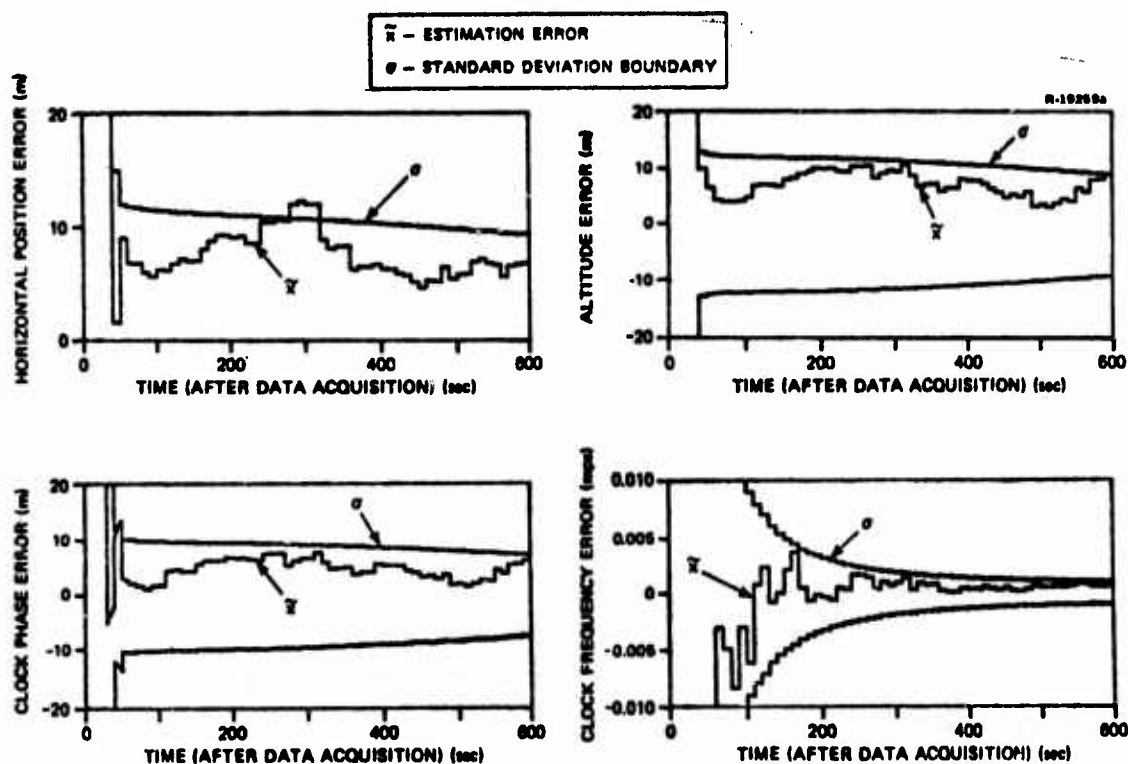
Figure 2.2-5   Baseline Performance

28

degradation in user performance as illustrated in Fig. 2.2-6.
The uncertainty in the estimates, as indicated by the standard
deviation boundary, is strongly dependent upon GDOP. This is
particularly evident in the horizontal position error results.
The horizontal position error standard deviation after four
sequential measurements and at the end of the simulation are
summarized in Table 2.2-5. After four measurements, this
standard deviation for the wide beam user is a factor of 8.7
larger than that of the baseline user, because of the poor
GDOP. However, as additional measurements are taken this
error standard deviation is reduced to a value comparable to
that for the baseline user.
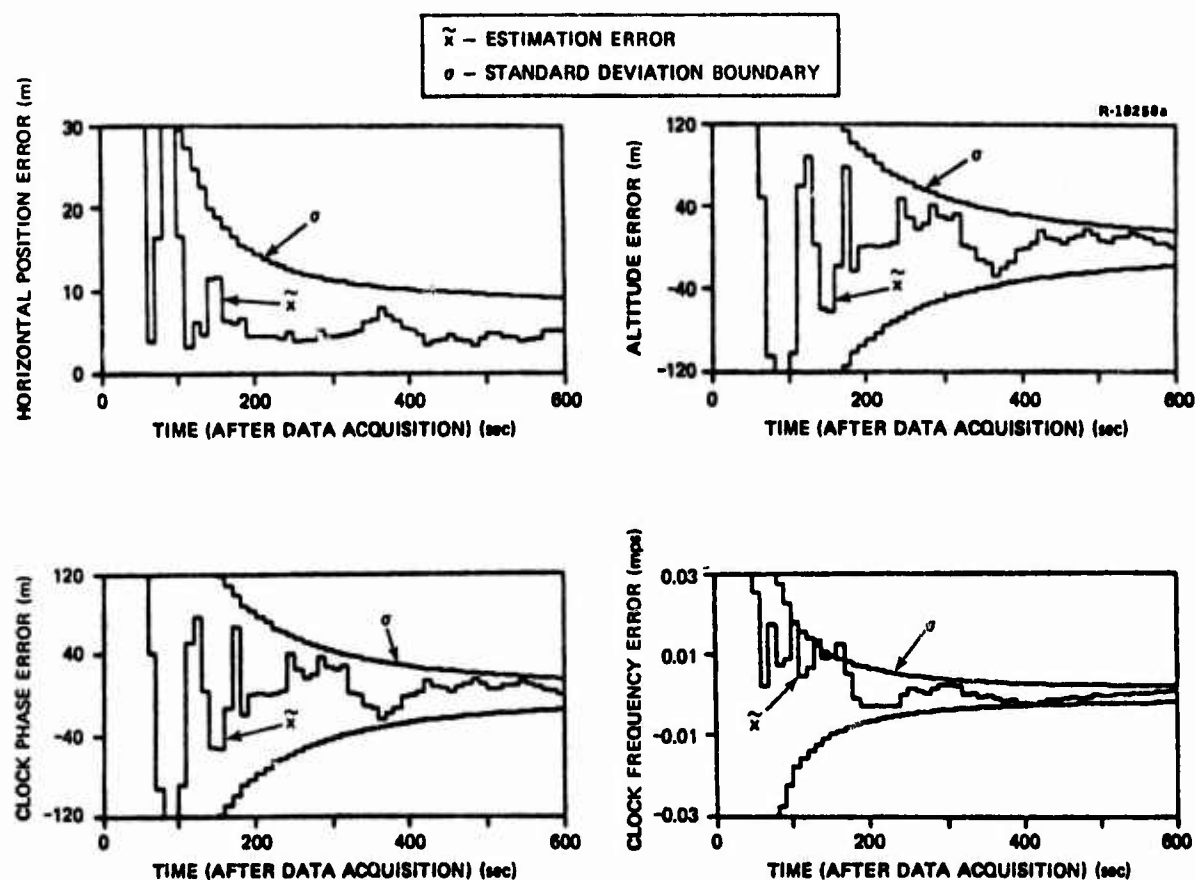
Figure 2.2-6   Wide Beam User Performance

TABLE 2.2-5

PERFORMANCE SUMMARY

USER	HORIZONTAL POSITION ERROR STANDARD DEVIATION	
	40 sec	600 sec
Baseline	15 m	9.4 m
Wide Beam	131 m	9.4 m

Narrow Beam User — An Army manpack GPS user may
be subject to an environment in which foliage attenuates
the GPS navigation signal and/or interference from elec-
tronic jamming is present, preventing acquisition and use
of the GPS navigation signals. One method of overcoming
these problems is through the use of a narrow beam direc-
tional antenna which can be physically pointed by the user
in the direction of a GPS satellite. The navigation signal
strength would be enhanced by the gain of the antenna, while
reducing the effects of interference and jamming by virtue
of the spatial properties of the antenna.

In order to obtain a navigation solution, pseudo-
range measurements to at least four satellites are required
(assuming no a priori knowledge of position or time). Thus,
the antenna must be separately pointed physically to at
least four satellites in sequence. The user computer would
indicate approximately where to point the antenna, and the
receiver could indicate when the desired signal has been
acquired.

In this study of a user with a narrow beam directional
antenna, the pointing of the antenna to each satellite is simu-
lated by taking five measurements (at a 10 sec rate) to one

satellite and switching to the next satellite for five measurements, and so forth. The satellite selection sequence was 1, 2, 3, 4, and 5. Holding on individual satellites for five measurements is reasonable in view of the fact that the antenna must be reoriented by the user to acquire a new satellite. With this technique, all satellites above the horizon are available to the user. Time required to reposition the antenna to a new antenna has not been taken into account in this simulation. During this repositioning period, the filter could be in a "hold" condition in which no measurements or processing is performed. In addition, the time required to acquire the satellite signal and data has not been included. The time required to perform both antenna repositioning and satellite signal and data acquisition would simply add to the time required to obtain a navigation fix as illustrated in the results presented below.

Typical performance for this user is illustrated in Fig. 2.2-7. The horizontal position error has been plotted with a vertical logarithm scale in order to illustrate the wide variation in dynamic range of this error as the measurements are processed. This curve indicates that measurements to the fourth satellite reduce the horizontal position error to less than 10 m. After the measurements to the fourth satellite the horizontal position error falls outside the standard deviation boundary. This is indicative of a minor filter design problem which was not pursued in this study. The other user errors (altitude, clock phase and clock frequency) shown in Fig. 2.2-7 are also strongly dependent on acquisition of the fourth satellite. Additional measurements to the same set of five satellites does not significantly reduce the error after the initial set of measurements has been processed.

Performance for the narrow beam antenna user compares favorably with that of the baseline user. The time required

31
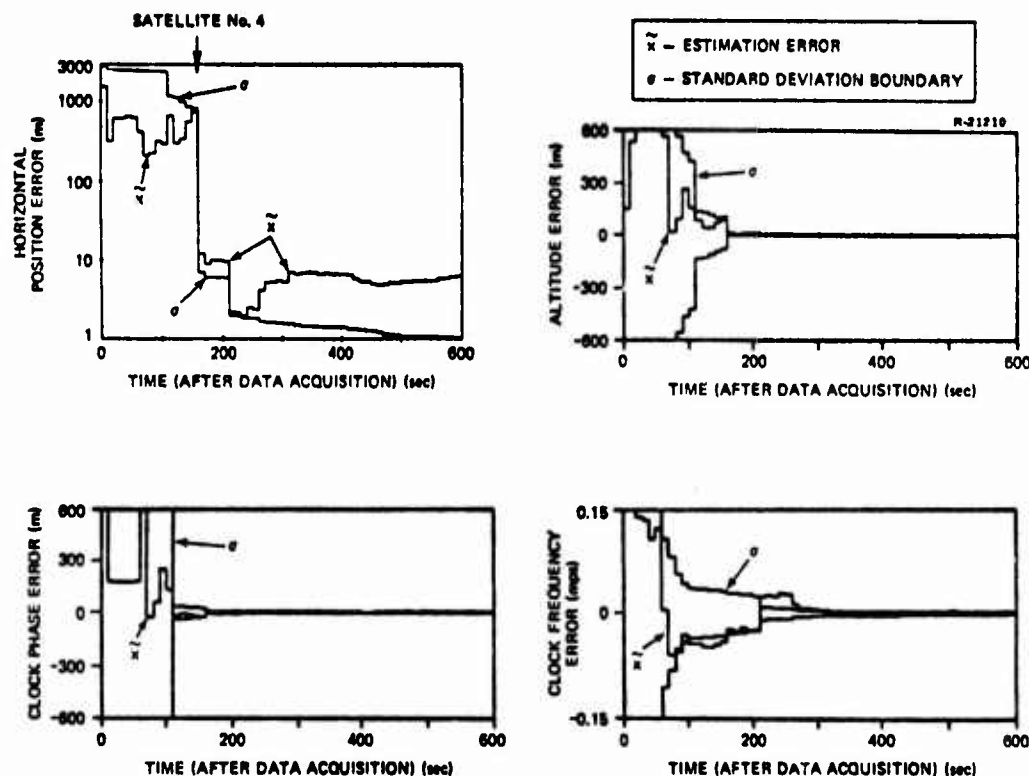
Figure 2.2-7   Narrow Beam User Performance

to obtain a satisfactory navigation solution in this scenario
is about 3 min plus the time required to reposition the antenna
three times and acquire satellite signals and data.

2.2.4 Performance Summary

The performance of a GPS user whose satellite visi-
bility is restricted with a directional antenna is not adversely
affected by this restriction as long as the measurements to a
sufficient number of satellites are processed with a Kalman
navigation filter.   Augmentation of this filter with pseudo-
states may be advantageous for a stationary user.   Large GDOPs
can result in a significant degradation in performance although
movement of the satellites alleviates this problem within 10 min.
The use of a very narrow beamwidth antenna that is physically
pointed to the satellites can provide accurate position esti-
mates, although the time required to obtain these estimates is

also affected by the time required to position the antenna.
In general, position estimation errors of less than 10 m are
possible for users with directional antennas. The accuracy of
the estimates generated here could be improved with further
filter design refinements.

2.3   ANTENNA ARRAY SYSTEMS

Directional antennas can be constructed from an ar-
ray of discrete isotropic antennas or elements. Depending
upon the relative position of the elements with respect to
each other and the signal frequency, the antenna array gain
will be greater in some directions than in others. If the
output signal from each element is delayed with respect to
a reference element by a given amount, the direction of this
maximum array gain can be changed. This results in a direc-
tional antenna with a main beam that can be pointed in any
direction simply by changing the delays. Furthermore, it
is possible to reduce the effects of directional interfer-
ence by placing a null (direction in which the antenna
gain is low) of the antenna beam pattern in the direction of
the interference.

Antenna arrays can provide both spatial and fre-
quency filtering to enhance the desired signal while reduc-
ing undesired directional interference or jamming. This
section presents a discussion of antenna arrays and their
applicability and feasibility for use by a GPS user, par-
ticularly the Army manpack user. A basic discussion of
antenna array processing is presented in Section 2.3.1.
The reduction of directional interference is considered
in Section 2.3.2 with an outline of the optimum array pro-
cessor. Finally, in Section 2.3.3 the application of array
antennas by GPS users is discussed.

33

2.3.1 Antenna Array Processing

Antenna arrays consist of a set of antennas or elements whose outputs are delayed relative to some reference element signal phase such that the signals arriving from a given direction will be in phase after the delaying operation. If these delayed outputs are summed, the signals that are in phase (i.e., those from the given direction) will be enhanced or increased in strength by the number of array elements. Signals arriving from other than the given direction will not be in phase after this delaying operation, and thus will be less enhanced (or degraded), depending upon their phase (i.e., direction). The delays can be changed to "steer" the main beam of the array in any desired direction, thus providing spatial discrimination or filtering.

A simple example will help to illustrate the concept. Consider the linear array with four elements in Fig. 2.3-1. Assume a signal is arriving with a planar wavefront as shown. If the outputs of the elements are delayed by
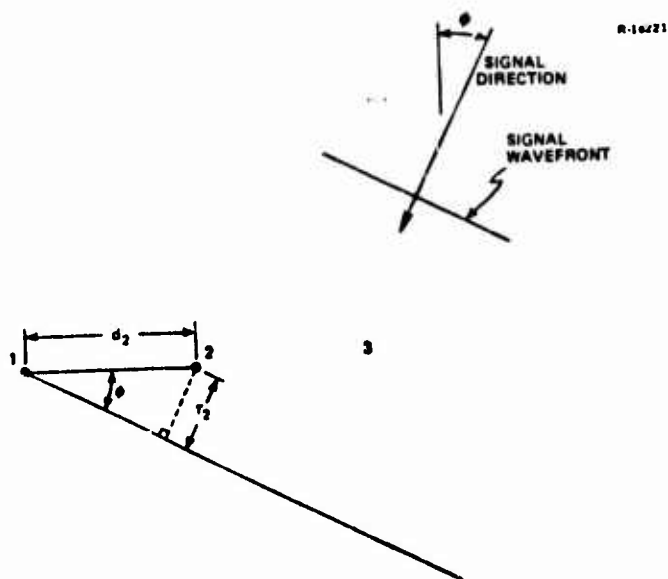
Figure 2.3-1   Four Element Array

$$\tau_i = \frac{d_i}{c} \sin \phi \qquad (2.3-1)$$

where

d_i is the spacing from reference element 1
       to element i

c   is the velocity of propagation

the signal at each delayed output will then be in phase with
the signal at element 1. If these delayed signals are then
summed, the signal strength will be four times as large as
for a single element. Any signal arriving at a direction
other than ϕ will not be in phase at the delayed outputs and
thus will not be enhanced. This array can be steered in any
direction (ϕ) simply by adjusting the delays as given by
Eq. (2.3-1).

The power or beam pattern (Appendix A) for this four
element linear array (assuming each element is an ideal isotro-
pic antenna with element spacing $d = \lambda/2$, where λ = signal wave-
length) is illustrated in Fig. 2.3-2 for a steered direction of
$\phi = 30$ deg. This figure is a polar plot of the array gain as
a function of angle relative to the center of the array in
the plane of the array. The shape of the beam pattern (and
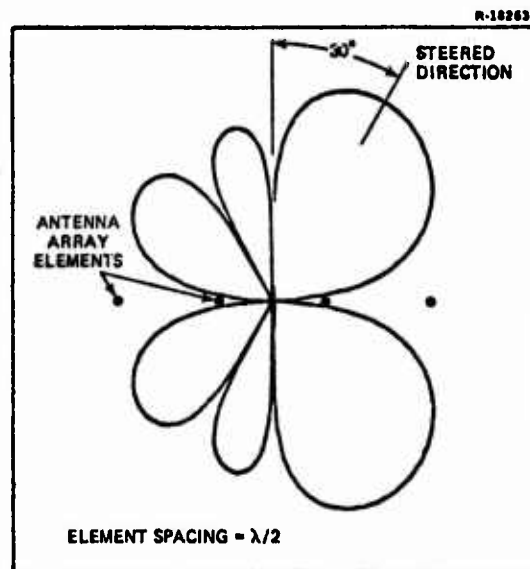
Figure 2.3-2   Typical Beam Pattern of Four
                Element Linear Array

the width of the main beam) will vary with steering direction. Additional elements would reduce the width of the main beam while increasing its gain. Because of array symmetry, the beam pattern revolves around the array axis. Several secondary beams or sidelobes are also evident for this linear array. The relative amplitude of these sidelobes as well as the width of the main beam can be controlled by "shading," that is, by controlling the amplitude of the signal from each element (Ref. 15).

Array antenna beam patterns also exhibit nulls, as evident in Fig. 2.3-2. If an interference signal arrived from the direction of one of these nulls, this interference would be reduced or eliminated at the output of the array. With additional phase shifting and further signal processing, a null can be placed in any desired direction, as discussed in the next section.

2.3.2 Interference Reduction With Arrays

The design of antenna arrays to provide interference reduction or elimination has been investigated by several authors (Refs. 16 to 21). The optimum array/processor configuration for the reduction of a directional interference has been shown to utilize two beams, one steered in the desired signal direction (main beam) and the other steered in the direction of the interference (interference beam) (Refs. 17 and 20). The output of the interference beam is passed through a weighting filter and then subtracted from the signal beam output, as illustrated in Fig. 2.3-3. The beamformers consist of delay elements and frequency filters. The weighting filter modifies the output of the interference beam so that it just equals the contribution of the interference in the

36

R-18223
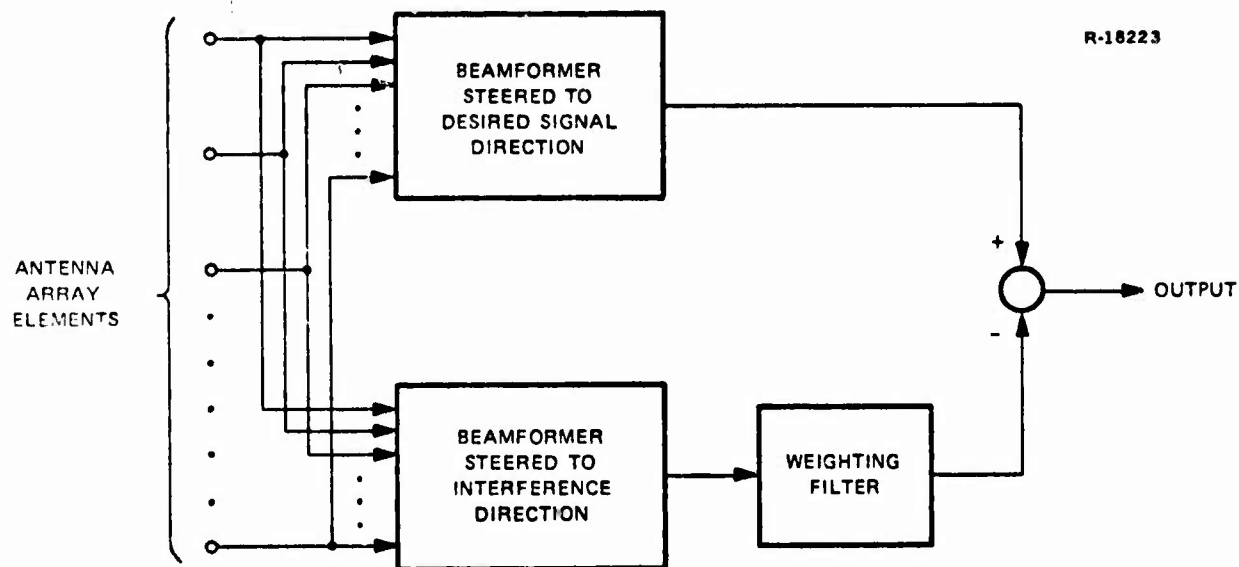
Figure 2.3-3   Interference Reduction Processor

main beam output. Thus the output of the weighting filter
will just cancel the interference signal in the main beam.
This weighting filter is a function of the directior to which the
main and interference beams are steered as well as the inter-
ference power (I)-to-isotropic noise power (N) ratio, (i.e.,
I/N). The isotropic noise power (N) is the power of iso-
tropic noise at each element of the array, assuming the noise
is uncorrelated between elements.

The beam pattern of a four element array with this
interference reduction processor is illustrated in Fig. 2.3-4
for an array steered to a desired signal at 30 deg. and an
interference at 60 deg with I/N = 100 dB. This pattern is
symmetrical about the array axis, as in Fig. 2.3-2; how-
ever, the antenna pattern is significantly different. This
beam pattern indicates that the processor basically steers
a beam pattern null in the direction of the interference, thus
reducing or eliminating its effect from the antenna output.

37
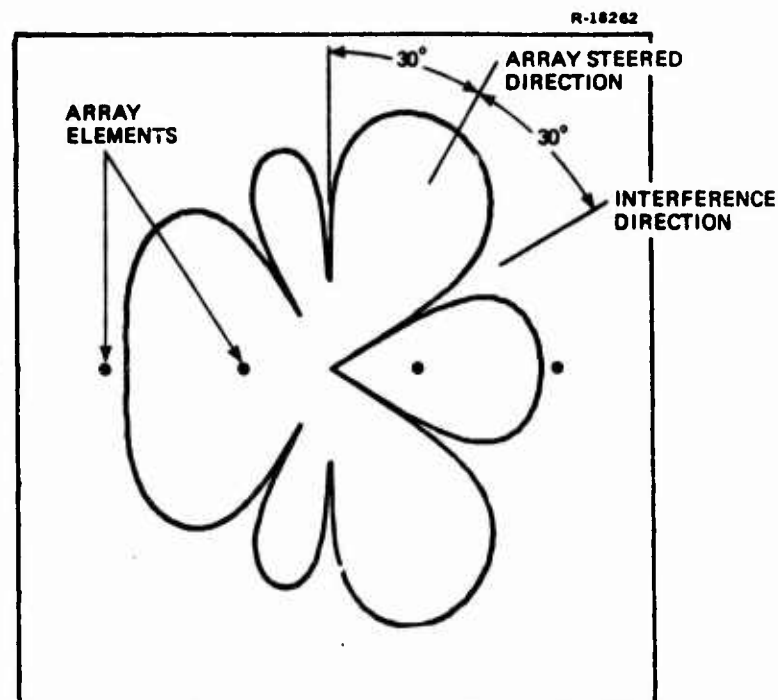
Figure 2.3-4   Beam Pattern With Interference Reduction

        If the interference direction is close to the direc-
tion of the desired signal, the array gain in the desired
signal direction must be compromised. However, if the in-
terference is outside the main beam (that is, at or beyond
the main beam nulls), the antenna array gain or directiv-
ity of the main beam (in the direction of the desired sig-
nal) is not significantly affected (Ref. 20). The influ-
ence of the interference direction on the array gain for a
four element array is illustrated in Fig. 2.3-5. This fig-
ure shows the gain of the array in the direction of the de-
sired signal at 30 deg, as the interference direction is
changed. The array gain is not significantly affected un-
less the interference is within 30 deg of the desired sig-
nal direction. The shape of this gain function is dependent
upon the desired signal direction, I/N ratio, and the num-
ber and spacing of array elements. The interference direction

38
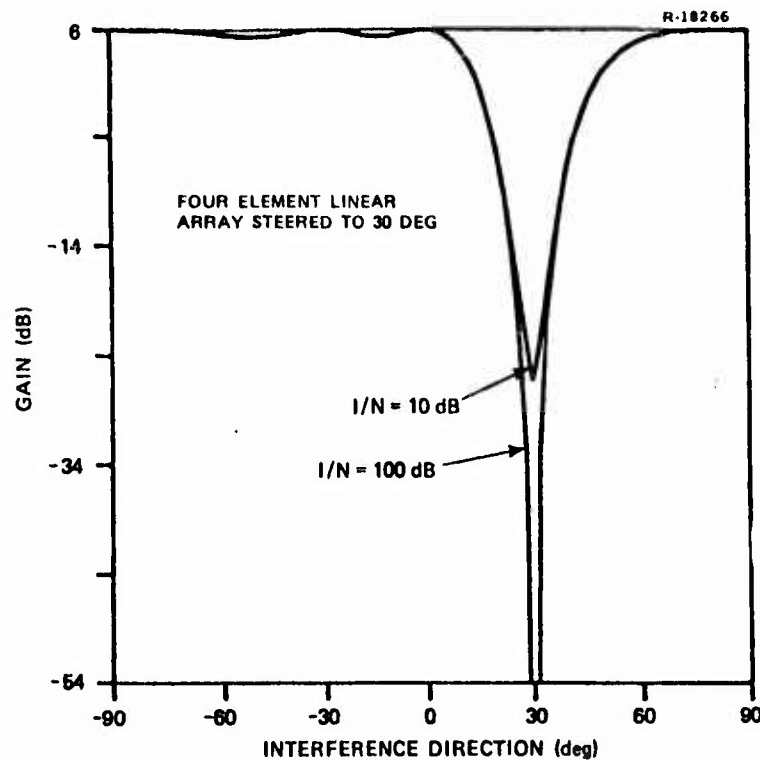
Figure 2.3-5   Array Gain With Interference Reduction

could be closer to the desired signal direction without af-
fecting array gain if the array contained more elements or
the array was steered closer to broadside (ϕ = 0 deg.).

The primary interest in employing interference
reduction with antenna arrays is to improve the tolerance
of the receiving system to directional interference or jam-
ming.   The theoretical reduction in interference provided by
the optimum interference reduction processor is illustrated
in Fig. 2.3-6.   This shows the reduction in the strength
of the interference at the antenna array processor output
as a function of the interference direction with the array
steered to 30 deg for several values of interference-to-
noise (I/N) ratio.   This interference reduction is the
ratio of the gain of the array (with the processor) in the
direction of interference to the gain in the steered

39
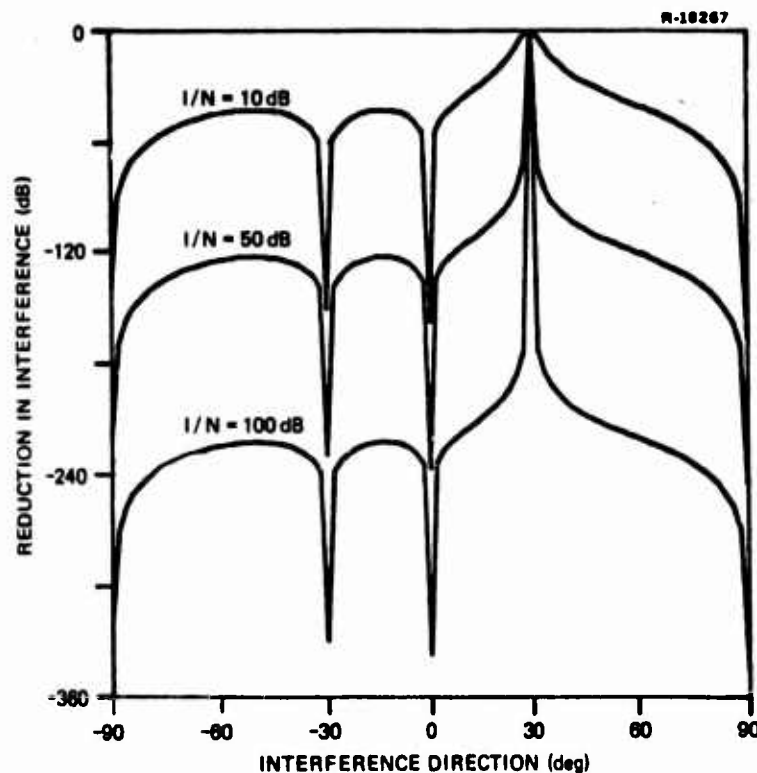
Figure 2.3-6   Theoretical Interference Reduction

direction. The reduction in interference is dependent upon
the strength (power) of the interference; that is, the
stronger the interference, the greater the reduction. How-
ever, if the interference is close to the direction of the
desired signal, then, as shown in Fig. 2.3-5, the array
gain is decreased and the interference reduction technique
becomes ineffective, as indicated in Fig. 2.3-6 in the
vicinity of the 30 deg value.

        The theoretical reduction in interference obtain-
able with the interference reduction technique adds to the
interference margin (i.e., the jamming-to-signal power
ratio (I/S)) of the receiver. Thus, if the receiver noise
level (N) is -201 dBW-Hz (Ref. 1) and the jammer power (I)
at the antenna is -110 dBW (corresponding to a 1 kW ground

jammer 10 km from user, see Section 3.1), the interference-to-noise ratio (I/N) is

$$\left(\frac{I}{N}\right)_{dB} = I_{dB} - N_{dB}$$

$$= -110 - (201) \text{ dB} \qquad (2.3-2)$$

$$= 91 \text{ dB}$$

From Fig. 2.3-6, this value of I/N corresponds to a reduction in interference at the output of the processor, of 199 dB for an interference at 60 deg and signal at 30 deg. The GPS receiver has an additional interference margin of 35 to 49 dB (Ref. 28). Thus, the total <u>theoretical</u> interference margin of the interference reduction processor-receiver system would be 234 to 248 dB.

Caution should be exercised in using these performance indices as they are based on an optimum interference reduction processor which may not be possible to implement. The finite nature of any implementation scheme (e.g., computer word size), non-ideal antenna beam patterns and radio frequency circuitry implementation problems may make it difficult to obtain these large reductions in interference.

The optimum processor assumes that the directions of the desired signal and interference as well as the interference-to-noise ratio are known. It may be unrealistic to estimate either the interference direction or strength. However, the direction of the desired signal is usually known. Several authors (Refs. 16 and 21) have proposed adaptive antenna array systems that are similar to the optimum interference reduction processor and do not require knowledge of interference direction or strength, but do require knowledge of signal structure or direction. Such a system has been built and tested using a four element linear array (Ref. 20).

The experimental performance of this system was close to
theoretical optimum. For I/N = 21.5 dB, the reduction in
interference-to-signal ratio was 42 dB. Thus, significant
reductions in interference were obtained with modest I/N
ratios.

Another possible approach to implementing the opti-
mum processor is to use an adaptive tracking technique (e.g.,
a phase lock loop) to keep the interference beam directed
toward the interference, while the GPS navigation computer
directs the main beam in the direction of the desired signal.
This technique may be easier to implement than the adaptive
antenna array system of the last paragraph, although it has
not been investigated here.

2.3.3 Applicability to GPS Manpack User

The GPS manpack user operating in a battlefield
environment is likely to encounter directional interference
such as jamming by the adversary. The interference reduc-
tion technique using an array of antennas as discussed in
the preceding section is capable of providing a significant
reduction in a user's vulnerability to jamming. The four
element array of the last section is less than 30 cm long
at the GPS navigation signal frequencies and thus physically
feasible. However, the implementation of this array may
require a considerable amount of signal processing equip-
ment in order to obtain the desired performance. This
equipment could be simplified if a two element array was
employed, at the expense of a reduction in performance.
The beam pattern of a two element array employing inter-
ference reduction is illustrated in Fig. 2.3-7. This fig-
ure indicates that the two element array has fewer nulls
and thus may be able to receive the navigation signals from
several satellites at the same time. However, the gain of
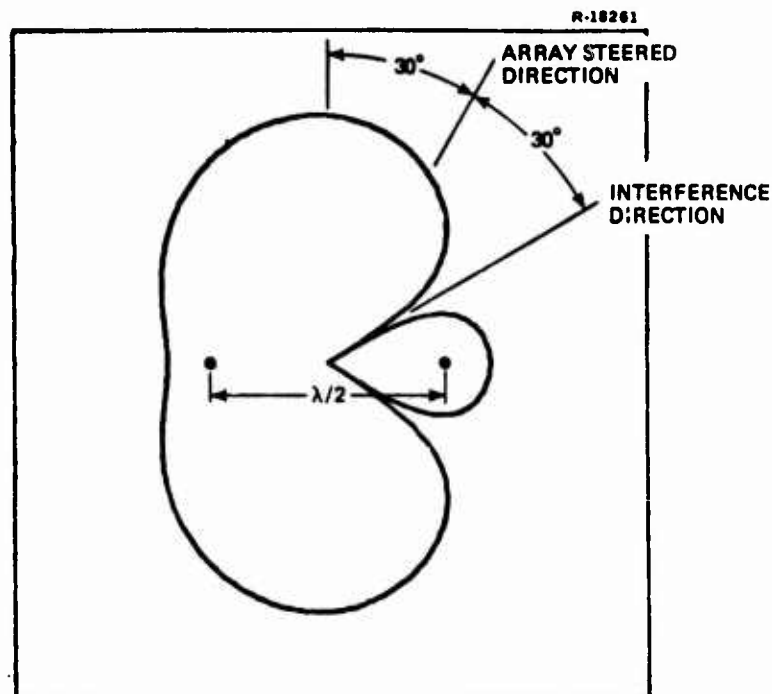
Figure 2.3-7   Two Element Beam Pattern With
                Interference Reduction

the array varies considerably with the direction of inter-
ference as illustrated in Fig. 2.3-8. Because of the low
margin in the GPS navigation signal power budget, this var-
iation in antenna gain may preclude the use of a two ele-
ment array. The reduction in interference which can be
provided by the two element array is illustrated in Fig.
2.3-9. This figure indicates that significant reduction
can be achieved as long as the difference in directions of
the desired signal and interference is greater than 30 deg.

        Two and four element "steerable null antenna pro-
cessors" for Army field communication systems are presently
being investigated by U.S. Army Electronics Command (Refs.
22 and 23). These systems are reported to be capable of
providing at least 35 dB reduction in interference.

43
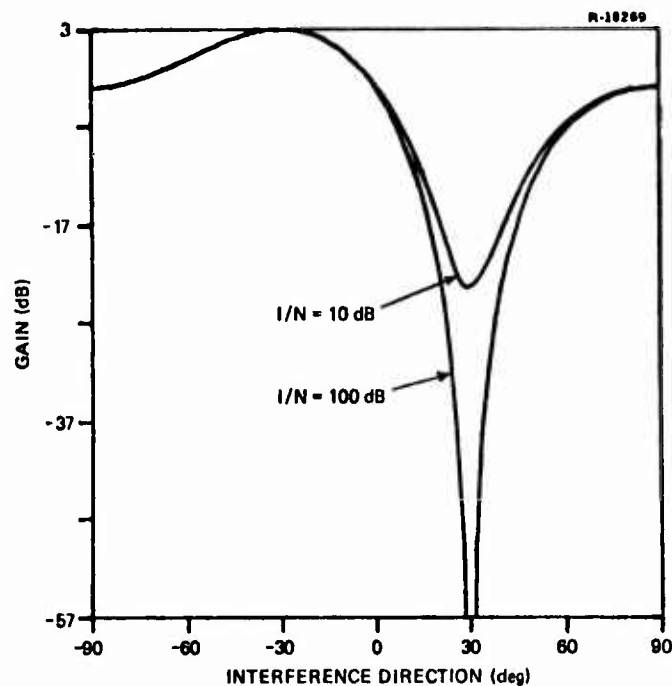
Figure 2.3-8   Array Gain With Interference Reduction
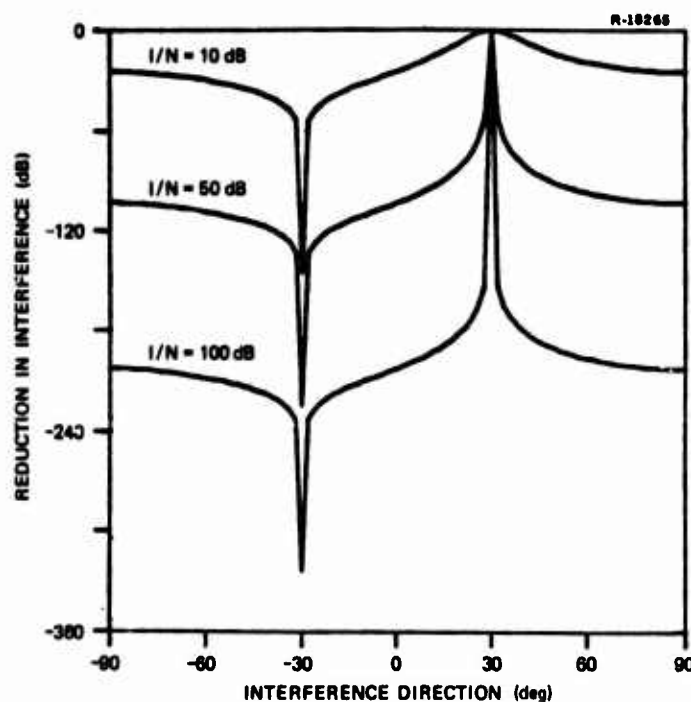
Figure 2.3-9   Theoretical Interference Reduction

44

Although these processors are designed for lower frequencies than that of the GPS navigation signal, their design could be modified to operate at L-band. Thus modified, these processors appear to be feasible for GPS manpack users, although details of their performance remain to be investigated.

It thus appears that interference reduction using antenna arrays are feasible for GPS manpack users. Additional studies of possible methods of implementing the optimum interference processor are required in order to determine the feasibility of obtaining performance that is suitable for the GPS user as well as to estimate the costs of such a processor.

2.4   ANTENNA DEPLOYMENT PROCEDURES

The directional antennas considered in this report require proper orientation and deployment in order that the user computer can select those satellites that are within the main beam of the antenna. This section discusses these deployment procedures for three types of directional antennas considered in this report. These are the wide beam and narrow beam directional antennas and the array antenna.

2.4.1 Wide Beam Antenna Deployment

The wide beam antenna used in the preceding performance studies is assumed to be a vertically pointed parabolic type with a beamwidth of 120 deg. This antenna should be mounted on an adjustable tripod with a two-axis leveling device, such as plumb bob or bubble level, which is capable of positioning the antenna to point vertically. The receiver is then activated.

45

2.4.2 Narrow Beam Antenna Deployment

The narrow beam antenna is also assumed to be a
parabolic type but with a very narrow beamwidth. This an-
tenna is manually positioned by the user to sequentially
point to individual satellites. This will again require
mounting the antenna on a tripod with a two-axis leveling
device. In addition, a measure of both elevation and azi-
muth angles must be provided.

The deployment procedure for the narrow beam an-
tenna again consists of unpacking and assembling the antenna
and tripod and connecting to the receiver with the cable.
The tripod and antenna are then leveled and the antenna
azimuth aligned with a reference direction (e.g., magnetic
north) using a compass. The user GPS navigation computer
is then turned on and queried as to the vertical and azi-
muth angles at which the antenna should be positioned to
receive the desired satellite navigation signal. The
antenna is then set to these angles and the receiver turned
on. If the navigation signal is received, the user can be
so notified and the measurement taking commenced. If the
signal is not received, the measurements can be skipped,
and an attempt made to locate another satellite. After a
sufficient set of measurements has been taken, the antenna
can be repositioned to the next satellite as directed by
the computer. The exact procedure for operating the GPS
navigation computer/receiver and antenna will depend upon
their implementation; however, the procedure outlined above
is typical of what must be done to use a narrow beam antenna.

2.4.3 Array Antenna Deployment

The deployment procedures for the array antenna
will depend upon the number of elements and the physical

46

construction of the array. Assuming the array elements are
arranged in either a line or planar geometry, the deploy-
ment procedure will be similar to that for the wide beam
antenna. However, the axis of the array must be aligned
with a reference direction (e.g., magnetic north).

The deployment procedure for the array antenna con-
sists of unpacking and assembling the antenna and tripod
and connecting the antenna to the receiver. The antenna is
then leveled and the axis aligned with the reference direc-
tion. The receiver is then activated and measurements pro-
cessed. Some implementations of the interference reduction
processor may require operator assistance in identifying
probable directions of jammer signals, in which case the
operator would input the direction of the battlefront or
his best estimate of the jammer direction. Sequencing from
satellite-to-satellite could be accomplished automatically,
under computer control.

3.   USER VULNERABILITY AND THREAT COUNTERING

        The ground-based users of GPS, such as the Army man-
pack user, are likely to be operating in a battlefield envi-
ronment where electronic jamming of the GPS navigation sig-
nal is present. The degree of vulnerability of the GPS
user will depend upon his location relative to the jammer,
the power of the jammer, the jamming signal structure, etc.
The user may be able to employ threat countermeasures to
reduce his vulnerability to jamming and other directional
interferences.

        This chapter considers the vulnerability of ground-
based users of GPS and some possible threat countering tech-
niques. The scenario and threat models used to evaluate
user vulnerability are presented in Section 3.1. Included
in this section are a discussion of the effectiveness of
various jamming signals and the jamming signal degradation
due to the propagation path between jammer and user. Sev-
eral techniques for countering the jammer threat are pre-
sented in Section 3.2. Finally, an evaluation of the
vulnerability of a GPS manpack user to electronic jamming
for the threat models and scenarios of Section 3.1 is pre-
sented in Section 3.3. The effectiveness of the threat
countering techniques of Section 3.2 is also discussed.

3.1 SCENARIOS AND MODELS

        The scenarios and models used in the evaluation
of the GPS manpack user vulnerability to electronic jamming

48

are discussed in this section. These scenarios and models were designed to provide a realistic assessment of user vulnerability to jamming.

3.1.1 Scenarios

This study is concerned with an Army manpack GPS user in a battlefield environment where jamming is present. The user is assumed to be stationary with his antenna located 2 m above ground level. This antenna is initially assumed to be the conventional antenna defined in Chapter 2; however, directional antennas will also be considered. The receiver is a Y-model (Ref. 24) capable of operating with a jammer power-to-navigation signal power ratio (J/S) of 34 dB to 49 dB, depending upon operating mode (i.e., initial signal acquisition, carrier tracking, etc.), and a receiver input signal level (P-code) greater than -163 dBW.

The interference rejection capability of a receiver or its threshold jammer-to-signal power ratio is heavily dependent upon the receiver design. Since this study was not concerned with receiver design, the values of this threshold used are the minimum values as specified by the Air Force (Ref. 24). Thus, the vulnerability results presented here are for worst case threshold values. Improved values may be possible with particular receiver designs, thus reducing the user vulnerability presented in this report.

The electronic jammer is assumed to emit a radio frequency continuous wave (CW) signal at the frequency of the primary GPS navigation signal (i.e., 1575.42 MHz), which is directed toward the GPS user. Two jammers will be considered in this report. One is a ground-based jammer with an antenna height of 10 m and the other a standoff

49

airborne jammer with an altitude of 3 km. The jammer ef-
fective isotropic radiated power (EIRP) will be treated as
a parameter, but within limits of 1 W to 100 kW. Further
details of the jammer are given in Section 3.1.2.

The signal path between the jammer and the user is
initially assumed to be a clear (i.e., unobstructed) path.
However, consideration is given to the effects on user
vulnerability of obstruction in the signal path, such as
an RFI (radio frequency interference) screen. Further de-
tails of the signal path are given in Section 3.1.3.

3.1.2 Threat Models

There are several signal structures that a jammer
can radiate in order to deny user access to GPS. The effec-
tiveness of these signals depends upon the user antenna and
receiver configuration. The GPS navigation signal is a
continuous sine wave bi-phase modulated with a ranging and
data code sequence. The GPS receiver mixes or correlates
this signal with a similar reference code sequence and, if
these code sequences match, correlation is achieved, thus
removing the phase modulation and producing the original CW
signal with power equal to that of the received signal (S).

The jammer could attempt to emulate the GPS naviga-
tion signal by transmitting a similar bi-phase modulated sig-
nal. However, unless the jammer code sequence is identical
to the navigation signal code sequence that the receiver is
searching for or tracking, no correlation is achieved. In
fact, when this or similar noise-like jamming or interference
signals are mixed with the receiver reference, the range of
their frequency spectrum is spread or increased by an amount
(Ref. 25) equal to the bandwidth of the reference code
sequence (which is equal to twice the ranging code

50

sequencing or chipping rate), and thus its power is distributed over a wider frequency spectrum. Since the correlator is followed by a very narrow band filter, the effective jammer power will be reduced by the amount its spectrum is spread.

Since interference signals are spread across the GPS band, an effective jamming signal is one whose power is concentrated in a very narrow frequency spectrum within this band. A continuous sine wave (CW) signal satisfies this requirement and is thus an effective jamming signal (disregarding potential countering techniques such as the notch filter described in Section 3.2). The jamming threat used in this study is thus assumed to be radiating a CW signal in all directions with an EIRP of from 1 W to 100 kW. Other jamming signals (e.g., pulse) may be equally effective. The objective here was to evaluate a number of jammer deployment methods and countering techniques for a single, representative jammer signal structure.

3.1.3 Propagation Path Models

To provide a realistic assessment of the vulnerability of GPS users to jamming, the factors which influence the propagation of radio waves between the jammer and user must be considered. These factors limit the effective range within which the jammer can deny a user access to GPS and are particularly important to the ground-based users.

The earth is the most important factor influencing radio wave propagation, especially for ground-based GPS users and jammers. It provides a surface to reflect the waves and, because of its curvature, limits line-of-sight distances for direct propagation of waves. The principle mechanism for propagation of radio waves at GPS frequencies

51

is the tropospheric wave, which travels in the lower 15 km of the earth's atmosphere. There are several paths by which this wave may travel between a transmitter and receiver; these paths can be divided into two regions, within line-of-sight and beyond line-of-sight. Within line-of-sight, the wave normally has two components. One travels <u>directly</u> from transmitter to receiver, while the other reaches the receiver as a result of <u>reflection</u> from the surface of the earth. Beyond line-of-sight, the wave is <u>diffracted</u> around the curvature of the earth. Well beyond the line-of-sight the wave can be reflected from <u>scatterers</u> in the upper troposphere. In addition, within either region, the wave is influenced by the composition of the atmosphere and by foliage, if present. A summary of these propagation paths is presented in Table 3.1-1.

TABLE 3.1-1

PROPAGATION PATHS

REGION	PATH
Within Line-of-Sight	● Direct ● Reflection
Beyond Line-of-Sight	● Diffraction ● Tropospheric Scatter
Either of above	● Atmosphere ● Foliage

The amount of energy loss by a wave traveling through these different paths is a function of distance traveled, antenna heights, wavelength, composition of the earth's surface and atmosphere, etc. This transmission or propagation loss can be computed using theoretical models and empirical data. Details of the models and data used to compute propagation path losses is given in Appendix D.

52

The propagation loss for jammer signals to the ground-based user is illustrated in Fig. 3.1-1. Two curves are presented; one for the ground jammer and one for the airborne jammer. Also illustrated is the propagation loss that occurs in <u>free space</u>. Within line-of-sight, the total propagation loss can be less than the free space loss due to the reinforcement of the direct wave by the reflected wave. Beyond line-of-sight, propagation loss increases rapidly, although high-powered jammers may still be effective. Further details on the origin of these curves are given in Appendix D. These propagation loss characteristics will be used in the evaluation of GPS manpack vulnerability to electronic jamming, in Section 3.3. <u>These curves assume a smooth earth's surface and do not include attenuation due to foliage</u>. Detailed data on foliage attenuation at the GPS navigation signal frequencies is presently not available.

R-16227
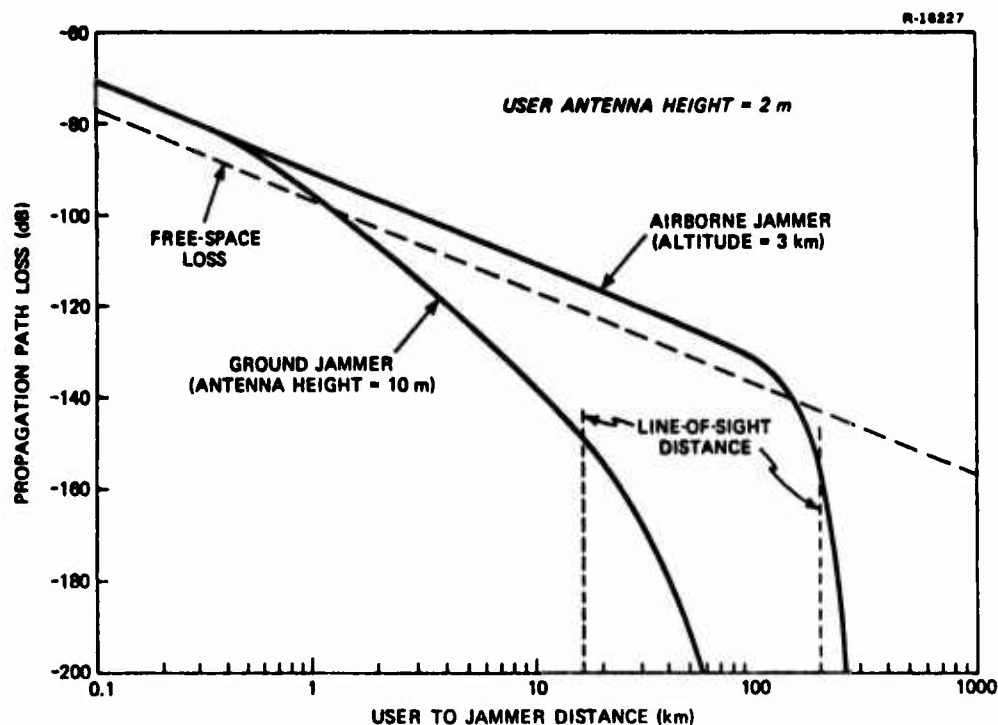
Figure 3.1-1   Propagation Path Loss

53

3.2 THREAT COUNTERING TECHNIQUES

In a severe jamming environment, the GPS user may be able to employ threat countering techniques to reduce his vulnerability to jamming. Several of these techniques are discussed and evaluated in this section. It is assumed that the GPS satellite power and navigation signal structure are fixed. The techniques considered in this discussion are restricted to those a user can influence through design of the receiver or through design of auxiliary equipment. The former techniques are classified as internal to the receiver, while the latter are classified as external to the receiver.

3.2.1 Internal

The baseline GPS user receiver characteristics assumed for this discussion are specified in Ref. 24. There are several modifications which can be made to this baseline receiver to reduce its vulnerability to electronic jamming by increasing its threshold jammer power-to-signal power ratio. Two techniques that appear promising are notch filters and reduced tracking filter bandwidth.

Notch Filter — This technique reduces the jamming or interference signal by placing a "notch" in the passband of the receiver's input filter (hence the term notch filter) at the jamming signal frequency, thus attenuating the jamming signal. If the notch is very narrow, only a small amount of the desired signal energy would be reduced, with a small degradation of user performance (Ref. 26). This technique is most effective against a CW jammer, allowing a 30 to 40 dB reduction in jammer power. Notch filters require a mechanism for acquiring and tracking the jamming signal. The most promising mechanism for doing this is a phase-lock-loop (Ref. 26). However, this adds complexity

54

to the receiver and may increase its cost substantially. Furthermore, the jammer may defeat a notch filter by modulating his CW signal, although this increases the jammer complexity and may decrease its effectiveness. A detailed investigation of this technique of threat countering has yet to be performed.

Reduced Bandwidth — The bandwidths of the baseline GPS receiver in the various operating modes are chosen to provide reasonable performance for dynamic users. However, the manpack user will normally be stationary, so that his receiver bandwidth could be narrower than that required for dynamic users. The bandwidth of the carrier tracking loop could easily be reduced. A representative proposed design calls for a 21 Hz carrier tracking loop bandwidth (Ref. 27). This bandwidth could be reduced to 1 or 2 Hz (and perhaps less*) for the manpack user. Reducing the carrier tracking loop bandwidth to 1 Hz from 21 Hz would result (Ref. 1) in a 13 dB increase in the receiver's threshold jammer-to-signal power ratio. (See Section 3.3.1 for further discussion of this ratio.) However, some receiver designs may not allow this much improvement, while others may provide for an even greater improvement. Thus, for evaluation purposes, the range of 10 to 15 dB will be used. Reducing the receiver bandwidth during initial acquisition would result in a longer navigation signal acquisition time period. For example, using the search strategy discussed in Ref. 1, reducing initial acquisition bandwidth from a nominal 1 kHz to 10 Hz would result in the acquisition time increasing by a factor of 100. Although this would result in a 20 dB increase in interference margin, the time factor is considered to be unrealistic. Thus, reducing the receiver bandwidth during initial acquisition is not considered feasible.

---

*Usable bandwidths are highly dependent on oscillator instabilities.

55

3.2.2 External

Several techniques have been suggested for reducing user vulnerability with auxiliary equipment. The basic idea is to reduce the sensitivity of the GPS user antenna to the directional interference or jamming signal, thus reducing the power level of this interference at the receiver input. The techniques to accomplish this that are considered in this discussion are directional antennas and RFI screens.

Directional Antennas — The user's vulnerability to jamming can be reduced if his antenna is insensitive to signals coming from the direction of the interference or jamming. This can be accomplished through use of directional antennas such as parabolic reflectors or antenna arrays, as discussed in Chapter 2. If the parabolic antenna can be positioned so that the interference is outside the main lobe, then typically the interference power level will be reduced 20 to 25 dB (Ref. 15), relative to that of the desired navigation signal. If an antenna array with null steering were employed, the interference power level could be reduced 35 to 40 dB, as discussed in Section 2.3. Thus, depending upon the type of directional antenna deployed, reductions in the receiver jamming-to-signal power ratios of 25 to 40 dB are possible. Multiple jammers may present problems. However, an antenna array with null steering can be effective against these multiple jammers at the expense of antenna gain and increased processor complexity.

RFI Screens — If the direction of the interference were known, an RFI screen could be placed between the user antenna and the interference. This screen would act to reduce the power level of the interference, the amount of reduction depending upon the size of the screen and distance

between this screen and the user antenna. According to
knife-edge diffraction loss theory (Ref. 15), if this screen
were at least 3 m high and 10 m long with the user 6 m from
the screen, the interference power level would be reduced
by approximately 25 dB. In practice, the actual loss may
be less than this, due to reflections from buildings, hills,
etc., but the size of the screen could be increased to com-
pensate. Empirical data (Ref. 15) indicates that if the
user antenna is behind a hill 15 m high, the loss in inter-
ference signal strength would be about 23 dB. Thus, a 20
to 25 dB loss with an RFI screen may be feasible. However,
deployment of such a screen may be difficult and thus limit
its usefulness. This was not investigated in this study.

3.2.3 Threat Countering Effectiveness

The effectiveness of the threat countering techniques
discussed in the preceding sections is summarized in Table
3.2-1. Threat countering effectiveness is measured by the
amount of reduction that is possible in the user receiver
jamming-to-signal power ratio. Several of these techniques
could be combined to provide further reduction in interference

TABLE 3.2-1

THREAT COUNTERING EFFECTIVENESS

TECHNIQUE	THRESHOLD JAMMING-TO-SIGNAL POWER RATIO IMPROVEMENT (dB)
Notch Filter	30-40
Reduce Bandwidth	10-15
Directional Antennas	20-25
Null Steering Antennas	35-40
RFI Screens	20-25

57

levels. Further evaluation of the effectiveness of these threat countering techniques will be made in the following section, where the reduction in the range at which the receiver is jammed will be illustrated.

3.3 USER VULNERABILITY EVALUATION

The vulnerability of a GPS manpack user to electronic jamming is evaluated in this section for the scenario and models of Section 3.1. The criteria used for this evaluation is the critical jammer range. This is defined as the range (distance) from the jammer within which a user would be denied access to the GPS navigation signals, since the jamming signal is effectively "overpowering" the navigation signals in the user receiver.

The jammer or interference level at the user receiver is computed in Section 3.3.1 using the propagation path losses given in Section 3.1.3 for the ground and airborne jammers. The critical jammer range is then computed from this data and presented in Section 3.3.2. The effectiveness of the threat countering techniques discussed in Section 3.2 in reducing the critical jammer range is discussed in Section 3.3.3. Finally, the results of the evaluation are summarized in Section 3.3.4.

3.3.1 Interference Level

The GPS navigation signal structure provides inherent interference rejection because of the spread spectrum modulation technique used. However, the amount of interference rejection available also depends upon the receiver and the particular operating mode employed. There are basically three operating modes for a GPS receiver:

58

- Initial signal acquisition
- Data acquisition
- Carrier tracking (normal navigation mode)

Each of these operating modes will have a particular interference rejection capability depending upon the receiver design. The first of these modes usually has the least amount of interference rejection, the second an intermediate capability, while the third has the greatest. Thus, subsequent discussion only considers the interference rejection capability of these two extremes, that is, initial signal acquisition and carrier tracking. The data acquisition interference rejection capability occurs within these extremes.

A measure of receiver interference rejection capability is the threshold jammer-to-signal power ratio. As long as the power of the jamming signal is such that this power ratio (or threshold) is not exceeded, the receiver will operate in the mode that corresponds to that threshold. However, if the jamming signal, in relation to the navigation signal level, is such that a particular threshold is exceeded, the receiver will not operate in the corresponding mode. Thus, the threshold jammer-to-signal power ratio is an effective measure of user vulnerability to jamming.

The jammer-to-signal power ratio (J/S) at the receiver input is defined as follows (all terms are in dB) (Ref. 1):

$$\left(\frac{J}{S}\right) = P_j + L_p + G_{uj} - S \qquad dB \qquad (3.3-1)$$

where

P_j is the effective isotropic radiated power (EIRP) of the jammer in the direction of the user (includes jammer antenna gain)

L_p is the propagation path loss (given in Fig. 3.1-1)

G_{uj} is the gain of the user antenna in the direction of jammer

S   is the navigation signal power at the receiver

The GPS system specifications (Ref. 28) require the P-code navigation signal level (S) at the user antenna equal or exceed -163 dBW. Assuming the user antenna is isotropic so that G_{uj} = 0 dB, then Eq. (3.3-1) becomes

$$\left(\frac{J}{S}\right) = P_j + L_p + 163 \qquad dB \qquad\qquad (3.3-2)$$

This jammer-to-signal power ratio for a 1W (EIRP) jammer (i.e., P_j = 1W or 0 dBW) is illustrated in Fig. 3.3-1. For higher jammer powers, the vertical scale moves down by 10 dB for every order of magnitude increase in the jammer power over 1W. Note that this figure is the same as
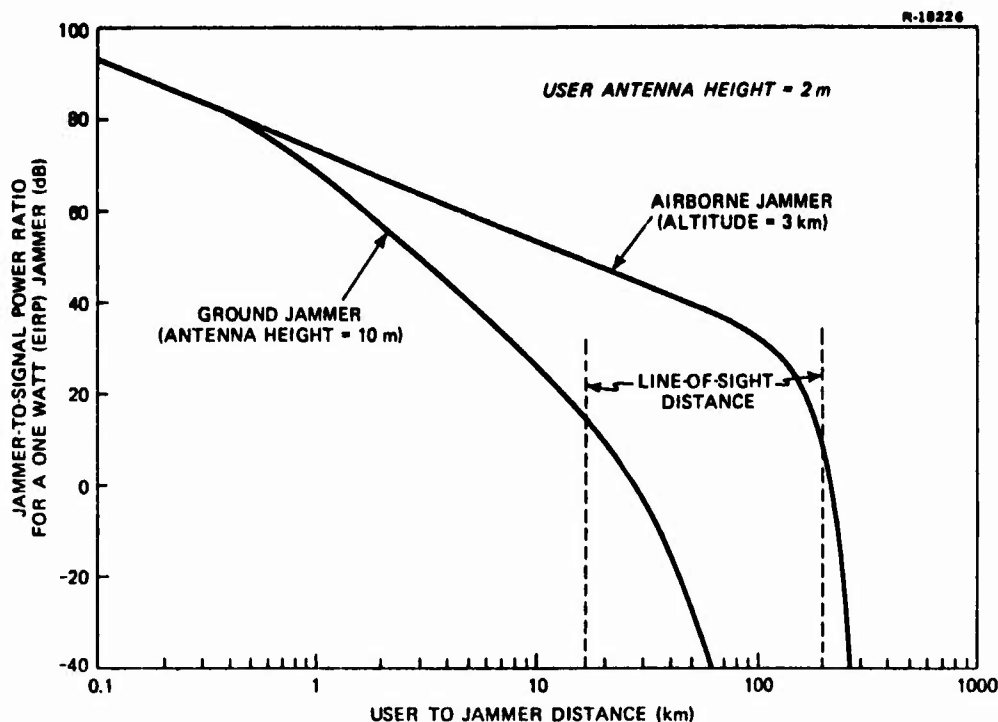
Figure 3.3-1   Jammer-to-Signal Power Ratio

Fig. 3.1-1, except the vertical scale has been increased by a factor of +163 dB to reflect the value of S in Eq. (3.3-2).

The effectiveness of the jammers tends to diminish rapidly beyond line-of-sight, especially for the airborne jammer. The effectiveness of the ground jammer decreases more rapidly than that of the airborne jammer due to the higher interaction between direct and reflected waves in the former case.

Because the army manpack user may be jammed most of the time in a battlefield environment, his receiver's most critical operating mode is the initial acquisition of the navigation signal. In this mode the receiver bandwidth is quite wide because of the initial large uncertainty in the navigation signal frequency. Thus, the receiver interference rejection capability or threshold jammer-to-signal power ratio is lowest in this operating mode. A minimum value for this power ratio is $J/S = +34$ dB (Ref. 24). In Fig. 3.3-1, it can be seen that this value of J/S is exceeded whenever the user is within 7 km of the 1W ground jammer or 90 km of the 1W airborne jammer. Larger values of jammer power will extend these ranges as will be illustrated in the next section.

If the jammer signal appears while the receiver is in the tracking mode, the critical jammer range is less than that of the acquisition mode. The minimum threshold jammer-to-signal power ratio for a receiver in the tracking mode is $J/S = 49$ dB (Ref. 24), since the receiver carrier bandwidth is very narrow. This value of J/S is exceeded whenever the receiver is within 3 km of the 1W ground jammer and 16 km of the 1W airborne jammer. Thus, the critical jammer range is decreased significantly when the receiver is in the tracking mode.

61

In the next section, the critical jammer range is illustrated as a function of jammer power for the two receiver operating modes discussed above.

3.3.2 Critical Jammer Range

The discussion in the preceding section illustrated the dependence of the user's vulnerability on receiver operating mode. The dependence of user vulnerability on the jammer power is illustrated in this section. The parameter of interest is the critical jammer range which is the range from the jammer at which a given threshold jammer-to-signal power ratio occurs. Two threshold jammer-to-signal power ratios are of interest, that for initial acquisition, which is assumed to be $J/S = 34$ dB, and that for carrier tracking, which is assumed to be $J/S = 49$ dB (Ref. 24).

The critical jammer range as a function of jammer power for these two threshold jammer-to-signal power ratios and the ground and airborne jammers is illustrated in Fig. 3.3-2. The ground jammer has the lowest critical jammer range as noted in the previous section. An especially interesting result from this curve is that jammer powers greater than 1000 W does not result in a significant increase in the critical jammer range for the airborne jammer.

3.3.3 Vulnerability Reduction

Although the GPS receiver has an inherent inter ference rejection capability, a user with the baseline receiver (especially the Army manpack user) is still vulnerable to jamming with relatively simple jammers, as the previous sections have shown. Therefore, threat countering techniques are extremely important. Since these
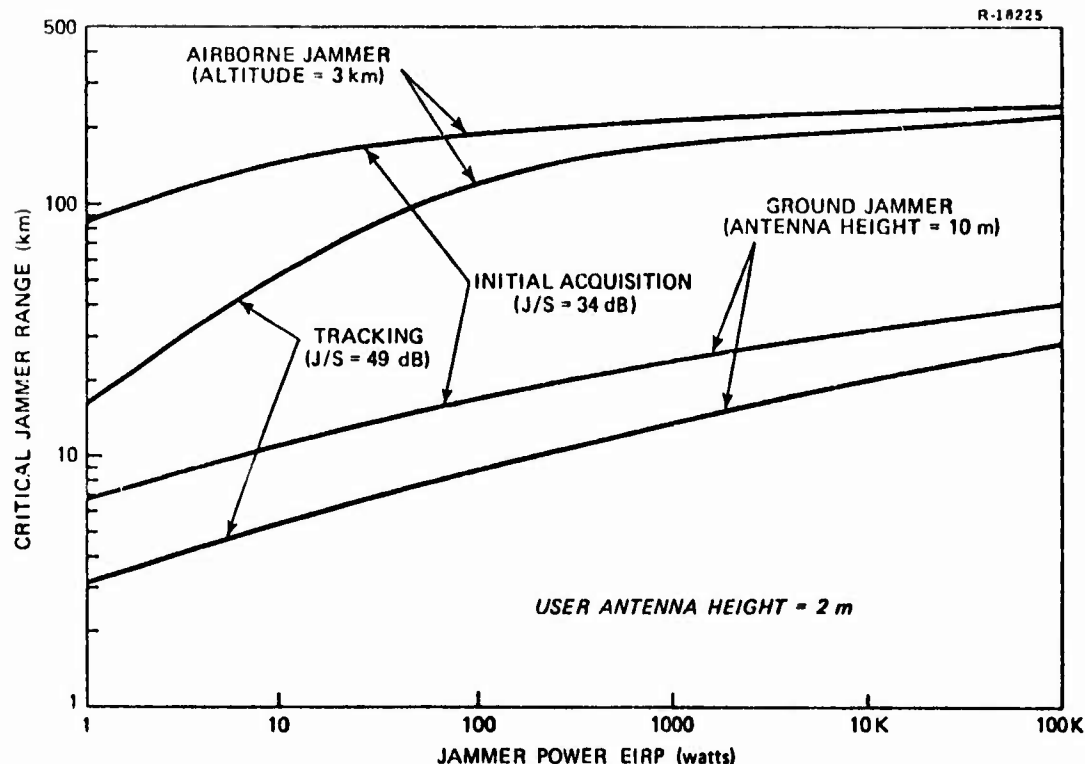
Figure 3.3-2   Critical Jammer Range

techniques effectively increase the user receiver threshold
jammer-to-signal power ratio, they can decrease the criti-
cal jammer range. Assuming 1 kW EIRP jammers, the critical
jammer ranges for users with and without the threat counter-
ing techniques discussed in Section 3.2 are summarized in
Table 3.3-1. Critical jammer ranges are given for the re-
ceiver in the initial acquisition and carrier tracking modes
for both the ground and airborne jammers. The critical jam-
mer range for the combined utilization of reduced receiver
bandwidth and RFI screen is also given.

     These results indicate that against a ground-based
jammer, an RFI screen and/or reduced bandwidth are about as
effective as the other techniques. Against an airborne
jammer, the notch filter and null steering antenna are the

63

TABLE 3.3-1

THREAT COUNTERING EFFECTIVENESS

THREAT COUNTERING TECHNIQUE	CRITICAL JAMMER RANGE (km)			
	GROUND JAMMING (1 kW EIRP)		AIRBORNE JAMMER (1 kW EIRP)	
	Initial Acquisition (J/S = 34 dB)	Carrier Tracking (J/S = 49 dB)	Initial Acquisition (J/S = 34 dB)	Carrier Tracking (J/S = 49 dB)
Baseline	24	14	210	170
Notch Filter	4-7	2-3	30-90	5-16
Reduced Bandwidth	N/A	7-9	N/A	90-120
Directional Antenna	9-11	4-5	120-150	30-50
Null Steering Antenna	4-5	2	30-50	5-8
RFI Screen	9-11	4-5	120-150	30-50
Reduced Bandwidth and RFI Screen	9-11	2-3	120-150	5-16

most effective. Reducing the bandwidth of the carrier loop in
the receiver is effective, and is the simplest threat count-
ering technique for a stationary user, although it can only
be used when the receiver is in the tracking mode.

3.3.4 Vulnerability Evaluation Summary

The GPS user is quite vulnerable to electronic jam-
ming from both a ground-based and an airborne jammer. This
is especially true for the Army manpack user since he will
most likely be attempting to acquire the GPS navigation sig-
nals when jamming is present. The results of this study
indicate that in the initial acquisition mode with a ground
jammer radiating 1 kW EIRP, the user will not be able to
operate within 24 km of the jammer without special threat
countering equipment. If the user were behind an RFI screen
of 3 m height, this critical jammer range could be reduced
to approximately 10 km.

If the jammer is airborne, the user is even more
vulnerable. In the initial acquisition mode, the critical
jamming range is approximately 210 km. The most effective
threat countering technique in this case is either the notch
filter or the null steering antenna.

4.   RECEIVER CLOCK ERROR ANALYSIS

        This chapter develops a model describing environ-
mentally-induced errors in a quartz crystal oscillator. The
error model is utilized to assess the degradation in GPS
navigation performance, for an airborne (helicopter) user,
arising from the use of the receiver oscillator (clock) in a
realistic (non-ideal) environment.

4.1 RECEIVER CLOCK ENVIRONMENTAL ERROR MODEL

    4.1.1 Introduction

        To properly assess the impact of environmentally-
induced quartz crystal oscillator errors on GPS navigation
performance, a comprehensive model of the oscillator error
behavior must be developed. This section describes the de-
velopment of an error model which considers the effects of
the environment on a quartz oscillator. The complete error
model will include a description of the intrinsic stability
of the oscillator as well as the environmentally-induced
errors. The model for intrinsic stability follows directly
from a consideration of the frequency stability of a specific
oscillator. (This model is developed in Appendix C, which
also includes background discussions of frequency stability
and the modeling of flicker noise.) The Hewlett Packard
(HP) 10544A quartz crystal oscillator will be utilized
throughout this study as a representative device. The
model describing environmental effects is based upon en-
vironmental performance data supplied by Hewlett Packard
and the U.S. Army Electronics Command.

The prototype for the quartz crystal oscillator error model to be considered is shown in Fig. 4.1-1 with

$\delta\phi(t)$ = total clock phase error in seconds at time t

$\delta\phi(t_0)$ = initial phase error (seconds)

$\delta f(t_0)$ = initial fractional frequency offset (dimensionless)

$\dot{\delta f}(t_0)$ = initial fractional frequency drift or "aging" (seconds^{-1})

q_f = spectral level of white noise driving the flicker noise model (dimensionless)
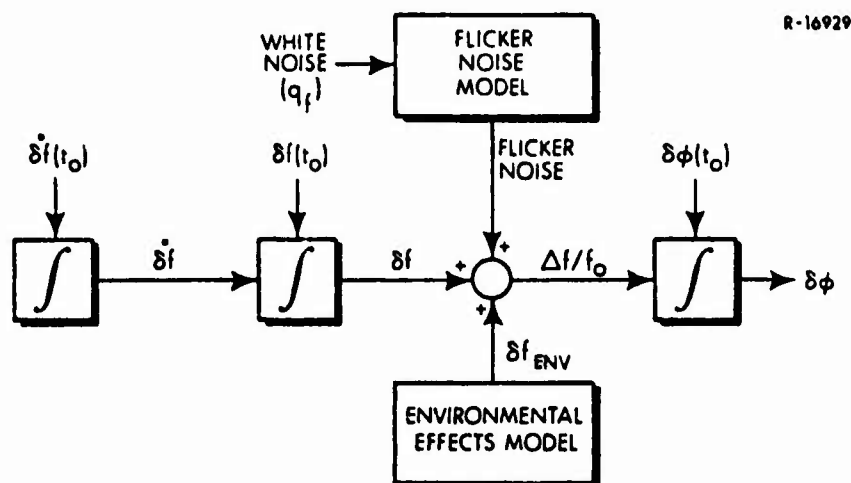
Figure 4.1-1   Prototype Quartz Crystal Oscillator Error Model

The initial phase and fractional frequency errors, $\delta\phi(t_0)$ and $\delta f(t_0)$, respectively, are dependent upon the specific application in which the oscillator is to be used. For this reason, specific values for these random variables will be deferred until the discussion of the performance projections in Section 4.2. The initial condition characterizing the "aging" of the oscillator can be specified and is computed in Section C.3 along with the spectral level (q_f) of

67

the white noise in the flicker noise model. The environmental
effects model is developed in the next section.

4.1.2 Modeling of Environmental Effects

Any complete time standard error model must contain
a description of the effects the environment has on the per-
formance of the oscillator. A completely general error model
for environmental effects would be prohibitively complex.
However, if certain assumptions are made about the form and
number of environmental influences, then an environmental
effects model can be developed for a specific device. In
the following paragraphs, the effects of temperature, warm-
up, acceleration, vibration and shock on a quartz crystal
oscillator (HP 10544A) will be discussed.

Temperature — A quartz oscillator responds to a
change in ambient temperature with a shift in frequency.
The magnitude of this nonlinear effect is shown in Fig. 4.1-2
for an HP 10544A oscillator. (The fractional frequency change
is shown as an excursion from the oscillator frequency at
30°C.) When the oscillator is utilized in a GPS receiver, a
linearized coefficient relating the frequency shift to a
temperature change can be obtained. For temperature excur-
sions about the nominal operating temperature of the GPS re-
ceiver (assumed to be $\approx 60^{O}$C, from Ref. 7), this temperature
drift coefficient (K_{tv}) is linear with a maximum value (see
oscillator Serial No. 1410), $K_{tv} = 1 \times 10^{-10}/^{O}$C. <u>Figure 4.1-2
illustrates the wide variation in temperature drift coeffi-
cients for differing devices of the same type</u>.

The frequency shift which results from a tempera-
ture change does not occur instantaneously due to a "thermal
lag." The temperature-regulating oven surrounding the quartz
crystal is the main contributor to this lag. The thermal

68
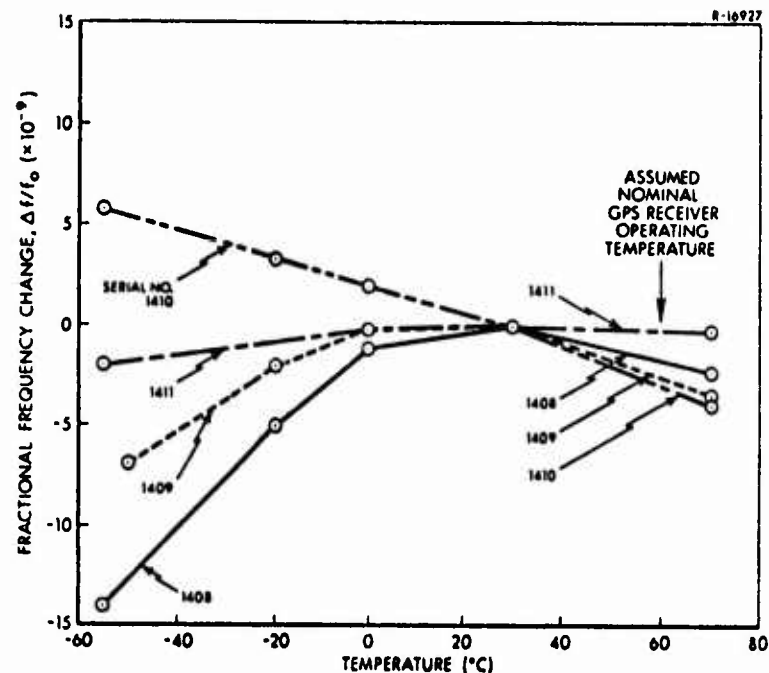
Figure 4.1-2   Frequency-Temperature Characteristic of
                  Selected HP 10544A Oscillators (Ref. 6)

response shown in Fig. 4.1-3 can be adequately described by
the simple first-order system shown in Fig. 4.1-4.   The time
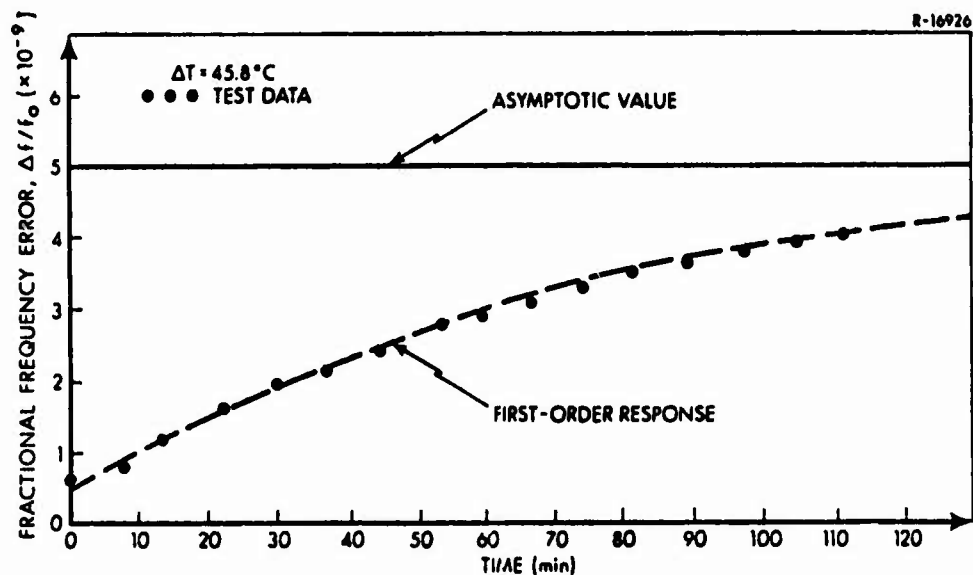
Figure 4.1-3   Response of Crystal Oscillator Frequency to
                  a Step Ambient Temperature Change (Ref. 7)
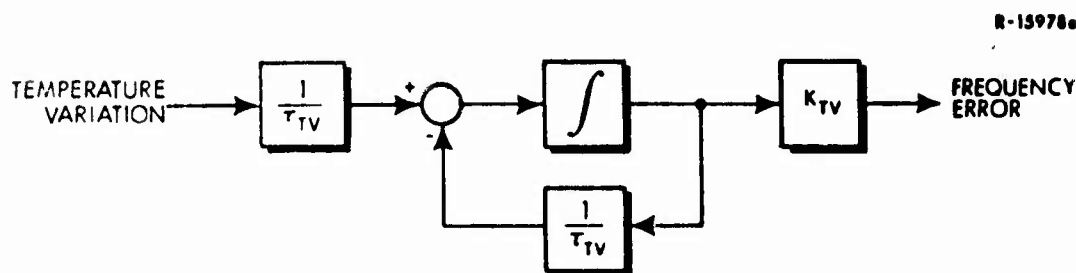
Figure 4.1-4   Temperature Variation Error Model

constant, τ_{tv}, depends upon the number of ovens surrounding the crystal. For a single oven device (such as the HP 10544A), this time constant (τ_{tv}) is on the order of 80 minutes (see Fig. 4.1-3).

The error model shown in Fig. 4.1-4 represents the response of the crystal oscillator to an arbitrary temperature variation. To utilize this model, the input temperature variation must be described quantitatively. It is obvious that differing users (e.g., manpack, helicopter, winged aircraft) will encounter vastly different environmental conditions; e.g., a manpack user moves from a heated room to a subfreezing field location, an aircraft climbs from sea level to cruising altitude, etc. These dissimilar environmental scenarios will result in mission-dependent temperature fluctuations outside the GPS receiver. These variations are not transmitted instantaneously to the crystal oscillator due to the moderating influence of the receiver thermal mass. Assuming random temperature variations, the ambient temperature surrounding the crystal oscillator is reasonably modeled as a first-order Markov process. The parameters of the process, rms value and time constant, must be chosen to reflect the temperature variations outside the GPS receiver and the moderating effect of the receiver. A composite thermal error model is given in Fig. 4.1-5. For a GPS
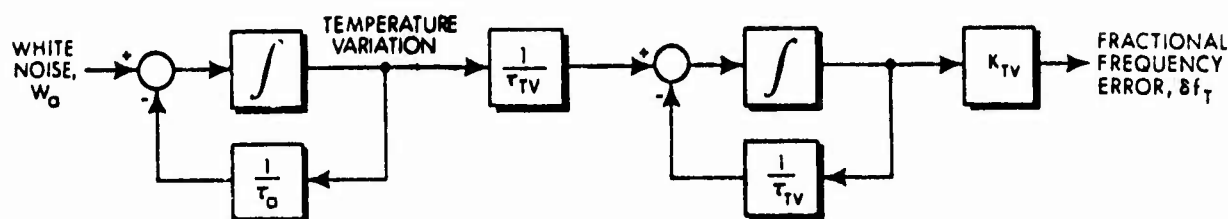
Figure 4.1-5   Quartz Crystal Thermal Error Model

receiver, the rms value of the temperature fluctuations near the crystal oscillator is expected to be on the order of $3^{\circ}C$ with a time constant (τ_a) of 100 minutes (based on Ref. 7). The corresponding spectral level of the white noise (q_a) is $3 \times 10^{-3} \, {}^{\circ}C^2/sec$.

Warm-up − Figure 4.1-6 shows the fractional frequency error versus warm-up time characteristics of three HP 10544A quartz crystal oscillators. The three oscillators exhibit vastly different behavior which is not amenable to direct analysis. The dashed line in the figure describes
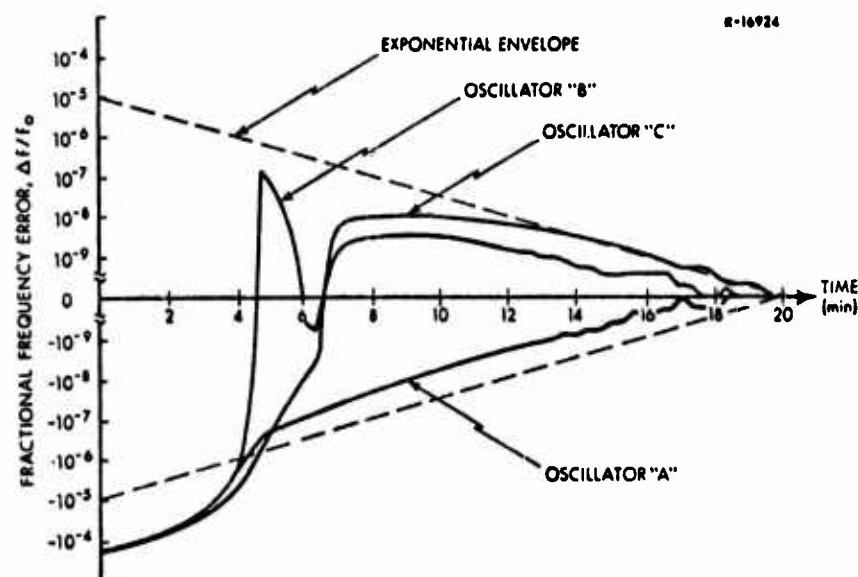
Figure 4.1-6   Warm-up Characteristic of HP 10544A
Quartz Crystal Oscillator (Ref. 6)

71

an exponentially decaying envelope (the plot is semi-log) which can be viewed as a statistical bound on the frequency error. The warm-up fractional frequency error variance ($\sigma^2_{\delta fw}$) for this exponential model is

$$\sigma^2_{\delta fw} = \sigma^2_w e^{-2t/\tau_w} \tag{4.1-1}$$

with $\sigma^2_w = 1 \times 10^{-10}$ and $\tau_w \simeq 100$ seconds. The warm-up time constant, τ_w, is much less than τ_{tv} since, during warm-up, the response is primarily that of the crystal without the moderating effect of the oven.

Acceleration — A constant acceleration introduces a frequency offset in a quartz oscillator proportional to the magnitude of the acceleration, i.e., $\delta f_a = K_g |\underline{a}|$. The coefficient of the proportionality, K_g, is dependent upon the orientation of the acceleration vector with respect to the crystallographic axes of the quartz crystal. A worst case value is $K_g = 1 \times 10^{-9}/g$ (Ref. 7).

Vibration — Vibration introduces sidebands (at the vibration frequency) into the spectrum of the signal from a quartz crystal oscillator. These sidebands produce a frequency error which is dependent upon the oscillator sensitivity at the vibration frequency. Measurements have been made of the fractional frequency error (averaged over a 10-second interval) arising from the lateral vibration of a quartz crystal oscillator (Ref. 7). Figure 4.1-7 shows the measured response to a sinusoidal input similar to the vibration specification (Curve M) in MIL-STD-810B. The worst case response is adequately modeled by the resonant second-order curve which is superimposed upon the data. In lieu of a well-defined spectrum for the vibration in an operational environment, a baseline model will be developed
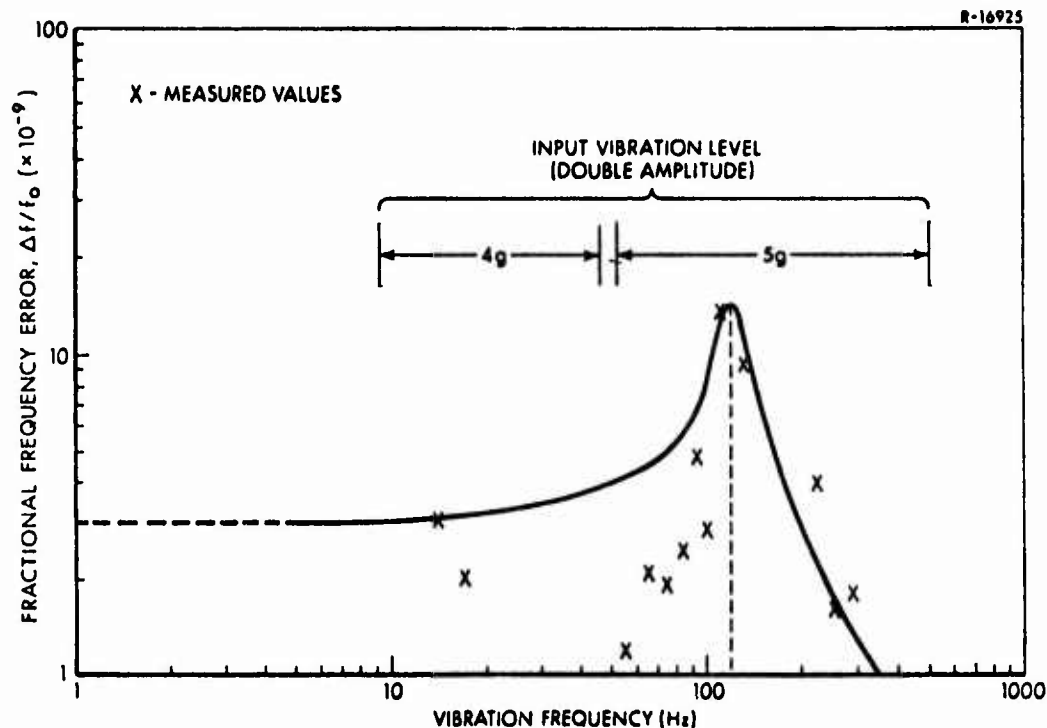
Figure 4.1-7   Frequency Error as a Function of
                Vibration Frequency

assuming a wide band noise input. The wide band noise can
be represented as a first-order Markov process with a cor-
relation time, τ_m, of 3.2 x 10^{-4} seconds. The power spec-
trum of this process is essentially flat out to a frequency
of 500 Hz. This wide band noise is undistinguishable from
white noise up to a vibration frequency of 300 Hz which is
beyond the region of crystal response shown in Fig. 4.1-7.
A worst case value (cf, MIL-STD-810B, Curve AE) for the rms
level of the input noise is σ_m = 5.4g. The wide band noise
can be simplified to an equivalent white noise (as shown in
Ref. 8) with a spectral level

$$q_v = 2\tau_m \; \sigma_m^2 = 0.02 \; g^2 \; \text{sec} \qquad (4.1-2)$$

The model representing the frequency error due to
vibration, δf_v, is shown in Fig. 4.1-8. The input is the

73
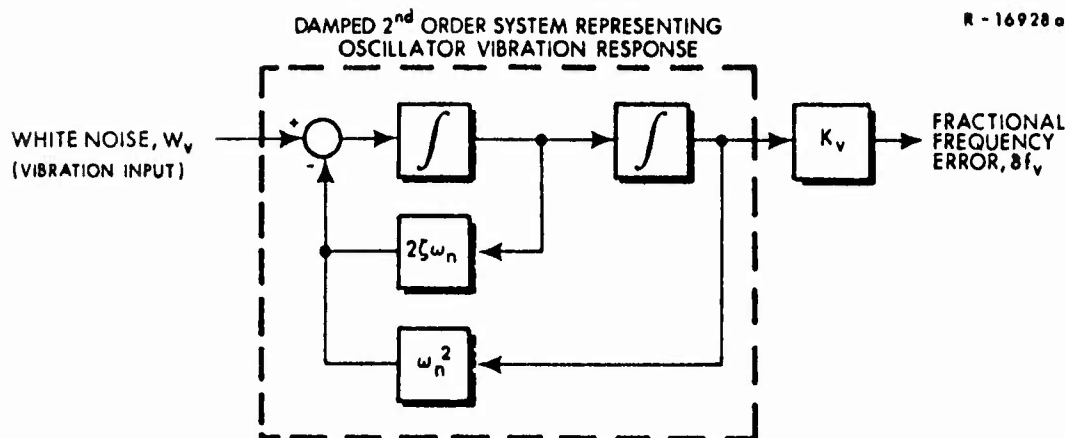
Figure 4.1-8   Crystal Oscillator Vibration Error Model

white noise equivalent to the assumed wide band noise and
the second-order system represents the response of the oscil-
lator as shown in Fig. 4.1-7.   The resonant curve in the
figure corresponds to a natural frequency, ω_n, of 754 rad/sec
and a damping ratio, $\zeta = 0.1$.   The constant K_v is the lateral
vibration drift coefficient with a value of 6×10^{-10}/g from
Fig. 4.1-7.   As expected, the vibration coefficient K_v is
very close to the g-sensitive drift coefficient K_g.

        Shock — When a quartz crystal oscillator is sub-
jected to a shock, a permanent frequency offset results.
No specific values are available (at this time) for the
magnitude of this offset during the shock, but step frac-
tional frequency shifts on the order of 1×10^{-9} have been
observed (Ref. 7) following shocks of 15g, 45g, and 60g.
A reasonable model for the effect of a shock of short dura-
tion (~ 1 msec), occurring at time t_s, is a step fractional
frequency shift ($\delta f_s \big|_{t_s}$) of 1×10^{-9}.

4.1.3 Composite Quartz Oscillator Error Model

        In the previous section, models were developed to
describe the frequency errors which arise from perturbations

74

in the oscillator's environment. The total fractional fre-
quency error due to environmental effects, δf_{env}, is the sum
of the individual errors resulting from temperature changes,
oscillator warm-up, acceleration, shock and vibration ef-
fects, viz,

$$\delta f_{env} = \delta f_t + \delta f_w + \delta f_a + \delta f_s\big|_{t_s} + \delta f_v \qquad (4.1\text{-}3)$$

The environmental effects model can be combined with
the intrinsic stability model of the quartz oscillator (see
Appendix C) as shown in Fig. 4.1-1. The state vector for
the composite quartz crystal oscillator error model is given
in Table 4.1-1. Two error sources are not included explicitly
in the state vector. The error arising from the acceleration
of the oscillator (i.e., $\delta f_a = K_g|\underline{a}|$) is more appropriately
modeled as an additive quantity. The second error source

TABLE 4.1-1

QUARTZ CRYSTAL OSCILLATOR
ERROR MODEL STATE VECTOR

STATE	SYMBOL	DESCRIPTION
1	$\delta\phi$	Phase Error
2	δf	Frequency Error
3	$\delta\dot{f}$	Frequency Rate Error
4	x_{1f}	Flicker Noise
5	x_{2f}	Intermediate Flicker Noise State
6	δf_t	Frequency Error (Thermal Model)
7	x_t	Temperature Variation
8	δf_w	Frequency Error (Warm-up Model)
9	δf_v	Frequency Error (Vibration Model)
10	x_v	Intermediate Vibration Error State

which will remain unmodeled is the effect of an impulsive shock to the oscillator. In any practical implementation of a Kalman filter, a priori knowledge of the time of occurrence of a shock is unlikely and such behavior cannot be described by a Gauss-Markov random process model. However, the effect of such an unanticipated shock can, and will, be examined in this study.

The error model can be written in state variable form as

$$\dot{\underline{x}}(t) = F \, \underline{x}(t) + G \, \underline{w}(t) \qquad (4.1\text{-}4)$$

where

$$\underline{x}(t) \;=\; 10 \times 1 \text{ column vector of the error states in Table 4.1-1}$$
$$F \;=\; 10 \times 10 \text{ error dynamics matrix}$$
$$\underline{w}(t) \;=\; 10 \times 1 \text{ column vector of process noise}$$
$$G \;=\; 10 \times 10 \text{ process noise distribution matrix}$$

The dynamics matrix,

$$F = \begin{bmatrix}
0 & 1 & 0 & f_1 & 0 & 1 & 0 & 1 & 1 & 0 \\
0 & 0 & 1 & 0 & 0 & 0 & 0 & 0 & 0 & 0 \\
0 & 0 & 0 & 0 & 0 & 0 & 0 & 0 & 0 & 0 \\
0 & 0 & 0 & f_2 & 1 & 0 & 0 & 0 & 0 & 0 \\
0 & 0 & 0 & f_3 & 0 & 0 & 0 & 0 & 0 & 0 \\
0 & 0 & 0 & 0 & 0 & -1/\tau_{tv} & K_{tv}/\tau_{tv} & 0 & 0 & 0 \\
0 & 0 & 0 & 0 & 0 & 0 & -1/\tau_a & 0 & 0 & 0 \\
0 & 0 & 0 & 0 & 0 & 0 & 0 & -1/\tau_w & 0 & 0 \\
0 & 0 & 0 & 0 & 0 & 0 & 0 & 0 & 0 & 1 \\
0 & 0 & 0 & 0 & 0 & 0 & 0 & 0 & -\omega_n^2 & -2\zeta\omega_n
\end{bmatrix}$$

$$(4.1\text{-}5)$$

76

is based upon the prototype model shown in Fig. 4.1-1, the environmental models developed above and the model of intrinsic stability developed in Section C.3. Values of f_1, f_2 and f_3 are defined in Eq. (C.3-7). The noise distribution matrix, also based on Section C.3, is

$$
G = \begin{bmatrix}
g_1 & & & & & & \\
0 & & 0 & & & & O \\
0 & & & 0 & & & \\
& & & & 0 & & \\
g_2 & & & & & 0 & \\
g_3 & & & & & & 0 \\
\text{--} & \text{--} & O & & & & 1 \\
& & & & & & 0 \\
0 & & & & & & 0 \\
& & & & & & K_v
\end{bmatrix} \tag{4.1-6}
$$

where g_1, g_2 and g_3 are defined in Eq. (C.3-8). The continuous process noise matrix, Q_c, is defined by

$$
E\left[\underline{w}(t)\ \underline{w}^T(\zeta)\right] \equiv Q_c\ \delta(t-\zeta) \tag{4.1-7}
$$

where $\delta(t-\zeta)$ is the Dirac delta function. Table 4.1-2 lists the non-zero elements of Q_c.

TABLE 4.1-2

CONTINUOUS PROCESS NOISE MATRIX
(NON-ZERO ELEMENTS)

ELEMENT	SOURCE	SYMBOL	VALUE
(1,1)	Flicker Noise	q_f	1.14×10^{-19}
(7,7)	Temperature Variation	q_a	$3.0 \times 10^{-3}\ {}^{\circ}C^2/\text{sec}$
(10,10)	Vibration	q_v	$2.0 \times 10^{-2}\ g^2\ \text{sec}$

4.2 USER PERFORMANCE PROJECTIONS

4.2.1 Evaluation Scenario

The analysis of the airborne user performance employed the GPS Direct Simulation Program (DSIM, see Ref. 2) in order to investigate the effects of environmentally-induced errors. The airborne user trajectory is illustrated in Fig. 4.2-1. The user initially processes one minute of GPS measurements while stationary to calibrate the receiver clock. After takeoff, the helicopter makes turns at a maximum of 15 deg/sec, accelerates at a maximum of 2.5 mps/sec and changes altitude at a maximum of 3.0 mps.
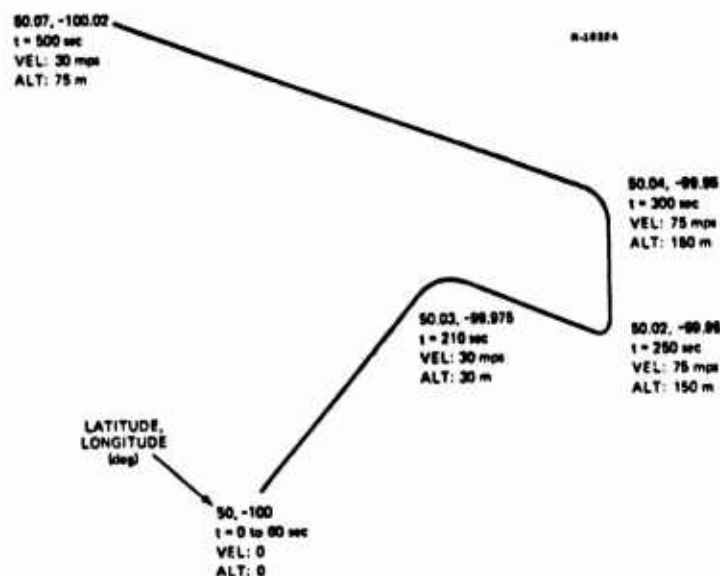
Figure 4.2-1   Airborne User Trajectory

Preliminary investigation indicated that a GPS/inertial configuration would be more sensitive to receiver clock errors than other mechanizations such as GPS/air data or GPS alone. Thus, in order to evaluate a worst case situation, an inertial navigation system (INS) has been adopted for this study. Although a GPS/INS system may not be of primary Army interest at this time, the findings relative to clock modeling are generally applicable to all GPS mechanizations. A barometric altimeter is also

included to bound the vertical channel of the INS. The measured altitude is used, in a closed-loop fashion, to damp the altitude errors. A detailed error model for the INS is presented in Section 4.2.2.

A detailed discussion of the GPS Phase III configuration used in this study is presented in Appendix B. For the airborne user performance analyses considered in this chapter, pseudo-range and pseudo-range-rate measurements are obtained simultaneously from four of the satellites in view (numbers 1, 2, 3 and 5) every 10 seconds. Initial state errors, initial filter standard deviation values and process noise variances for this study are given in Section 4.2.2.

4.2.2 Error Models

Two error models are required for the generation of user performance projections. The first is a model describing the "real world" errors. This model would ideally be a complete description of all significant error sources which impact upon user navigation performance. The second model, which is a deliberately simplified description of the "real world" errors, is implemented in the user Kalman filter.

"Real World" Error Model — The "real world" error model includes a description of GPS system errors, the user INS errors and a user clock error model. The GPS system errors, as implemented in the DSIM program, include satellite clock and ephemeris errors, signal propagation delays (ionospheric, tropospheric and multipath), and receiver noise and quantization. These error sources and their models are well documented in Ref. 2 and will not be repeated here. The equations describing inertial system error propagation are

79

explicitly stated in the discussion of the user filter later in this section. The barometric altimeter is used to sense the altitude of the user above the earth. The error in measuring the altitude is modeled as a scale factor error (first-order Markov process) plus a white measurement noise (Ref. 2). Figure 4.2-2 is a block diagram of the barometric altimeter error model. The altitude error is computed as

$$\delta h_m = h_u \, \delta s_a + v_a \qquad (4.2\text{-}1)$$

where

δh_m = altitude error

h_u = true user altitude

δs_a = barometric altimeter scale factor error

v_a = measurement noise associated with the altitude measurement; $E[v_a(t_n)] = 0$

$E[v_a(t_n) \, v_a(t_m)] = \sigma_a^2 \, \delta_{mn};$ δ_{mn} is the the Kronecker delta function, i.e.,

$$\delta_{mn} = \begin{cases} 1 & m = n \\ 0 & m \neq n \end{cases}$$

R-15320
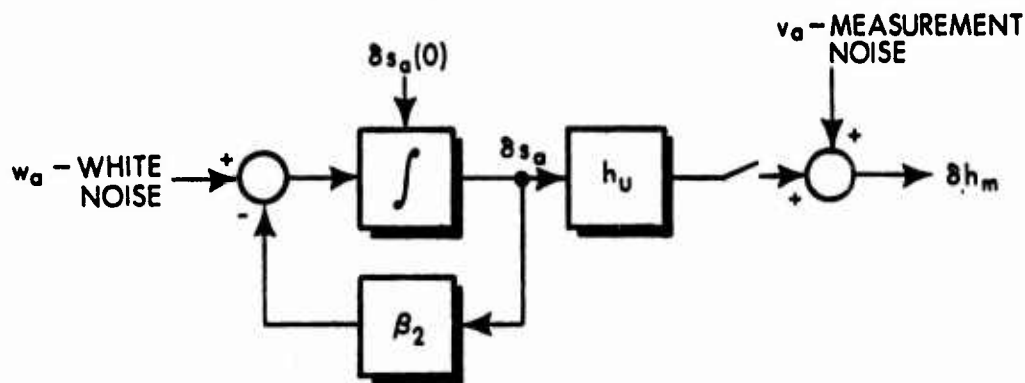
Figure 4.2-2   Barometric Altimeter Error Model

80

The user clock error model was developed in Section 4.1. The 10-state clock error model includes a description of the effects of temperature, warm-up and vibration. Errors which arise from acceleration and shock are not explicitly included in the error state vector (see Table 4.1-1). However, these two error sources are included in the description of the "real world" and their effects on user navigation performance will be evaluated.

User Filter — The user Kalman filter estimates the 20 user navigation and clock errors summarized in Table 4.2-1. The user position and velocity errors are referenced to a locally level [north (n), east (e) and down (d)] coordinate system located at the instantaneous user position. As indicated in Table 4.2-1, INS errors are characterized by gyro drift (with bias and random walk components) and accelerometer bias error terms. This model will provide a reasonable description of INS errors during the short ($\approx$8 minute) mission under consideration. Since the purpose of this study is to evaluate the effect of user clock errors, a more detailed INS error model would be undesirable. The user filter does not include a model of any environmentally-induced errors in the user clock. The state modeling the effects of aging has also been deleted in the filter model, since the total mission duration is shorter than the time required for the effects of aging to become significant.

The user filter error model can be written in state variable form

$$\underline{\dot{x}}_u(t) = F_u(t) \, \underline{x}_u(t) + G_u \, \underline{w}_u(t) \qquad (4.2-2)$$

where

$\underline{x}_u(t)$ = 20 x 1 column vector of user error states

81

TABLE 4.2-1

STATE DESCRIPTIONS FOR 20-STATE AIRBORNE USER FILTER

STATE NUMBER	SYMBOL	DESCRIPTION
1	δR_n	North Position Error
2	δR_e	East Position Error
3	δh	Altitude Error
4	δV_n	North Velocity Error
5	δV_e	East Velocity error
6	δV_d	Down Velocity Error
7	ψ_n	Platform Misalignment About North
8	ψ_e	Platform Misalignment About East
9	ψ_d	Platform Misalignment About Down
10	δs_a	Barometric Altimeter Error
11	ε_n	North Gyro Drift
12	ε_e	East Gyro Drift
13	ε_d	Down Gyro Drift
14	μ_n	North Accelerometer Bias Error
15	μ_e	East Accelerometer Bias Error
16	μ_d	Down Accelerometer Bias Error
17	$\delta\phi$	Phase Error
18	δf	Fractional Frequency Error
19	x_{1f}	Flicker Noise
20	x_{2f}	Intermediate Flicker Noise State

$$F_u(t) = \text{20 x 20 user error dynamics matrix}$$

$\underline{w}_u(t)$ = 20 x 1 column vector of white process noise such that $E\left[\underline{w}_u(t)\right] = 0$, $\text{Cov}\left[\underline{w}_u(t)\right] = E\left[\underline{w}_u(t) \; \underline{w}_u(\zeta)^T\right]$ = $Q_u(t) \; \delta(t-\zeta)$; $\delta(t-\zeta)$ is the Dirac delta function.

G_u = 20 x 20 process noise distribution matrix

The dynamics matrix, F_u, may be partitioned as

$$F_u(t) = \begin{bmatrix} F_s(t) & \vline & 0 \\ \hline 0 & \vline & F_c \end{bmatrix} \tag{4.2-3}$$

where

$F_s(t)$ = 16 x 16 inertial navigation system error dynamics matrix. (This description of INS errors is also included in the "real world" error model.)

F_c = 4 x 4 clock error dynamics matrix

The $F_s(t)$ matrix (as developed in Refs. 2 and 8) is shown in Fig. 4.2-3 with

V_n, V_e = the user's north and east velocities in the local level navigation frame

$\underline{R}$ = position vector of the user measured from the center of the earth

r = $|\underline{R}|$

L = user latitude

Ω = earth's angular rate

D_1, D_2 = vertical channel damping coefficients (0.0011 sec^{-2} and 0.0666 sec^{-1} respectively)

Figure 4.2-3 The System Dynamics Matrix, $F_S(t)$

THIS REPORT HAS BEEN DELIMITED
AND CLEARED FOR PUBLIC RELEASE
UNDER DOD DIRECTIVE 5200.20 AND
NO RESTRICTIONS ARE IMPOSED UPON
ITS USE AND DISCLOSURE.

DISTRIBUTION STATEMENT A

APPROVED FOR PUBLIC RELEASE;
DISTRIBUTION UNLIMITED.

$$\beta_2 \quad = \quad \text{altimeter inverse time constant}$$

$$g_o \quad = \quad \text{nominal acceleration due to gravity}$$

$$f_n, f_e, f_d \quad = \quad \text{specific force; equal to } a_n, a_e, a_d - g_o, \text{ respectively}$$

The clock error dynamics matrix, from Eq. (4.1-5), is

$$F_c = \begin{bmatrix} 0 & 1 & 1.0 \times 10^{-2} & 0 \\ 0 & 0 & 0 & 0 \\ 0 & 0 & -1.01 \times 10^{-1} & 1 \\ 0 & 0 & -1.0 \times 10^{-4} & 0 \end{bmatrix} \qquad (4.2\text{-}4)$$

The noise distribution matrix may also be partitioned such that

$$G_u = \begin{bmatrix} I_{16\times16} & 0 \\ \hline 0 & g_c & 0 \end{bmatrix} \qquad (4.2\text{-}5)$$

where $I_{16\times16}$ denotes a 16x16 identity matrix and, from Eq. (4.1-6),

$$g_c = \begin{bmatrix} 1.0 \times 10^{-2} \\ 0 \\ 9.09 \times 10^{-1} \\ 9.90 \times 10^{-3} \end{bmatrix} \qquad (4.2\text{-}6)$$

The user filter initial conditions are summarized in Table 4.2-2. The data contained in the table includes

85

TABLE 4.2-2

AIRBORNE USER STATE AND FILTER ERROR VALUES

STATE NUMBER	SYMBOL	DESCRIPTION	INITIAL ESTIMATION ERROR VALUE	UNITS	INITIAL FILTER STANDARD DEVIATION VALUE	UNITS	PROCESS NOISE SPECTRAL DENSITY VALUE	UNITS
1	δR_n	North Position Error	-75	m	100	m	0	-
2	δR_e	East Position Error	-75	m	100	m	0	-
3	δh	Altitude Error	30	m	30	m	0	-
4	δV_n	North Velocity Error	0	mps	0.3	mps	0	-
5	δV_e	East Velocity Error	0	mps	0.3	mps	0	-
6	δV_d	Down Velocity Error	0	mps	0.3	mps	0	-
7	ψ_n	Platform Misalignment About North	50	sec	72	sec	0	-
8	ψ_e	Platform Misalignment About East	-20	sec	72	sec	0	-
9	ψ_d	Platform Misalignment About Down	400	sec	530	sec	0	-
10	δs_a	Barometric Altimeter Error*	0.03	-	0.04	-	8.8×10^{-7}	sec^{-1}
11	ϵ_n	North Gyro Drift	0.03	deg/hr	0.03	deg/hr	1.2×10^{-3}	$(deg/hr)^2/hr$
12	ϵ_e	East Gyro Drift	-0.02	deg/hr	0.03	deg/hr	1.2×10^{-3}	$(deg/hr)^2/hr$
13	ϵ_d	Down Gyro Drift	-0.01	deg/hr	0.03	deg/hr	1.2×10^{-3}	$(deg/hr)^2/hr$
14	μ_n	North Accelerometer Bias Error	-200	μg	316	μg	0	-
15	μ_e	East Accelerometer Bias Error	-100	μg	316	μg	0	-
16	μ_d	Down Accelerometer Bias Error	75	μg	316	μg	0	-
17	$\delta\phi$	Phase Error	22.5	m	30	m	1.03×10^{-2}	$(mps)^2$
18	δf	Frequency Error	0.3	mps	0.3	mps	0	-
19	x_{1f}	Flicker Noise	0.12	mps	0.12	mps	0	-
20	x_{2f}	Intermediate Flicker Noise State	1.4×10^{-3}	m/sec^2	1.4×10^{-3}	m/sec^2	0	-

*Markov process, time constant = 3600 sec.

the initial filter state estimation errors, the initial filter estimation error standard deviations, and values assumed for the filter noise spectral densities. The user filter's initial covariance matrix, $P_u(0)$, is assumed to be diagonal with the exception of the correlation between platform level alignment (ψ_n, ψ_e) and accelerometer bias errors (μ_e, μ_n) and between azimuth alignment (ψ_z) and east gyro drift (ϵ_e). The level alignment/accelerometer bias correlation was selected as 0.95 and the azimuth alignment and east gyro drift were assumed to be perfectly correlated. This represents, in a simplified manner, the result of pre-flight gyrocompass alignment. The diagonal elements of the filter covariance matrix, P_u, are set equal to the squares of the initial filter standard deviations. The continuous spectral density matrix, Q_u, is assumed to be a diagonal matrix with the diagonal equal to the spectral densities given in the table. The noise distribution matrix is given by Eqs. (4.2-5) and (4.2-6).

The clock error states (phase, frequency, etc.) in the table are expressed with the same dimensions as position and velocity errors (i.e., m and mps). The conversion from the units of Section 4.1 to those considered here is accomplished by multiplying the appropriate clock states in the $P_u(0)$ and Q_u matrices by the square of the velocity of propagation of the radio signal from the satellite to the user. This study will consider the signal propagation velocity to be constant with a value equal to the speed of light, $c = 3 \times 10^8$ mps. The F_u and G_u matrices remain unchanged.

The user filter formulation assumes that the user is equipped with a multichannel X-model receiver to allow the simultaneous processing of pseudo-range and pseudo-range-rate information from four of the satellites in view. The filter-assumed receiver measurement noise levels are

87

7.5 m (rms) and 0.15 mps (rms) for pseudo-range and pseudo-range-rate, respectively. Errors due to the ionospheric and tropospheric effects are assumed (in the filter) to be compensated to within the measurement noise and are not correlated with the other error sources.

4.2.3 Results

This section will present user performance projections which predict the impact of environmentally-induced GPS receiver clock errors on user navigation performance. The results are given in the form of user estimation errors and the <u>rms estimation error envelope (standard deviation boundary) predicted by the user Kalman filter</u>. Each error source modeled in Section 4.1.2 is introduced into the "real world" model separately and its effect on user navigation performance is assessed by comparing the resultant navigation errors with those of a baseline run in which environmentally-induced errors were deleted. The following paragraphs discuss the impact of the various error sources.

<u>Baseline</u> — The baseline performance of the airborne user is indicative of the navigation errors which arise from GPS system errors (satellite ephemeris and clock errors, signal propagation errors, etc.) and user dependent errors (INS error sources and the non-environmentally-induced clock errors). This performance is illustrated in Fig. 4.2-4 for the trajectory of Fig. 4.2-1. The horizontal position error is under 8 m and the altitude error is below 1.5 m. The horizontal velocity error is less than 0.1 mps except during the first turn when it peaks to 0.26 mps. The peak is due to a residual heading error which couples the acceleration experienced during the turn into the horizontal velocity
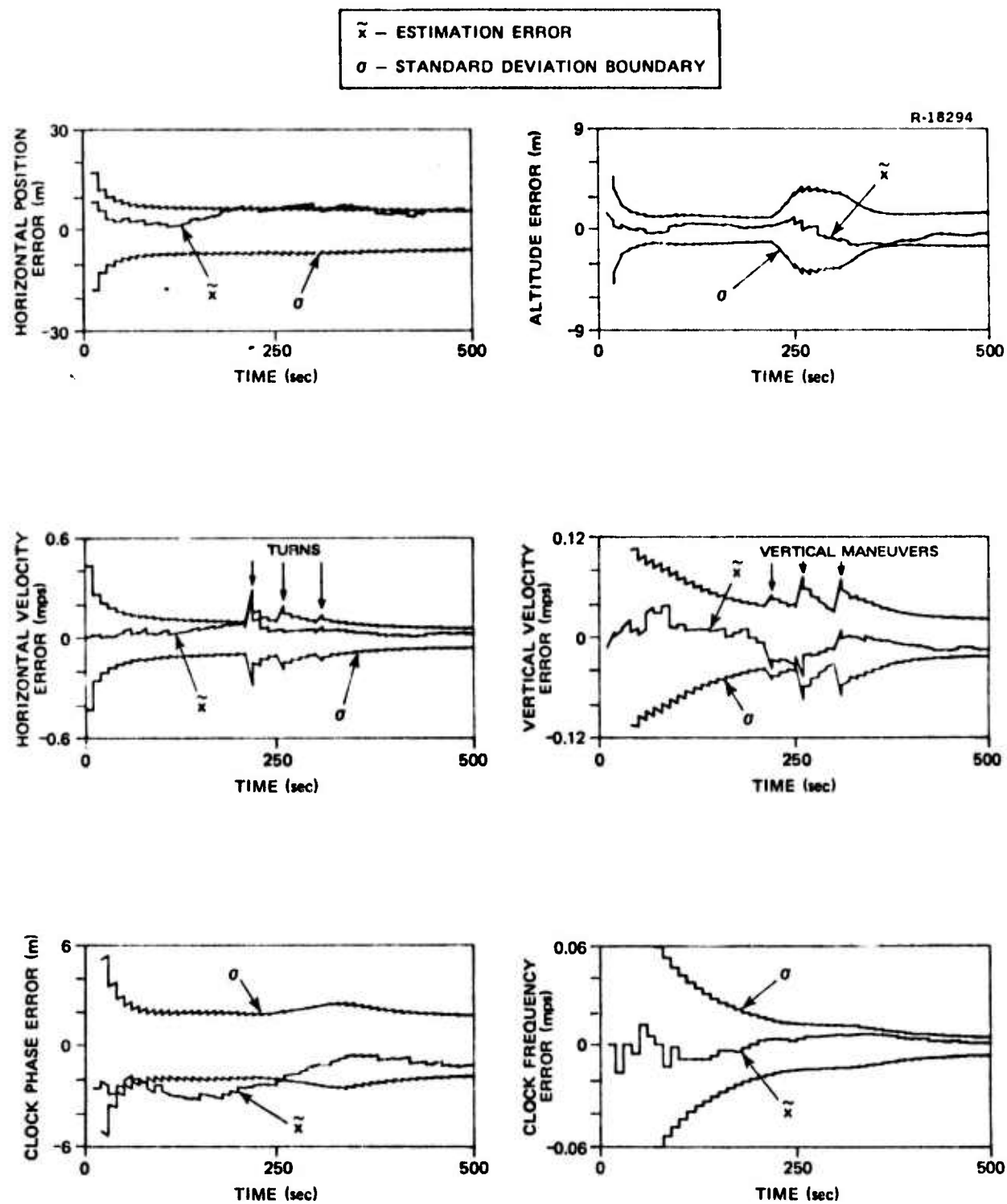
Figure 4.2-4   Airborne User Errors — Baseline

error. This makes the heading error highly observable, such that GPS pseudo-range-rate measurements during the first turn calibrate the heading error (see Fig. 4.2-5). The vertical velocity error remains below 0.05 mps. The user clock phase and frequency errors settle out to less than 1.25 m and 0.01 mps, respectively, after processing 250 seconds of pseudo-range and pseudo-range-rate measurements.

Degraded Quality — The "degraded quality" run considered the case in which the intrinsic stability of the real world oscillator was worse than that chosen as the filter design model. The degraded quality oscillator was obtained by increasing the process noise spectral level q_f [Eq. (C.3-9)] by a factor of ten. The performance projections for the degraded quality clock are shown in Fig. 4.2-6. The horizontal position, altitude, horizontal velocity and vertical velocity errors remain essentially unchanged from their baseline values. The user clock phase and frequency errors do change, however. Specifically, the clock phase error is outside the standard deviation boundary approximately 60% of the time. In addition, filter divergence (Ref. 5) occurs at 290 seconds for the clock frequency error state. This is indicative of the fact that the filter model is optimistic in
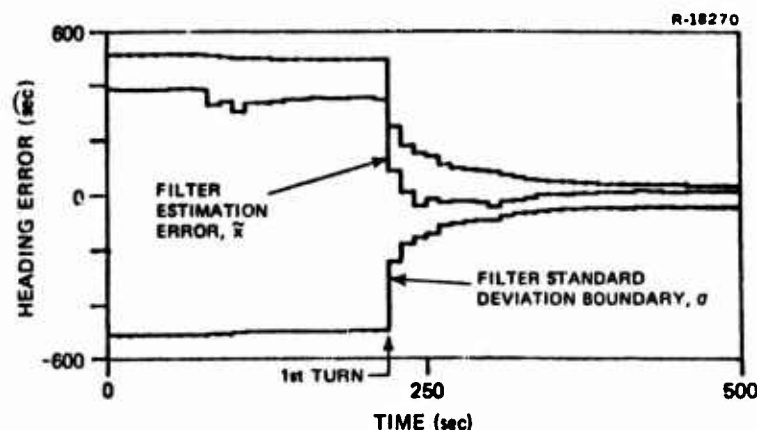
Figure 4.2-5   INS Heading Error During Flight
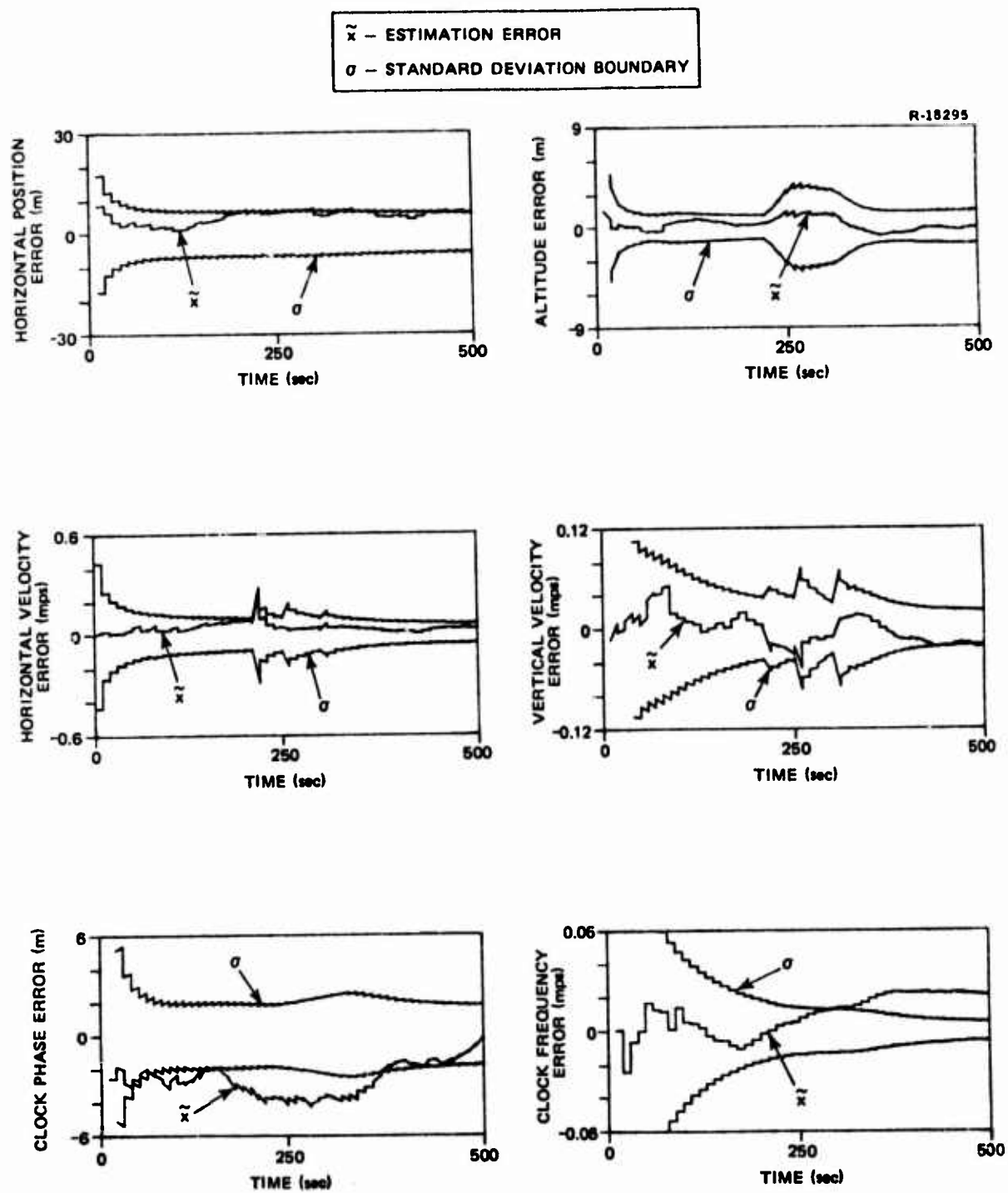
Figure 4.2-6   Airborne User Errors —
Degraded Quality

91

its description of the user clock error behavior. This situation can be remedied by increasing q_f in the filter model, but this will result in non-optimum performance if the real world clock performs in the manner described by the baseline model. This type of effect will be illustrated below when a worst case filter model is developed and evaluated.

Temperature — The effects of ambient temperature variations on user navigation performance are shown in Fig. 4.2-7. A comparison of these results with the baseline performance indicates that, for the assumed temperature fluctuations of the GPS receiver, the temperature sensitivity of the quartz crystal oscillator has minimum impact on user navigation. Thus, this error source need not be included in user Kalman filter design considerations.

Vibration — The effects of vibration of the receiver crystal oscillator on user navigation performance are shown in Fig. 4.2-8. A comparison of these results with the baseline performance indicates that, for the assumed level of random vibration of the crystal, the vibration sensitivity of the quartz crystal oscillator has minimum impact on user navigation. It should be noted, however, that a strong sinusoidal vibration near 120 Hz (see Fig. 4.1-7) would result in a large frequency error and could lead to a degradation in user navigation performance.

Warm-up — The impact of quartz crystal oscillator warm-up on user navigation performance is considered next. It was assumed that the oscillator had been turned-on 12 minutes prior to the start of the flight such that the
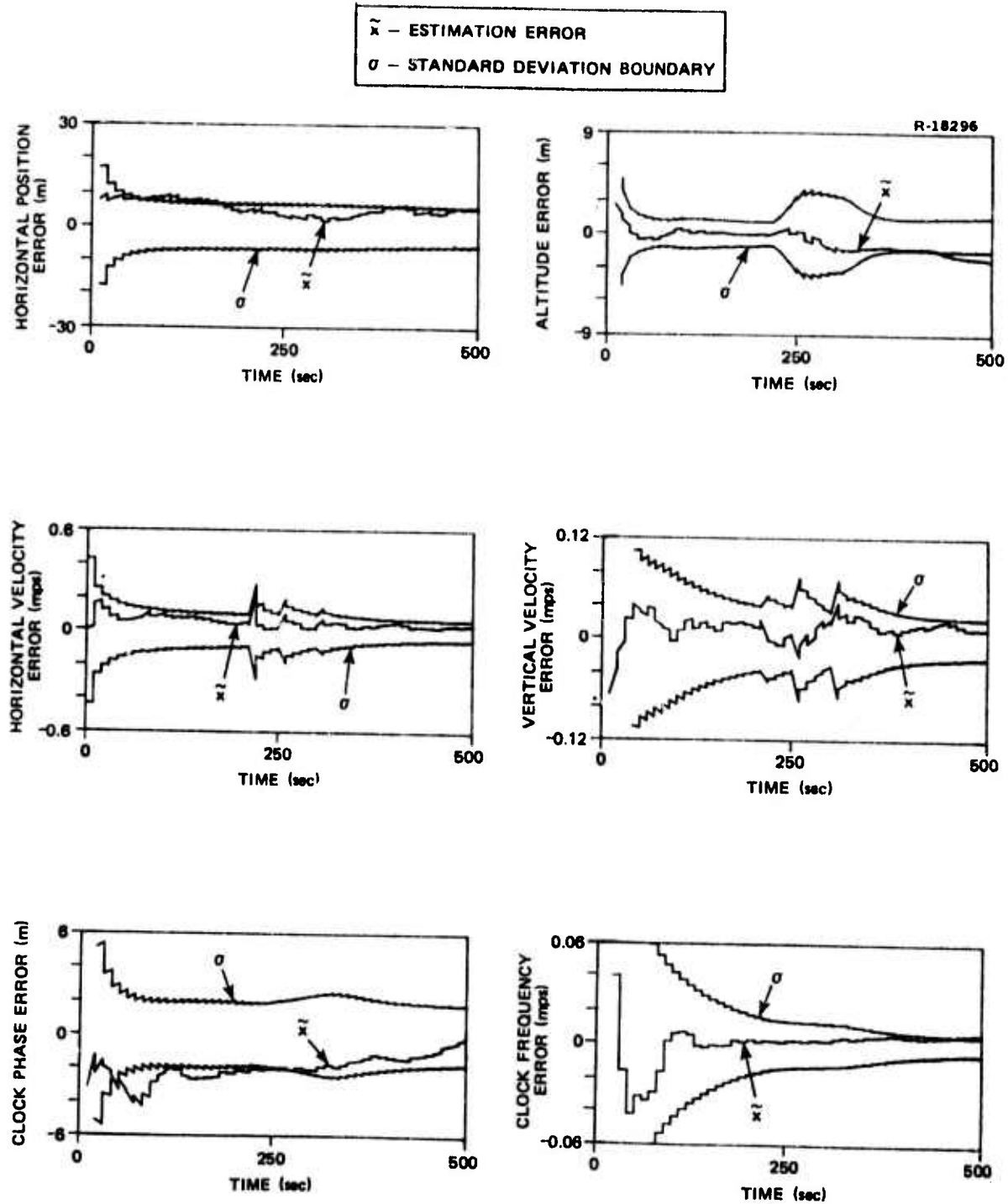
Figure 4.2-7   Airborne User Errors – Temperature
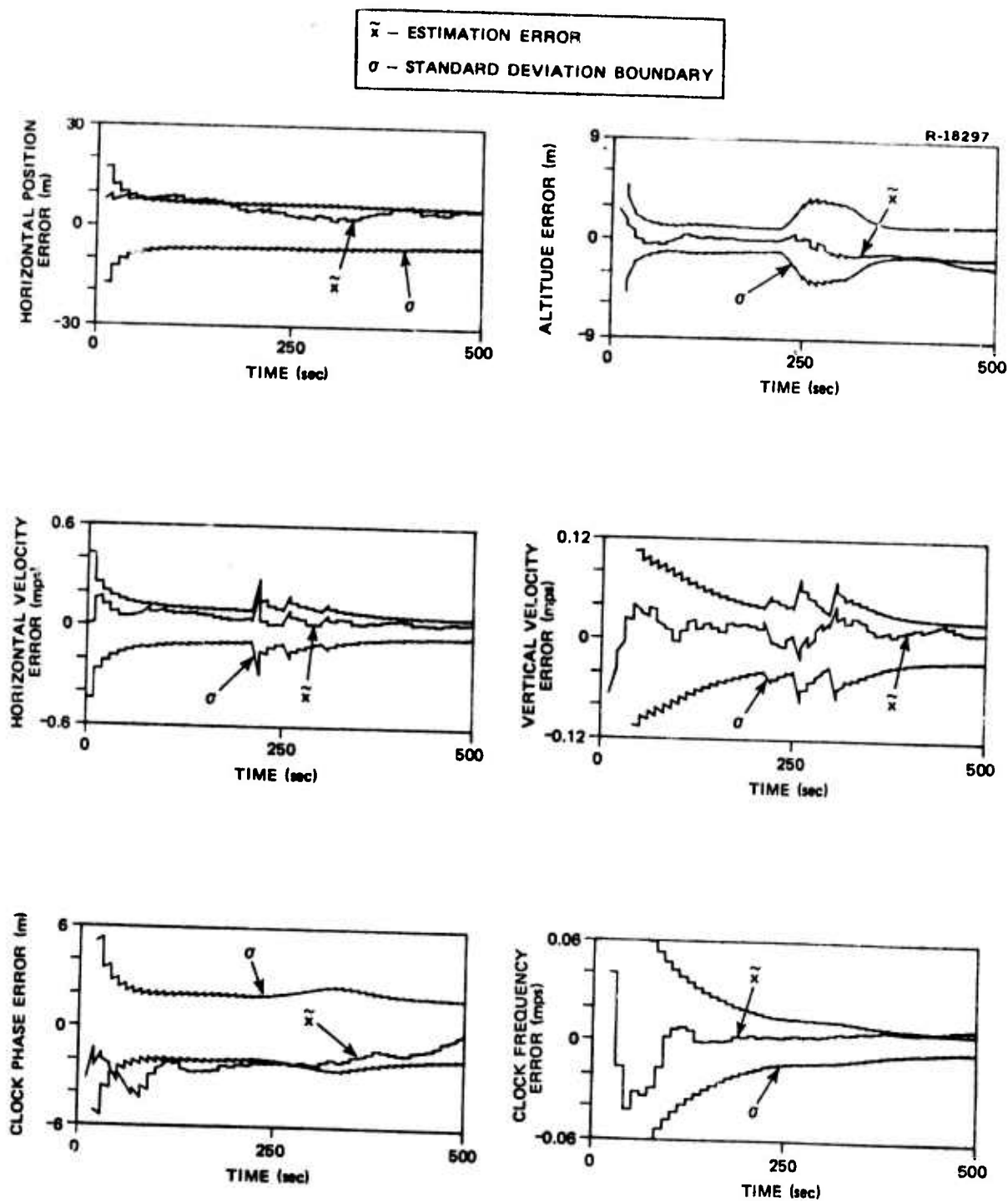
Figure 4.2-8   Airborne User Errors — Vibration

94

initial frequency offset (at t=0) was 3.0 mps (3.0 mps = $c \times \Delta f(12 \text{ min})/f_O$, where c is the speed of light and $\Delta f/f_O$ is obtained for oscillator "c" from Fig. 4.1-6). The 12 minute period from oscillator turn-on until the start of the flight was chosen to be compatible with a five minute coarse gyrocompass and 420 second fine-align of the INS.

Figure 4.2-9 illustrates the effects of oscillator warm-up when it is not modeled in the user filter. The frequency offset present during warm-up appears directly as the predominant contributor to frequency estimation error. This large frequency offset results in an increase in velocity error since the filter cannot properly allo-cate the large pseudo-range-rate measurement residual. The clock phase error also increases due to the warm-up induced frequency offset and consequently, user position errors are increased.

To compensate for the impact of oscillator warm-up, a model for the warm-up was included in the user filter. The model is identical to the warm-up model presented in Section 4.1.3. Figure 4.2-10 illustrates the resultant im-provement in user navigation performance. User position, horizontal velocity and clock phase errors are comparable to their baseline values. Vertical velocity and clock frequency errors exhibit a distinct improvement from their values in the unmodeled case, but they are somewhat larger than the baseline performance for the first 400 seconds of flight. Beyond this point, these errors compare favorably to their baseline values.

The use of warm-up initial conditions at 12 minutes after oscillator turn-on is arbitrary; however, it is con-sistent with the time frame imposed by the calibration

95
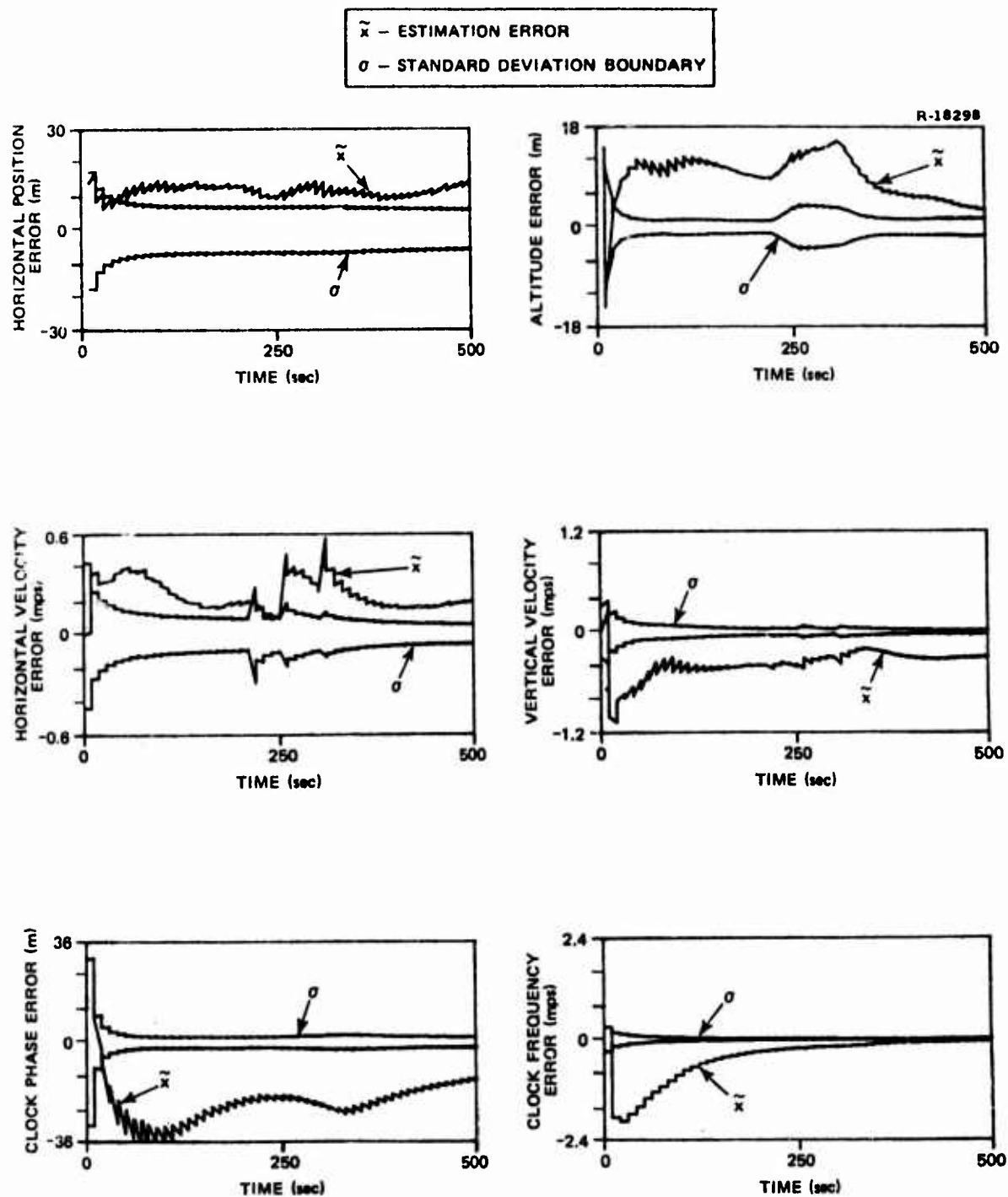
Figure 4.2-9   Airborne User Errors — Warm-up
(Not Modeled in User Filter)

96
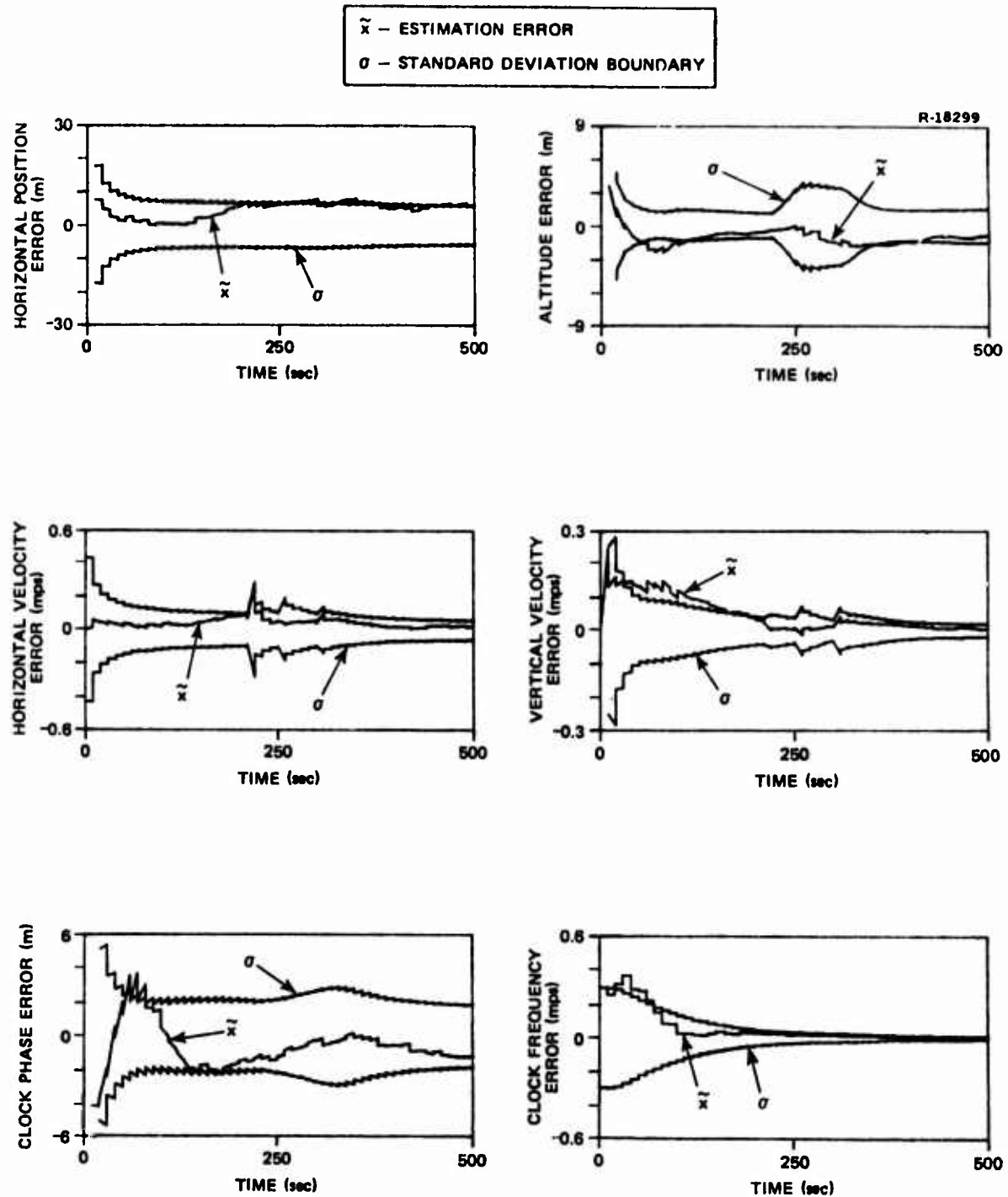
Figure 4.2-10   Airborne User Errors – Warm-up
(Modeled in User Filter)

97

of the INS. If the oscillator were turned-on at a point
in time closer to the start of the flight, the frequency
offset would be larger and consequently user navigation
performance would be degraded. Conversely, if a longer
warm-up period were allowed, user navigation errors would
tend to be closer to their baseline values.

Acceleration — The effects of acceleration of the
user clock on navigation performance are shown in Fig. 4.2-11.
The frequency error arising from the g-sensitivity of the
quartz oscillator is readily apparent as the airborne user
traverses the trajectory of Fig. 4.2-1. The impact of this
frequency error is manifest in the horizontal and vertical
velocity errors. When the user resumes straight and level
flight following the third turn, the frequency error is
reduced through processing of pseudo-range-rate measurements.
Since the filter model does not contain any information about
the acceleration sensitivity, the filter gains are small (at
this point) and do not weight the pseudo-range-rate measure-
ments heavily enough to remove the residual frequency error
entirely. One consequence of this residual frequency error
is the large residual velocity error which remains after
straight and level flight is resumed.

The clock phase error grows (to a maximum value of
200 m) as the user proceeds through the turns and begins
to recover during the straight and level portion of the
flight. However, since the filter gains are small (the
filter has no information about the large clock phase er-
ror), the phase error is not reduced rapidly. The large
horizontal velocity error ($\simeq 1$ mps) drives the horizontal
position error to 60 to 70 m. The altitude error (44 m at
t = 500 sec) results from the misallocation (by the filter)
of the large pseudo-range measurement residual which is
due to the clock phase error (these errors are highly cor-
related).

98
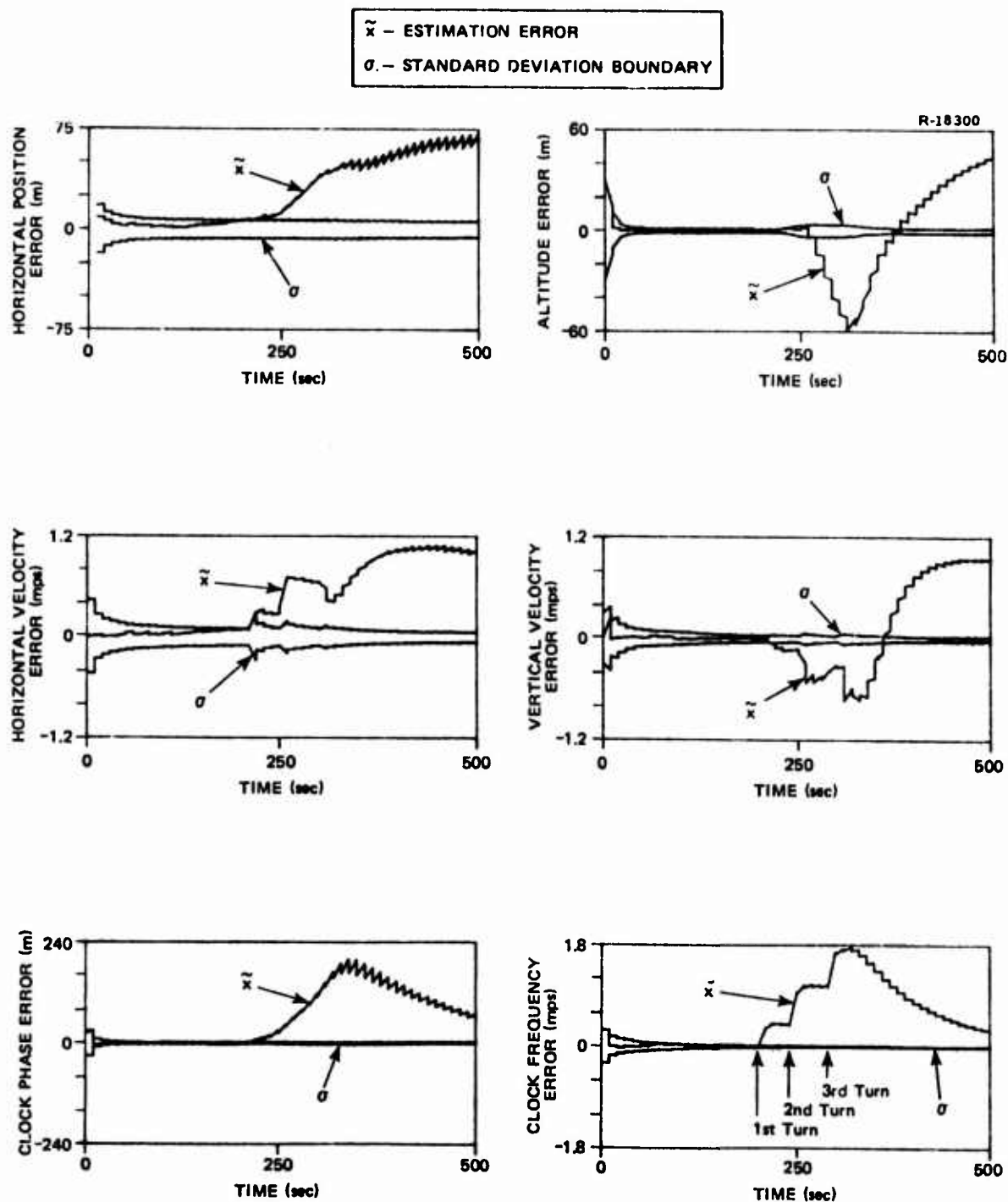
Figure 4.2-11   Airborne User Errors — Acceleration
(Not Modeled in User Filter)

99

This type of performance is clearly not desirable. One method which will afford a reduction in user navigation errors is to add white noise to the user filter to increase the clock frequency error variance. Adding a white noise with a spectral level of 1.83×10^{-3} $(mps)^2$/sec [discrete $q = 1.83 \times 10^{-2}$ $(mps)^2$], driving the frequency error state in the user filter, results in the performance shown in Fig. 4.2-12. The horizontal position and velocity errors are reduced to approximately their baseline values. The altitude and vertical velocity errors exhibit dramatic improvement, but remain larger than in the baseline case. (The altitude error remains well outside the standard deviation boundary from 280 seconds until the end of the flight.)

A significant reduction in user clock phase error is observed, with a peak excursion of 11 m evident during the third turn. The clock phase estimation error exceeds the filter standard deviation boundary, from the beginning of the second turn until the third turn is completed, as a result of the large spikes in the clock frequency error at 250, 260 and 300 seconds (viz., the beginning of the second and third turns). A somewhat weaker spike in the frequency error is evident at the beginning of the first turn (i.e., 210 seconds). These spikes are due to the unmodeled acceleration-dependent sensitivity of the quartz oscillator; however, since the frequency error state is being driven by white noise, the filter gains are large enough to effect a reduction in this frequency error at the next pseudo-range-rate measurement. Thus, the frequency error does not build-up as it did in the unmodeled case (see Fig. 4.2-11). This approach does have disadvantages in that the clock phase and frequency estimation errors are much "noisier" (i.e., exhibit larger rms errors) in the

Figure 4.2-12   Airborne User Errors — Acceleration
(Modeled in User Filter)

101

nonaccelerating portion of the flight than in either the
unmodeled or baseline cases.

The value selected for the spectral level of the
white noise was chosen to give acceptable performance and
should not be considered as optimal. Indeed, better user
performance may be obtained with careful "tuning" of the
filter which was not attempted in this study.

Shock — The effects on user navigation performance
of a shock to the receiver crystal oscillator are shown in
Fig. 4.2-13. The sharp jump in frequency error (0.3 mps =
c x 10^{-9}, where 1 x 10^{-9} is the fractional frequency offset
due to the shock at t = 350 sec) is quite evident as is the
rapid growth in clock phase error due to this frequency shift.
These errors are subsequently reduced through processing of
pseudo-range and pseudo-range-rate measurements; however, the
recovery is not rapid since the filter gains are small during
this latter portion of the flight, and the position and velo-
city errors appear after to diverge after t = 350 seconds.

Since this type of error cannot be described by a
Gauss-Markov random process model, the only method of im-
proving the filter's response to an unanticipated shock is
to increase the variance of the frequency error state (as
was done to handle the acceleration sensitivity of the
oscillator). Including a white noise [with spectral level
q = 5.625 x 10^{-4} (mps)^2/sec] driving the frequency error
state in the user filter results in the performance shown
in Fig. 4.2-14. The horizontal position and velocity er-
rors are reduced to approximately their baseline values.
The altitude and vertical velocity errors exhibit some
improvement over those in Fig. 4.2-13, but remain somewhat
larger than in the baseline case. (The altitude error
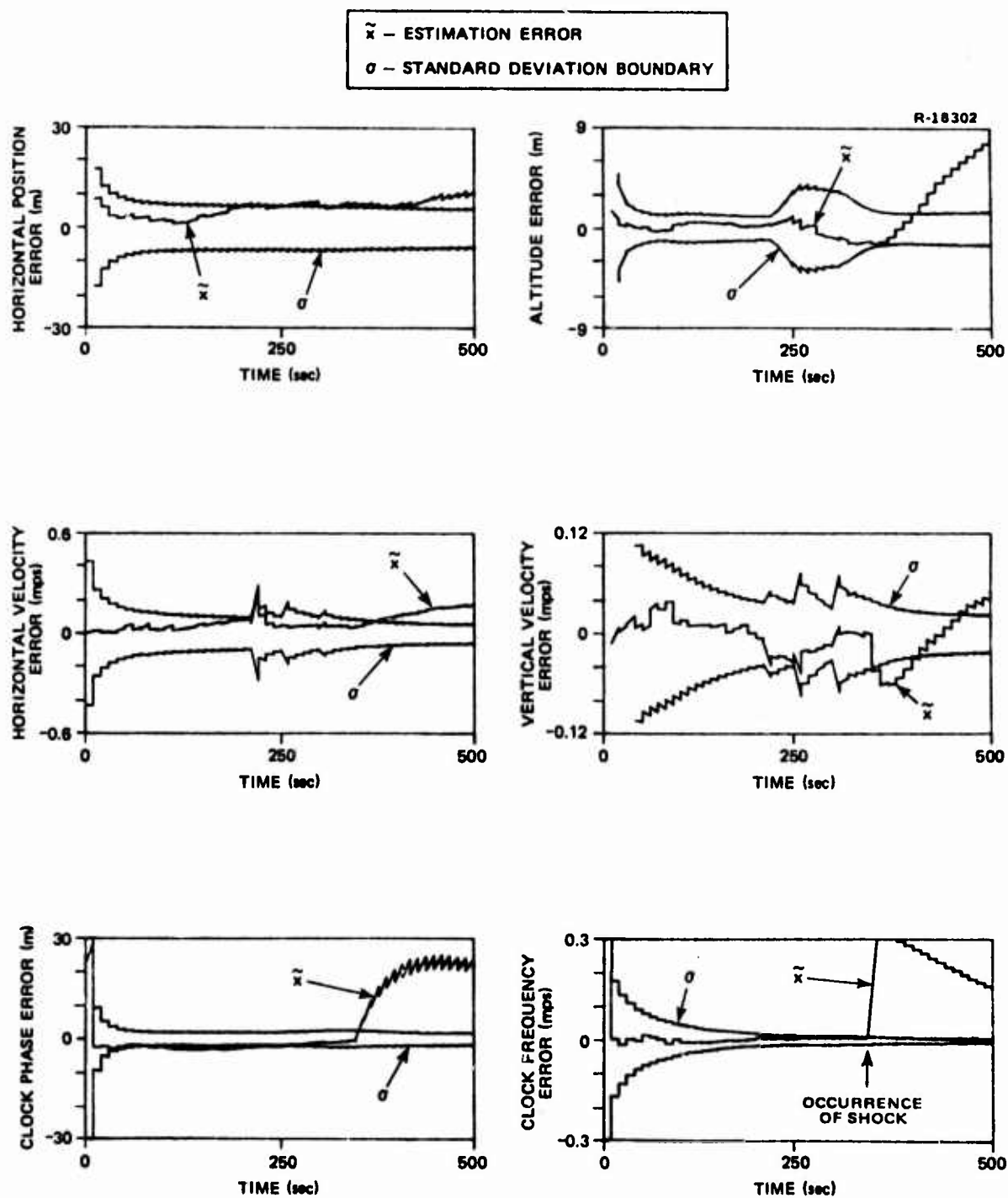
Figure 4.2-13   Airborne User Errors — Shock
(Not Modeled in User Filter)

103
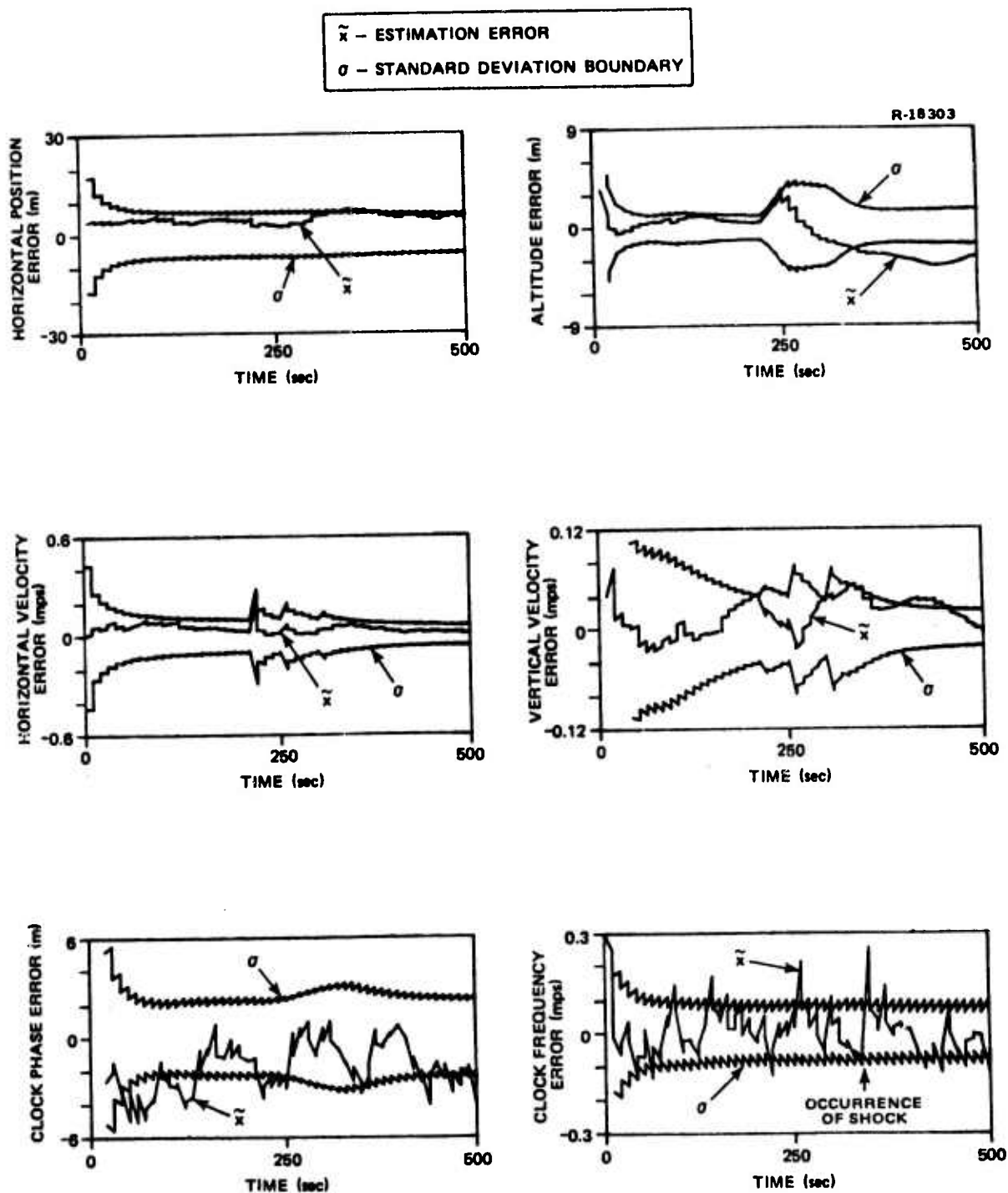
Figure 4.2-14   Airborne User Errors — Shock
(Modeled in User Filter)

remains well outside the standard deviation boundary from 350 seconds until the end of the flight.)

A significant reduction in user clock phase error is observed, with the estimation error well bounded by the filter standard deviation boundary. Similarly, the frequency estimation error is within the boundary at all but a few points. The shock has minimal effect on the frequency error since the larger filter gains (due to the increased frequency error variance) reduce the error significantly at the next pseudo-range-rate measurement. Here again, the disadvantages of this approach are evident as the clock phase and frequency estimation er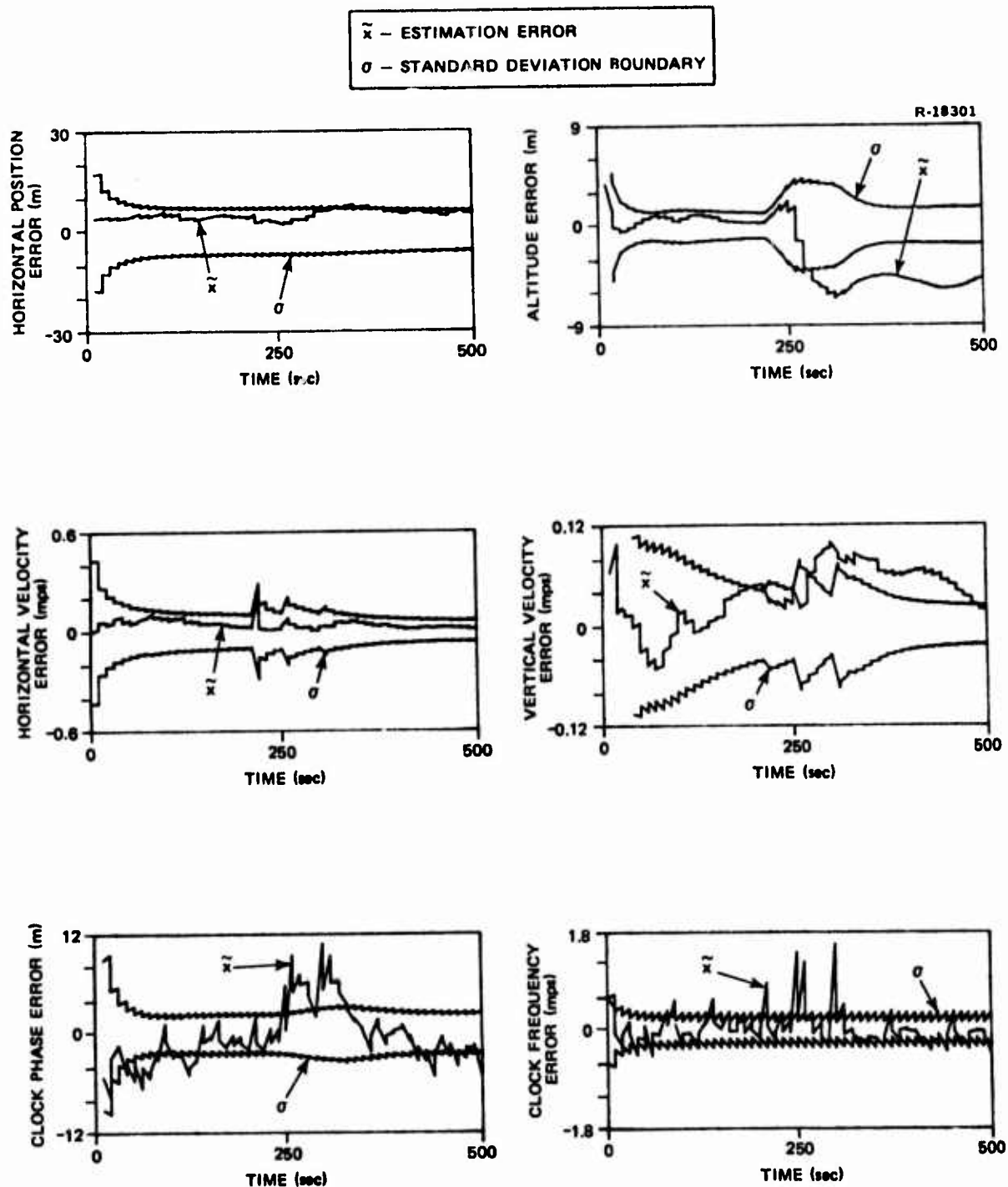rors are much "noisier" (i.e., exhibit larger rms values) throughout the flight than in either the unmodeled or baseline cases.

The value selected for the spectral level of the white noise was chosen to give acceptable performance and should not be considered as optimal. As with the previous cases, better user performance may be obtained with careful "tuning" of the filter which was not attempted in this study.

Modified User Filter — In light of the results obtained in the previous paragraphs, it is possible to reformulate the user Kalman filter such that it "acknowledges" the simultaneous presence of all the environmentally-induced error sources. In fact, this filter model has been developed in parallel with the evaluation of the environmental error sources. The error sources which lead to a serious degradation in user navigation performance (if they are not modeled in the user filter) are warm-up, acceleration and shock. In the discussion of warm-up, it was shown that inclusion of a model describing oscillator warm-up (decaying exponential)

in the user filter resulted in a substantial improvement in
user navigation performance. Similarly, in the discussions
of acceleration and shock effects, it was determined that
the addition of white noise driving the clock frequency er-
ror state in the user filter provided acceptable user per-
formance in the presence of acceleration and shock of the
receiver quartz oscillator.

Modifying the user filter to include the model of
oscillator warm-up [decaying exponential with initial vari-
ance of $(3.05 \text{ mps})^2$] and the additional white noise driving
the frequency error [spectral level, $q = 1.83 \times 10^{-3}$ $(\text{mps})^2/$
sec)], should provide adequate user navigation performance
under all environmental conditions. This performance is
indeed realized as shown in Fig. 4.2-15. For this run, all
of the environmental error sources discussed individually
in the preceding paragraphs were included in the "real
world" clock model. The horizontal position and velocity
errors are indistinguishable from their values in the base-
line run (in which it was assumed that no environmentally
induced errors existed). The increase in altitude error
during the second turn is a result of the unmodeled phase
error growth in the turn. Due to the high correlation be-
tween altitude and clock phase errors, the filter cannot
distinguish between the large phase error and the altitude
error, thus causing an increase in the altitude error at
the pseudo-range update. Following the turn, the altitude
error settles out at 4 to 5 m. A similar situation arises
between vertical velocity and clock frequency errors. The
vertical velocity error increases at the pseudo-range-rate
measurement as a result of the jumps in frequency error but
is reduced to about 0.05 mps during straight and level flight.
The altitude and vertical velocity errors are much smaller
with the modified filter than they would be with the original
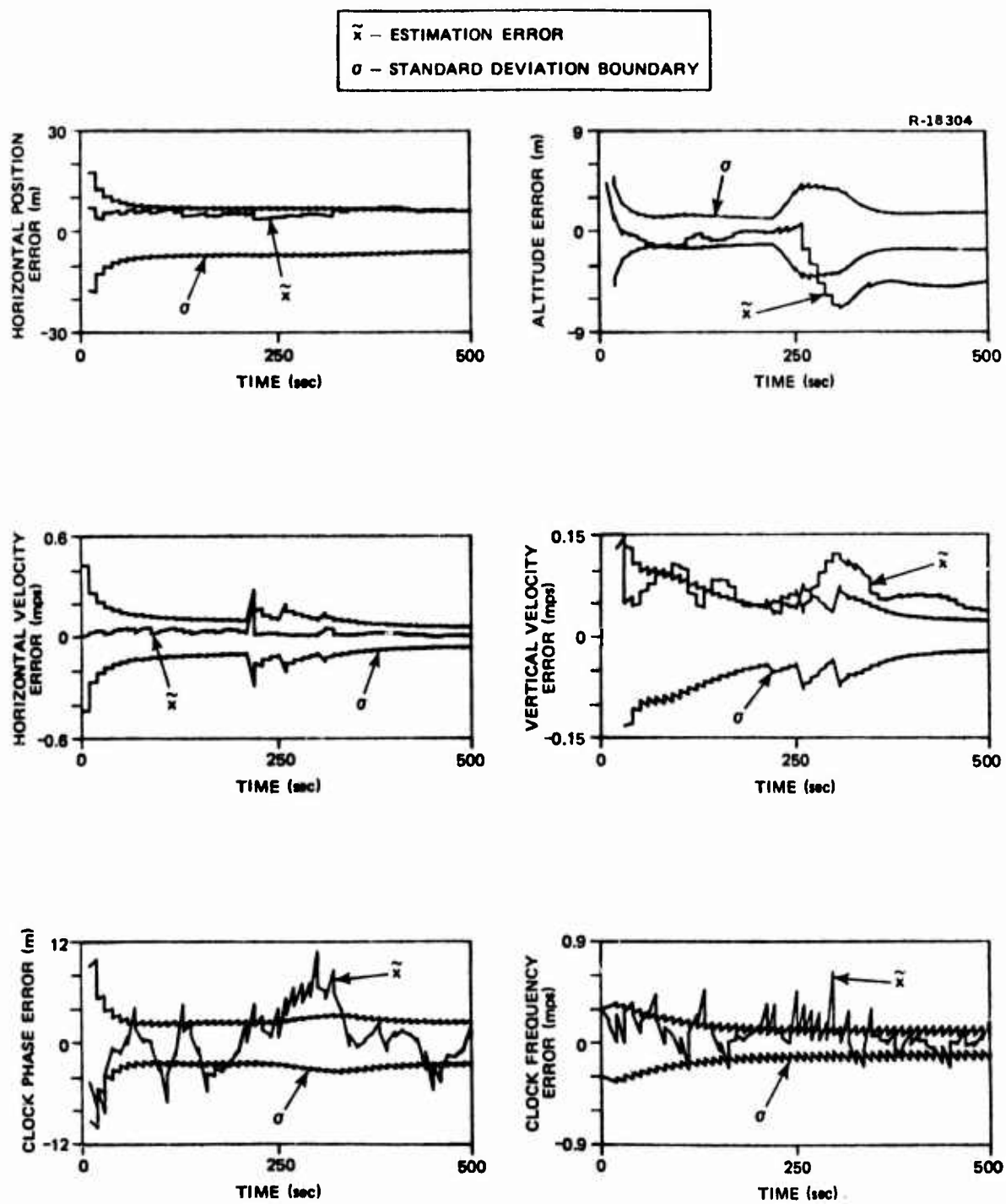
Figure 4.2-15   Airborne User Errors – Modified User Filter
(All Environmental Error Sources Present)

filter (compare with the errors resulting from acceleration of the oscillator prior to the filter modification, shown in Fig. 4.2-11). Although filter design is not the objective of this study, it should be possible to further reduce these errors by including process noise driving the altitude and vertical velocity states in the filter. This alternative was not pursued here.

The user clock phase and frequency errors are well behaved and remain below 11 m and 0.6 mps, respectively, throughout the flight. These errors exhibit an rms level larger than the baseline case (Fig. 4.2-4), but the error growth which would be present due to acceleration and shock (Figs. 4.2-11 and 4.2-13) does not appear.

User navigation performance in the presence of a worst case environment is shown in Fig. 4.2-15 with the user filter modified to "acknowledge" the significant error sources. These changes to the user filter will have a minor adverse effect on user navigation performance when the environmental errors are not present (as represented by the baseline case). This is illustrated in Fig. 4.2-16 in which the baseline run (see Fig. 4.2-4) was repeated with the user filter modified to take into account the possibility of environmentally in- duced errors. The apparent degradation in vertical channel performance is associated with the particular random sequence generated in this Monte Carlo run. Throughout the flight, the clock phase and frequency estimation errors exhibit larger excursions than in the previous baseline run due to the increased uncertainty attributed to these states in the user filter.
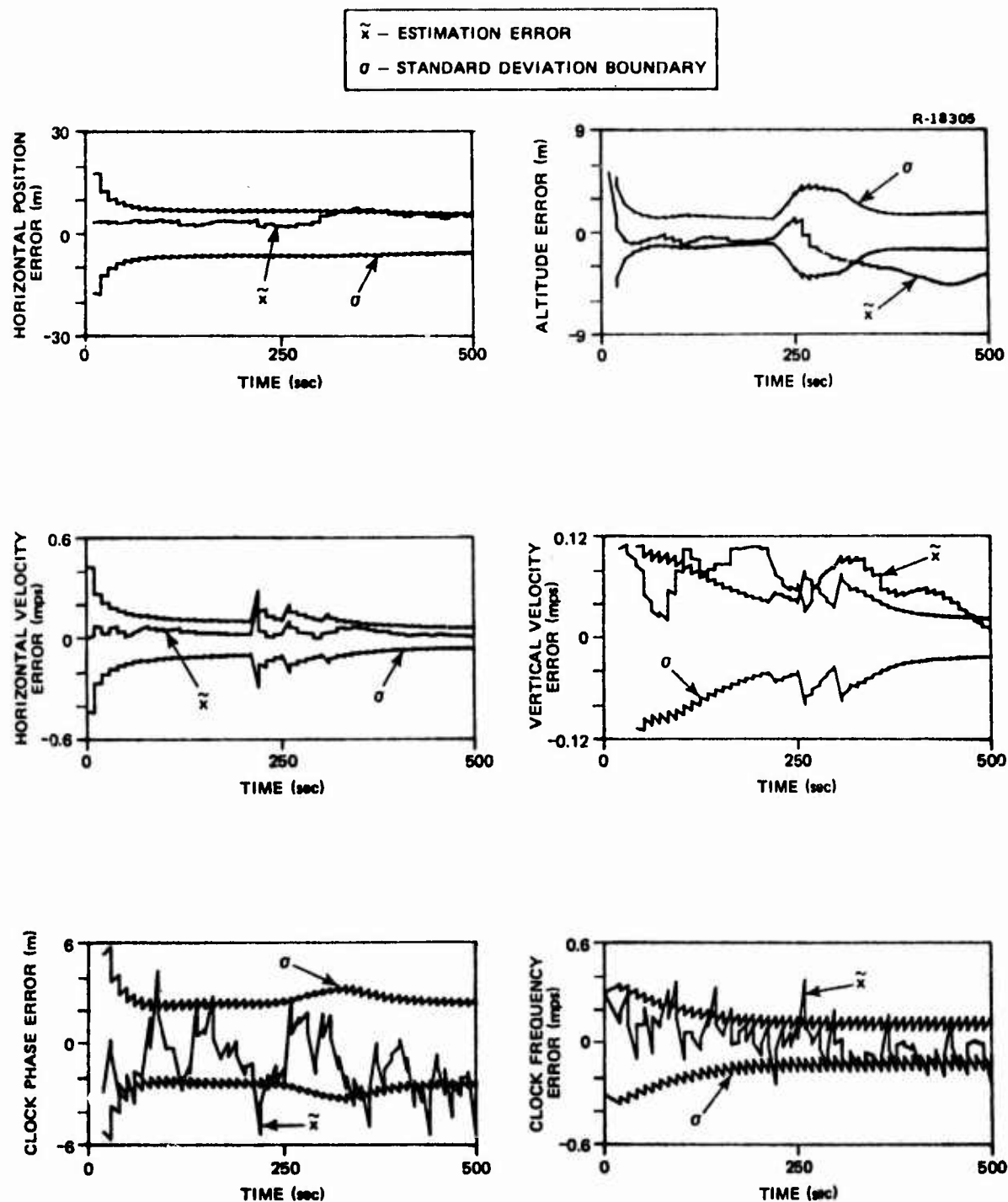
Figure 4.2-16   Airborne User Errors — Modified User Filter
(No Environmental Error Sources)

109

4.2.4 Airborne User Performance Summary

The results of the airborne user performance analysis may be summarized as follows:

- Acceleration, shock and warm-up of the GPS receiver quartz crystal oscillator are the dominant environmental error sources. The temperature and vibration sensitivities of the oscillator and the effect of a degraded quality oscillator have minimal impact on user navigation errors.

- The environmental error sources have direct impact upon the oscillator phase and frequency errors. Due to the high correlation between clock errors and vertical channel errors, large unmodeled phase and frequency errors tend to increase altitude and vertical velocity errors at filter updates; i.e., the filter cannot properly attribute the large pseudo-range and pseudo-range-rate measurement residuals to the clock states alone and thus "divides" the large residual between clock and vertical channel errors. The horizontal position and velocity errors are insensitive to all but extreme environmentally induced errors (e.g., acceleration).

- A simple modification of the user filter to model oscillator warm-up and the effects of acceleration and shock substantially improves user navigation performance, if these error sources are present. However, in the absence of these errors, the modified filter introduces some degradation in user navigation performance. Careful "tuning" of the user filter or an adaptive filtering mechanization could reduce this sensitivity.

5.   SUMMARY AND CONCLUSIONS

        Performance studies of Army users of the NAVSTAR
Global Positioning System (GPS) in a battlefield environ-
ment are presented in this report.   These studies represent
a continuation of an earlier Army user performance analysis
conducted by TASC and reported in Ref. 1.   The problems
analyzed in this report include an assessment of the impact
on the Army manpack GPS user navigation performance of the
use of directional receiver antennas.   These antennas can
be employed to increase the GPS navigation signal strength
while reducing the users' vulnerability to jamming.   Methods
of countering jamming threats are considered and evaluated.
An assessment is also made of the environmentally-induced
error effects of the user receiver crystal oscillator (clock)
on navigation performance.

5.1   STUDY HIGHLIGHTS

        User Performance with Directional Antennas — The
extent to which directional antennas restrict user satel-
lite visibility and the degradation in navigation perform-
ance which results with their use were investigated in
this report.   The navigation performance of a stationary
user with a 120 deg beamwidth antenna is illustrated in
Fig. 5.1-1a.   After the initial transient period (during
which the initial set of measurements to the four visible
satellites are being made), the uncertainty of the posi-
tion estimates of this restricted visibility user is
greater than if satellite visibility was unrestricted,

111
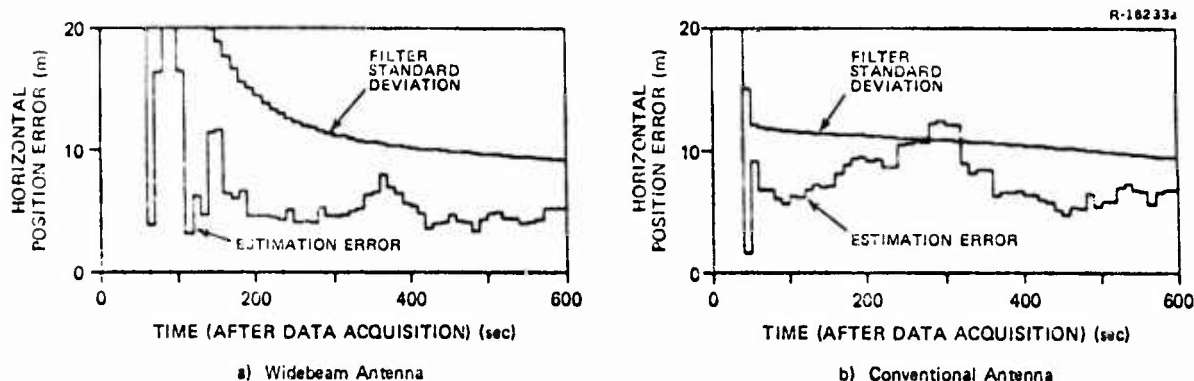
Figure 5.1-1   Horizontal Position Error with
                 Wide Beam and Omni-Directional
                 Antennas

as illustrated in Fig. 5.1-1b. This is attributed to a
poor GDOP condition for the four satellites available with
the 120° beamwidth antenna.

A stationary manpack user could significantly in-
crease the strength of navigation signals while reducing
his vulnerability to jamming by employing a very narrow
beam directional antenna which restricts visibility to one
satellite. This antenna must be physically pointed by the
user (with directions provided by his GPS navigation com-
puter) to each satellite for measurements. This antenna/
deployment concept was evaluated in this study, indicating
that performance comparable to that shown in Fig. 5.1-1 is
achievable after the user has sequenced through five satel-
lites.

As a byproduct of the directional antenna study,
it was discovered that significant improvement in manpack
user performance could be achieved if one additional state
variable ("pseudo-state") per satellite were included in
the user filter software to account for satellite clock
and ephemeris errors. Comparisons of this filter design
with alternative designs are included in this study.

112

Antenna Array Systems — Directional antennas can be constructed from an array of discrete antennas or elements. These antenna arrays can be designed to provide both spatial and frequency filtering to enhance the desired signal while reducing directional interference or jamming. This study indicates significant potential reductions in interference are possible with array antennas for Army GPS manpack users. Futher investigations of methods of implementing the optimum array are required to determine practically realizable performance and cost.

User Vulnerability — The range from a continuous wave jammer within which a ground-based user could be denied access to the GPS signal is illustrated in Fig. 5.1-2 as a function of jammer type and power, and user receiver operating mode. The user receiver is most vulnerable to jamming during initial acquisition of the satellite navigation
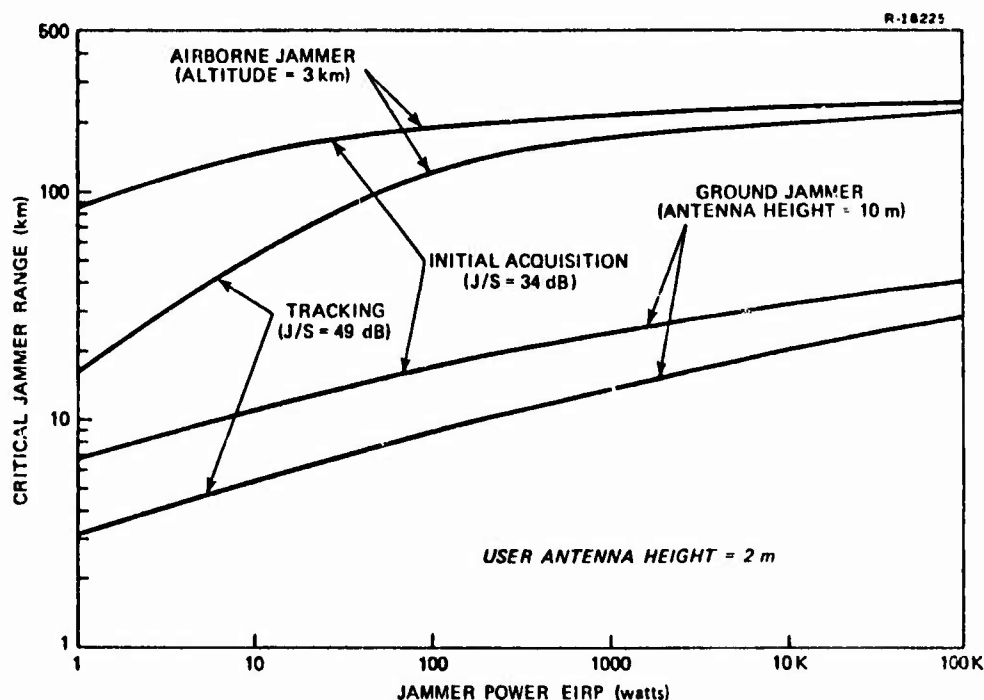
Figure 5.1-2   Critical Jammer Range

signals, because the initial large frequency uncertainty of these signals require a large receiver bandwidth. If the jamming commences <u>after</u> the receiver has acquired the navigation signals, it can operate in the tracking mode with a significant reduction in critical jammer range, as illustrated.

Five techniques of countering a jammer threat that are considered in this report include notch filters, reduced receiver bandwidth (navigation mode only), directional antennas, null steering antennas and RFI screens. It is shown in this report that the null steering antenna and notch filter are most effective against an airborne jammer while a combination of the reduced receiver bandwidth and RFI screen are effective against a ground jammer.

<u>Receiver Clock Error Analysis</u> — An examination of the potential impact of environmentally-induced errors in the GPS receiver quartz crystal oscillator on user navigation performance was conducted. Errors considered in this study include those due to vibration, shock, warm-up, temperature variations and acceleration of the clock platform. A comprehensive model of the oscillator error behavior, under assumed operating conditions, was developed and employed to obtain the performance projections for an airborne (helicopter) user employing a four channel GPS receiver and an inertial navigation system.

<u>The environmental error sources which proved to be dominant are acceleration, shock and oscillator warm-up. The oscillator temperature and vibration sensitivities and the effects of an unknown increase in the oscillator flicker noise level have only a minimal effect on user navigation performance.</u> The navigation performance of the airborne user, illustrating the impact of oscillator acceleration sensitivity (not modeled in the user

Kalman filter) is shown in Fig. 5.1-3a. However, the navigation errors arising from the dominant error sources can be reduced via simple modifications to the user Kalman filter. This is illustrated in Fig. 5.1-3b for the acceleration-sensitive case.
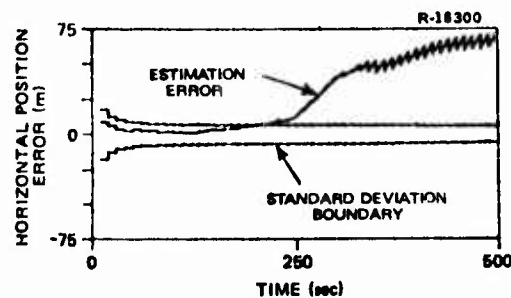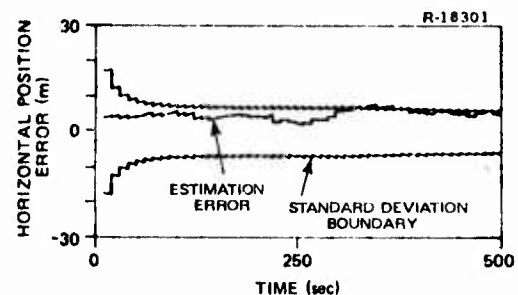
a) Not Modeled in User   b) "Acknowledged" in User
   Kalman Filter   Kalman Filter

Figure 5.1-3   Impact of Quartz Oscillator Acceleration
                  Sensitivity on Airborne User Navigation
                  Performance (see Section 4.2.3)

5.2 RECOMMENDATIONS

This study has indicated the need for additional analytical effort in the following areas:

> User Filter Design — Additional analysis of user filters should be performed with particular emphasis on elimination or compensation of modeling deficiencies. This report has indicated that the addition of pseudo-states is an effective method of compensating for unmodeled satellite ephemeris and clock errors. This technique requires further analysis to determine its full potential and advantages. A method for reducing the impact of unmodeled user clock errors is the inclusion of white process noise in the filter, driving the user clock frequency errors. Optimum determination of the white noise spectral level (i.e., "tuning" of the filter) would require further study.

115

- Interference Reduction Array Implementation — This report has shown the potential advantage of using interference reduction (or null steering) arrays to reduce GPS user vulnerability to jamming. Methods of implementing this technique should be investigated to determine performance, cost and computational requirements. A promising alternative to this technique, not investigated in this study, is the use of a tracking filter (e.g., with phase lock loops).

- User Vulnerability/Receiver Design — This report has illustrated that user vulnerability to jamming is highly dependent upon the threshold jammer-to-signal power ratio of the user receiver. Further analysis of receiver designs are required to determine potential improvements in this threshold for proposed receiver designs. Simulation of the user receiver with jamming in a typical manpack scenario would provide confirmation of user vulnerability. In addition, this analysis could determine the feasibility of reducing the manpack user receiver carrier loop bandwidth to improve his jamming resistance.

APPENDIX A

DIRECTIONAL ANTENNA UTILIZATION CONSIDERATIONS

The effectiveness of directional antennas depends
upon the amount of gain they can provide, as well as their
beamwidth. Increased gain and decreased beamwidth provides
greater immunity to signal interference such as jamming, mul-
tipath, rotor blade modulation and foliage attenuation. To
evaluate the results of Chapter 2, the achievable gain as a
function of beamwidth must be determined. That is the sub-
ject of this appendix. In particular, equations relating
antenna gain, beamwidth and size are developed in Section
A.1. These equations are applied to a parabolic-type an-
tenna in Section A.2. This type of antenna is often used
in high frequency communication systems where medium to high
gain is required. Thus the results of Chapter 2 can be given
some physical interpretation through the equations developed
in this section.

The definitions in this appendix are applicable to
any antenna, although some of the quantities (in particular,
effective cross-sectional area) are difficult to calculate
for most antenna types. References 12 to 15 contain addi-
tional details on antennas. In particular, Ref. 14 con-
tains a good discussion of parabolic antennas.

A.1 ANTENNA CHARACTERISTICS

A measure of an antenna's ability to transmit or re-
ceive radio frequency power is described by its antenna power

pattern $w(\theta,\phi)$, which is defined as the power transmitted in (or received from) a direction (θ,ϕ) per unit solid angle (Refs. 12, 13 and 15). Figure A.1-1 defines the spatial geometry of the antenna used in this report. The conceptually simplest antenna is the ideal isotropic antenna whose antenna pattern is constant (unity) in all directions. The isotropic antenna is often used as a reference with which to compare other antennas.

R -15579
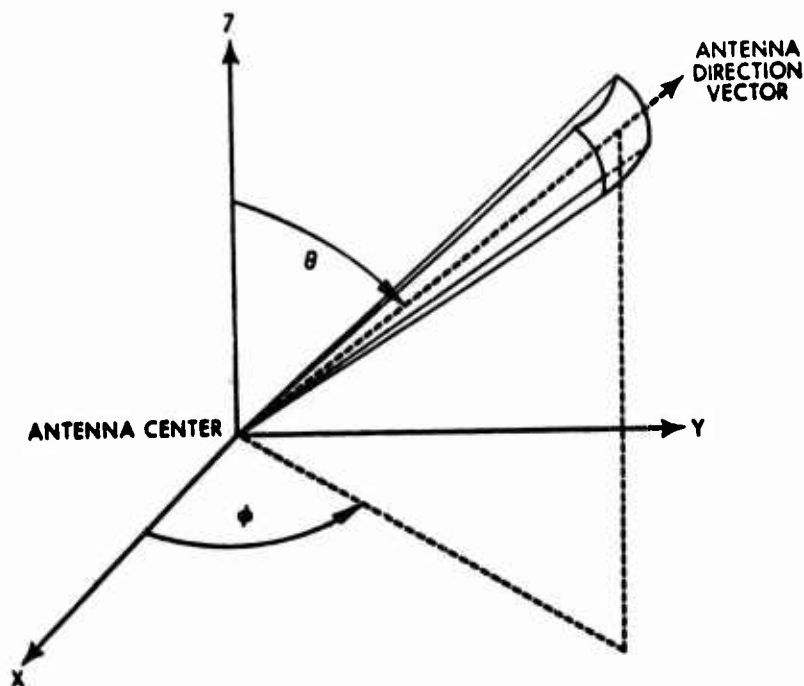
Figure A.1-1 Antenna Spatial Geometry

The total power, P_T, (transmitted or received) associated with an antenna is the surface integral of the antenna pattern over the surrounding sphere of unit radius, i.e.,

$$P_T = \int_{\text{sphere}} w(\theta,\phi) \, d\Omega \qquad (A.1-1)$$

118

The power associated with an ideal isotropic antenna is thus just the surface area of a unit sphere or 4π.

The antenna pattern is often normalized to form the antenna gain function. The normalization term is the power per unit solid angle of an isotropic antenna with the same total power P_T. Thus, the antenna gain function is

$$g(\theta,\phi) = \frac{w(\theta,\phi)}{P_T/4\pi} \tag{A.1-2}$$

The gain or directivity of an antenna is taken as the maximum value of its gain function, i.e.,

$$G = \max_{\theta,\phi} g(\theta,\phi) \tag{A.1-3}$$

or in terms of decibel rating

$$G(db) = 10 \log_{10} G \tag{A.1-4}$$

The actual gain of an antenna is lower than this theoretical gain due to coupling and feed losses. The relation between the theoretical antenna gain G and actual gain G_a is the antenna gain efficiency factor η_g, i.e.,

$$G_a = \eta_g G \tag{A.1-5}$$

The antenna gain efficiency factor, η_g, is typically 50%, thus the actual antenna gain is 3 dB less than the theoretical gain. However, with good design, this efficiency factor may be only 1 to 2 dB.

The antenna solid beamwidth is defined as the solid angle, Ω, through which all of the radiated power would pass if the gain in this angle were constant and equal to its maximum value. Thus, the solid beamwidth is given by

$$\Omega = \frac{P_T}{\max w(\theta, \phi)} = \frac{4\pi}{G} \qquad \text{(A.1-6)}$$

Note that this relation is independent of frequency or an-
tenna size.

The effective cross-sectional area, $a(\theta, \phi)$, of an
antenna is the total power collected at the antenna termin-
als divided by the incident power density in the direction
(θ, ϕ). This is a measure of the amount of power that a re-
ceiving antenna can absorb from a passing wave. The physical
antenna area A_a is related to the maximum cross-sectional an-
tenna area $A = \max a(\theta, \phi)$ by the antenna aperture efficiency
factor η_a, i.e.,

$$A = \eta_a A_a \qquad \text{(A.1-7)}$$

Thus, the maximum cross-sectional area of an antenna is al-
ways less than the physical area of the antenna due to the
aperture efficiency factor.

The maximum cross-sectional area of an antenna can
be expressed in terms of antenna gain and signal wavelength
by (Ref. 13)

$$A = \frac{G\lambda^2}{4\pi} \qquad \text{(A.1-8)}$$

where λ is the radio frequency wavelength of the signal.
Equations (A.1-6) and (A.1-8) illustrate the relationship
between antenna gain, beamwidth and size. Antenna gain is
directly proportional to (frequency)^2 and antenna size. An-
tenna beamwidth is inversely proportional to frequency and
antenna size.

120

A.2 PARABOLIC ANTENNA PARAMETERS

The gain of an antenna as a function of beamwidth and antenna efficiency factor is [from Eqs. (A.1-5) and (A.1-6)]

$$G_a = \eta_g \frac{4\pi}{\Omega} \tag{A.2-1}$$

The solid angle beamwidth Ω is the surface area of that segment of a unit sphere which intersects a solid cone with conical angle β and apex at the center of the antenna, as illustrated in Fig. A.2-1. From spherical calculus, the relation between Ω and conical beamwidth β is

$$\Omega = 2\pi[1 - \cos(\beta/2)] \tag{A.2-2}$$

R - 15580
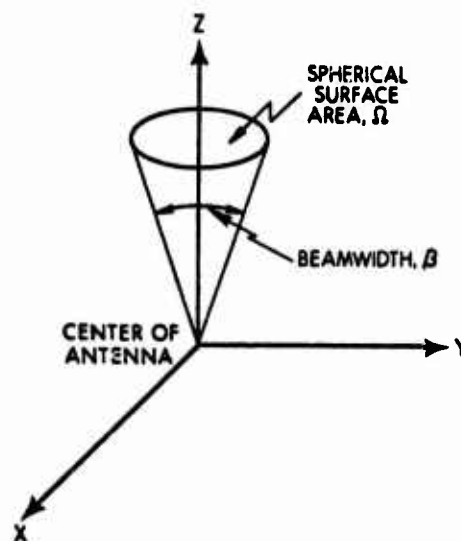
Figure A.2-1   Definition of Beamwidth of a Parabolic Antenna

Combining Eqs. (A.2-1) and (A.2-2), the antenna gain G_a as a function of (conical) beamwidth β is

121

$$G_a = \frac{2 \eta_g}{[1 - \cos (\beta/2)]} \qquad (A.2-3)$$

This relation is presented in Fig. A.2-2 for two gain efficiency factors expressed in decibels. (The -1 dB and -3 dB efficiency factors correspond to 80% and 50% efficiencies, respectively.)
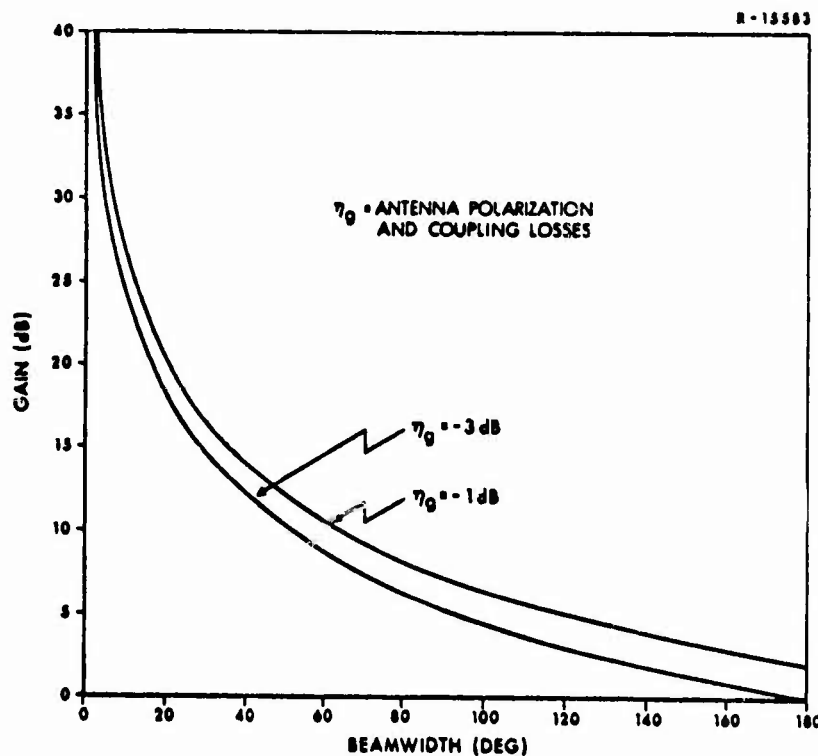
Figure A.2-2   Parabolic Antenna Gain vs Beamwidth

The gain of an ideal parabolic antenna as a function of size is obtained from Eqs. (A.1-5), (A.1-7) and (A.1-8) as

$$G_a = \eta_g \, \eta_a \, \frac{4\pi}{\lambda^2} \, A_a \qquad (A.2-4)$$

The physical area a parabolic antenna presents to a radio frequency wave is the area of the front of the antenna or

$$A_a = \frac{\pi d^2}{4} \qquad (A.2-5)$$

122

where d is the diameter of the antenna "dish." Thus, the gain of a parabolic antenna, in terms of its diameter, is

$$G_a = \eta_g \, \eta_a \left(\frac{\pi d f}{c}\right)^2 \qquad\qquad (A.2-6)$$

where

f is signal frequency in hertz

c is propagation constant = 3×10^8 meters/sec

d is diameter of parabolic antenna in meters

This relation is presented in Fig. A.2-3 for efficiency factors of -1 dB and the two GPS navigation signal frequencies.
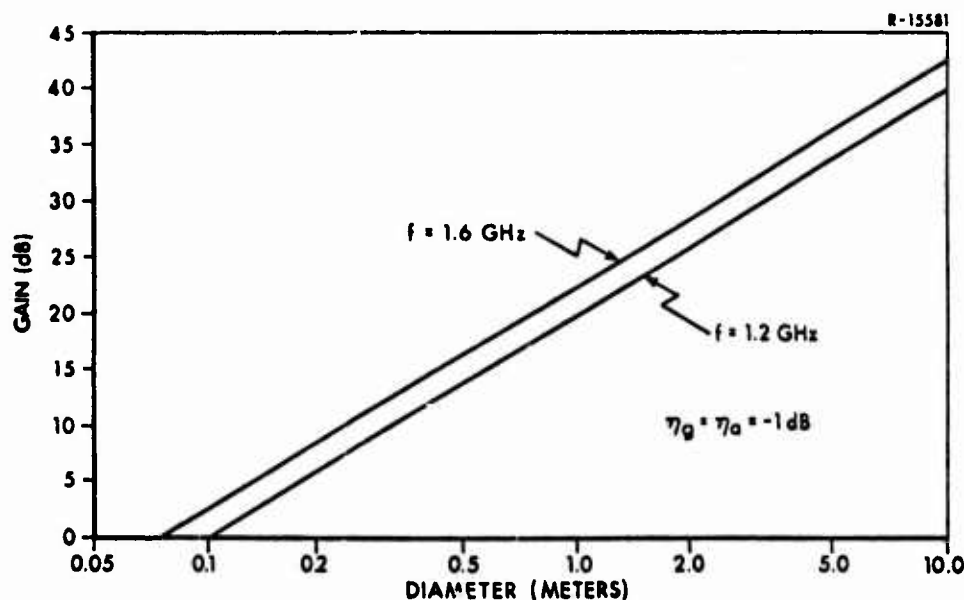
Figure A.2-3   Parabolic Antenna Gain vs Diameter

The beamwidth of a parabolic antenna as a function of its size or diameter is obtained from Eqs. (A.1-6), (A.1-7), (A.1-8), (A.2-2) and (A.2-5) as

$$\beta = 2 \cos^{-1}\left[1 - \frac{2}{\eta_a\left(\frac{\pi d}{\lambda}\right)^2}\right] \qquad\qquad (A.2-7)$$

123

where

  η_a is antenna aperture efficiency factor

  d is antenna size

  λ is radio frequency wavelength

This relationship is presented in Fig. A.2-4 for an aperture
efficiency factor of -1 dB and the two GPS frequencies.
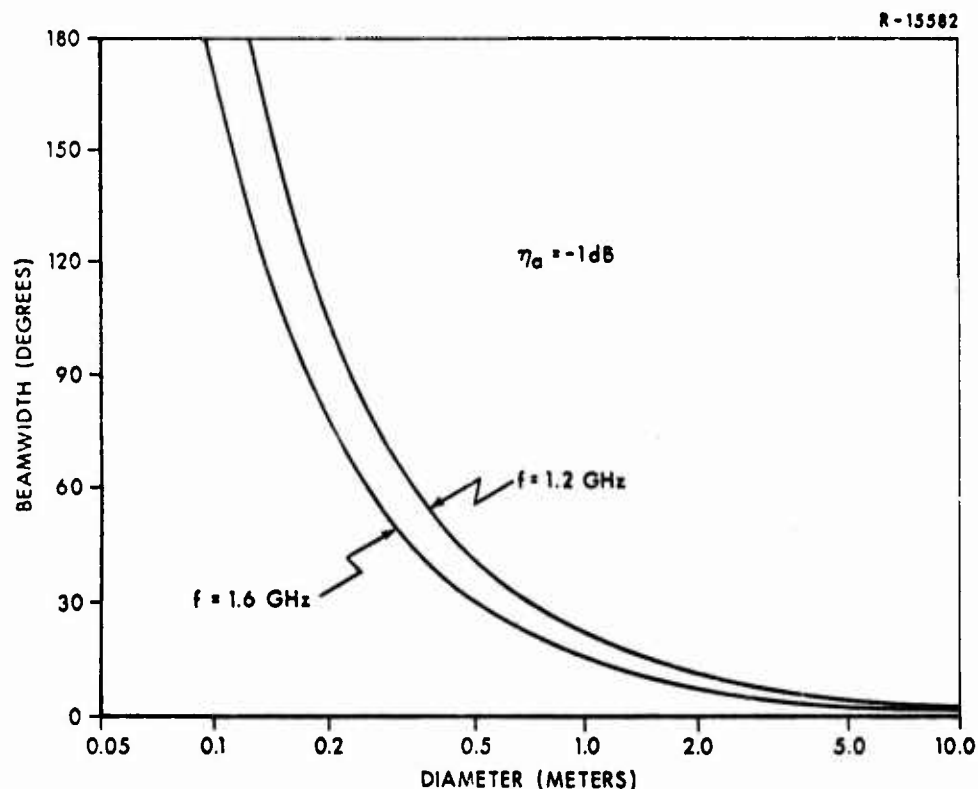
Figure A.2-4   Parabolic Antenna Beamwidth
vs Diameter

This last figure illustrates the different beamwidths
that occur at the two frequencies for a constant antenna size.
For example, if a beamwidth of 140 deg at 1.6 GHz is desired,
the antenna diameter should be 0.12 meters (5 inches). At
1.2 GHz, the beamwidth is 180 deg for this size antenna and
the gain is 2 dB less than at 1.6 GHz. Thus, some compromise
in performance might be required if a single antenna is em-
ployed for both frequencies.

A.3 PARABOLIC ANTENNAS FOR GPS USERS

A parabolic antenna could be employed by a GPS user in order to increase the signal strength at the receiver and to reduce interference such as jamming. The data presented in Section A.2 can be used to determine the amount of signal gain and directivity a user can obtain using parabolic antennas under various operating conditions.

It has been observed in Section 2.1 that the operational Phase III GPS will provide at least four satellite visibility to a user employing a vertical boresight antenna with a beamwidth of 140 deg. From Fig. A.2-2, an antenna with 140 deg beamwidth has a 1.8 to 3.8 dB gain, depending upon the efficiency factor. From Fig. A.2-4, this beamwidth corresponds to an antenna size of 0.12 meters at 1.6 GHz. However, at 1.2 GHz the beamwidth is 180 deg for this antenna size and the gain is 2 dB less. This may not be a serious problem if the higher frequency is used for initial acquisition of the signals. Acquisition of the signals at 1.2 GHz is then relatively easy since the signals on these two frequencies are synchronized. For 120 deg beamwidth, the antenna gain is 3 to 5 dB.

For the narrow beam antenna of Section 2.2, if the bandwidth were 60 deg then a gain of 8.7 to 10.7 dB would be provided with a diameter of 0.26 m at η_a = -1 dB. This represents a significant gain in signal strength which may be desired under foliage conditions. However, this antenna must be physically slewed by the operator to each satellite for acquisition and pseudo-range measurements, since four satellites cannot be seen simultaneously by this antenna.

These examples illustrate the use of the design data developed in Section A.2 to determine user performance improvements and limitations with directional antennas.

APPENDIX B

GPS PHASE III CONFIGURATION AND PERFORMANCE

Realistic user performance projections require realistic satellite ephemerides and measurement data. This data is obtained by simulating the satellites and the ground tracking system that computes the satellite ephemerides which are relayed to the user. The user's performance is thus dependent upon the performance of the tracking system. This appendix presents details of the ground tracking system simulation that was performed to generate the data required in the user performance projections of Sections 2.2 and 4.2. Further details of the simulation program are given in Ref. 2.

This study is concerned with the fully operational Phase III satellite configuration. In order to reduce the computer time required in the tracking system simulation, a subset of the Phase III satellite configuration was used. The satellites selected and the rationale for their selection are discussed in Section B.1. The error models that are peculiar to this study (and thus not in Ref. 2) are presented in Section B.2. Also, the initial conditions used in the tracking filter are given. Finally, the tracking system performance results are summarized in Section B.3. Included are illustrations of typical performance for each of the tracking system error sources.

B.1 SATELLITE CONFIGURATION

The GPS Phase III satellite configuration consists of 24 satellites in a 3 x 8 (three planes, eight satellites

per plane) constellation with each satellite in a 12-hour orbit
inclined 63 deg. The orbital elements of this constellation of
the initiation of the tracking process are summarized in Table
B.1-1 with the satellite geometry shown in Fig. B.1-1.

TABLE B.1-1

GPS PHASE III SATELLITE POSITIONS
AT THE START OF TRACKING

SATELLITE NO.	SEMIMAJOR AXIS	ECCENTRICITY	INCLINATION	RIGHT ASCENSION OF THE ASCENDING NODE	ARGUMENT OF PERIGEE	MEAN ANOMALY
	a	e	i	Ω	ω	M
	earth radii		deg	deg	deg	deg
1	4.16449	0	63	0	0	15
2	4.16449	0	63	0	0	60
3	4.16449	0	63	0	0	105
4	4.16449	0	63	0	0	150
5	4.16449	0	63	0	0	195
6	4.16449	0	63	0	0	240
7	4.16449	0	63	0	0	285
8	4.16449	0	63	0	0	330
9	4.16449	0	63	120	0	345
10	4.16449	0	63	120	0	30
11	4.16449	0	63	120	0	75
12	4.16449	0	63	120	0	120
13	4.16449	0	63	120	0	165
14	4.16449	0	63	120	0	210
15	4.16449	0	63	120	0	255
16	4.16449	0	63	120	0	300
17	4.16449	0	63	240	0	0
18	4.16449	0	63	240	0	45
19	4.16449	0	63	240	0	90
20	4.16449	0	63	240	0	135
21	4.16449	0	63	240	0	180
22	4.16449	0	63	240	0	225
23	4.16449	0	63	240	0	270
24	4.16449	0	63	240	0	315

The user scenarios in this report are relatively short
(less than one hour) and thus, only a limited set of satellites
will be visible to the user during this period. The computer
time required to provide a realistic tracking system simulation
is dependent upon the number of satellites used. This time can
be reduced if only those (four) satellites which are visible and
provide the best GDOP to a user (with a conventional antenna)
during the scenario time period are included in the tracking
system simulation. A wide beam (120 deg) directional antenna
user will see three of these four satellites, plus a fifth.
Thus, five satellites were included in the simulation.

127
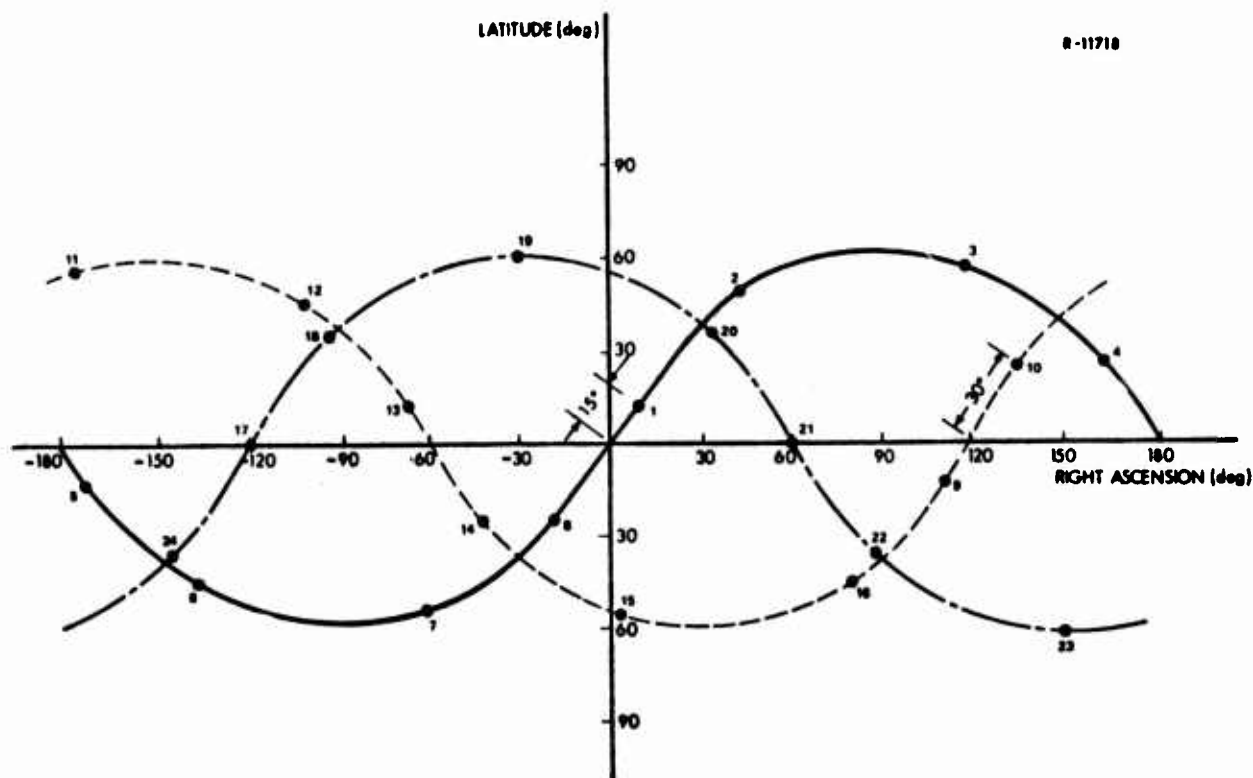
Figure B.1-1 GPS Phase III Orbit Configuration
(Inertial Coordinates)

The satellites chosen to include in the simulation
are listed in Table B.1-2 and correspond to Satellite Nos.
10, 11, 12, 17, and 18, respectively, in Table B.1-1. These

TABLE B.1-2

SATELLITE ORBITAL ELEMENTS AT THE
START OF TRACKING

SATELLITE NO.	SEMIMAJOR AXIS	ECCENTRICITY	INCLINATION	RIGHT ASCENSION OF THE ASCENDING NODE	ARGUMENT OF PERIGEE	MEAN ANOMALY
	a	e	i	Ω	ω	M
	earth radii		deg	deg	deg	deg
1	4.16449	0	63	120	0	30
2	4.16449	0	63	120	0	75
3	4.16449	0	63	120	0	120
4	4.16449	0	63	240	0	0
5	4.16449	0	63	240	0	45

128

five satellites provide a wide range of satellite visibility and GDOP conditions to users located at latitude +50 deg, longitude -100 deg as illustrated in Fig. B.1-2. Ground tracks of these five satellite subpoints during a three-hour period are illustrated in Fig. B.1-3. The satellite points along each ground track at one-hour intervals are depicted by hatch marks.
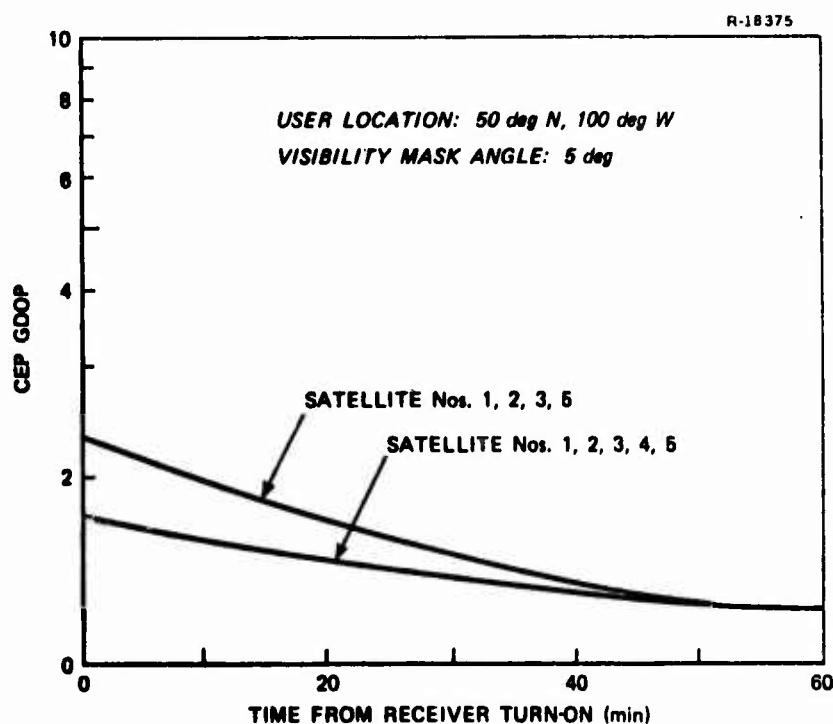
Figure B.1-2   User GDOP and Visibility

The ground tracking system was simulated for 49 hours of simulation time at which point the user scenarios were initiated. The simulation then continued for three hours or to 52 hours after the commencement of the simulation. Thus, the user scenarios can last up to three hours.
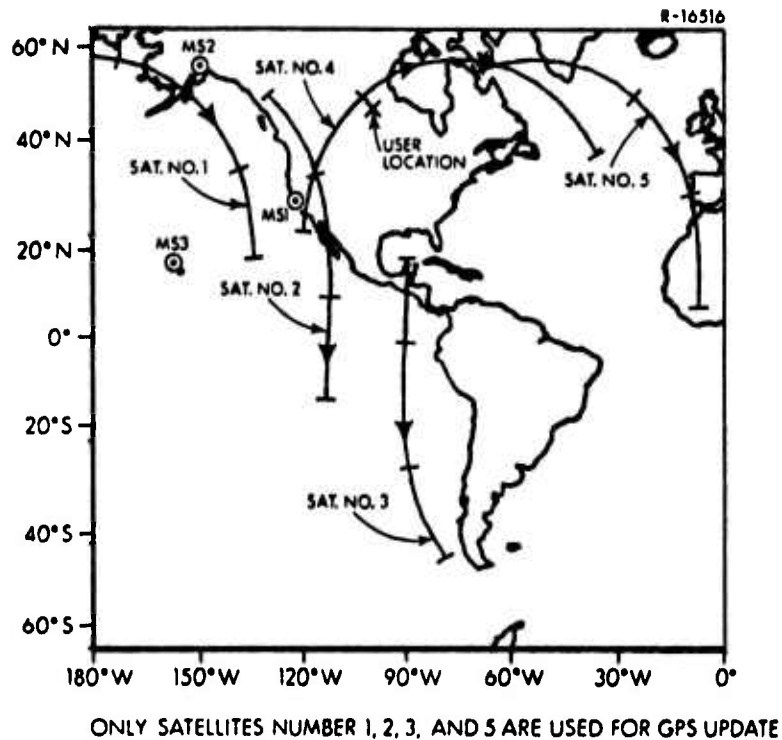
Figure B.1-3   Satellite Ground Tracks

B.2   ERROR MODELS

The five satellites are tracked by an "optimal" filter in that it is assumed that all unknown quantities which will have an impact on the orbital estimation process are included as state variables in the filter. Also the statistics associated with each state variable are assumed to be modeled correctly.

The details of the error models used in this simulation are given in Ref. 2 and summarized in Ref. 1. The only significant changes to these error models were a reduction of some of the initial estimation errors (especially a 2% solar radiation force uncertainty and a reduction in gravitational constant uncertainty) and the incorporation of a new model for the satellite and monitor station clocks.

130

The new clock model is of a high performance cesium beam tube time standard and consists of three states: phase error, frequency error and a one-state flicker noise modeled as a Markov process with a time constant of approximately one day. (Ref. 3 and Appendix C). This clock model, illustrated in Fig. B.2-1, is based on data contained in Ref. 4. The fractional frequency

Figure B.2-1   Cesium Beam Clock Error Model

stability plot for this clock model is shown in Fig. B.2-2. The error states for the model are defined in Table B.2-1. The spectral density (continuous) matrix associated with this clock model is given by Eq. (B.2-1). The parameters k_1, k_2 and β shown in Fig. B.2-1 have values 0.1, 0.03 and 1×10^{-5}, respectively.

The satellites are tracked by four ground tracking stations located in the northern hemisphere in United States territory. The locations of the tracking stations are given in Table B.2-2 with the first three also shown in Fig. B.1-2.

131

R—16596

Figure B.2-2   Fractional Frequency Stability Data
for Cesium Beam Clock Model

TABLE B.2-1

CESIUM BEAM CLOCK ERROR STATE DEFINITIONS

SYMBOL	ERROR SOURCE DEFINITION	UNITS
$\delta\phi$	Clock Phase Error	m
δf	Clock Frequency Error	mps
x_f	Flicker Noise	mps

132

$$Q = \begin{bmatrix} 7.35 \times 10^{-6} & 0 & 5.95 \times 10^{-10} \\ 0 & 1.11 \times 10^{-15} & 0 \\ 5.95 \times 10^{-10} & 0 & 5.35 \times 10^{-13} \end{bmatrix} \qquad (B.2\text{-}1)$$

TABLE B.2-2

GROUND TRACKING STATION LOCATIONS

STATION NO.	NAME	LATITUDE deg	LONGITUDE deg	ASSUMED ALTITUDE m
1	Vandenberg AFB	34.7	-120.5	0
2	Elmendorf AFB	61.3	-149.5	0
3	Hawaii	20.0	-158.0	0
4	Guam	13.0	145.0	0

Uploading of the satellites with current ephemeris data occurs once a day when the individual satellites make their closest approach to the master tracking station at Vandenberg AFB. The time of the uploading to each satellite is given in Table B.2-3.

TABLE B.2-3

SATELLITE DAILY INFORMATION UPLOADING TIMES

SATELLITE NO.	TIME (min)
1	210
2	90
3	1395
4	105
5	1380

The ionospheric and tropospheric delay errors are assumed to be accounted for perfectly in the measurements, and the only measurement error is a normally-distributed white measurement noise with zero mean and variance of $(0.3m)^2$.* Measurements are processed at 15-minute intervals for all satellites in view of the ground tracking stations, while the filter states are propagated between these measurements using one-minute integration steps. The tracking filter was initialized with the filter statistics presented in Table B.2-4.

B.3 PERFORMANCE RESULTS

Typical results of the satellite tracking system for the 52 hours of simulation time are summarized in this section. These results are presented in the form of time histories of the estimation error as well as the tracking filter standard deviation boundary for an error state. The standard deviation boundaries are computed by taking the square root of the diagonal element of the covariance matrix corresponding to the particular error of interest and plotting plus-and-minus the value. Theory says (Ref. 5) that if everything is modeled properly, the estimation error should not go outside that standard deviation boundary more than 31.7% of the time. If the filter estimate is seen to diverge outside the boundary, then the filter does not properly model the physical process, and a filter redesign is in order.

Typical performance of the tracking system in estimating satellite ephemerides is illustrated in Figs.B.3-1 and B.3-2. These show the error in estimating the Z-component[†]

---

*This value assumes prefiltering of the tracking data over the 15 minute update intervals.

†The Z-component lies along the earth's polar axis.

TABLE B.2-4

TYPICAL TRACKING FILTER INITIAL CONDITIONS

| SYMBOL	STATE DEFINITION	INITIAL ESTIMATION ERROR		INITIAL FILTER STANDARD DEVIATION		CORRELATION TIME (sec)	DISCRETE PROCESS NOISE VARIANCE	
		VALUE	UNITS	VALUE	UNITS		VALUE	UNITS
$\delta\hat{R}_4$	Satellite No. 4 Position Error	19.1, -5.3, 11.4	m	61	m	—	5.8×10^{-9}	m^2
$\delta\hat{V}_4$	Satellite No. 4 Velocity Error	-0.0005, 0.0053, -0.0012	mps	0.003	mps	—	2.1×10^{-14}	$(mps)^2$
$\delta\hat{\phi}_{s4}$	Satellite No. 4 Clock Error	61	m	61	m	—	⎫	m^2
$\delta\hat{f}_{s4}$		0.27×10^{-3}	mps	3×10^{-3}	mps	—	⎬ Discrete Form of Eq. (B.2-1)	$(mps)^2$
$\hat{x}_{fs4}$		0.09×10^{-3}	mps	0.16×10^{-3}	mps	10^4	⎭	$(mps)^2$
$\delta\hat{SR}_4$	Satellite No. 4 Solar Radiation Force Uncertainty	1.4×10^{-9}	m/sec^2	1.8×10^{-9}	m/sec^2	3600	1.27×10^{-18}	m^2/sec^4
$\delta\hat{R}_{G3}$	Monitor Station No. 3 Location Uncertainty	4.0, 10.7, 6.4	m	9	m	∞	0	—
$\delta\hat{\phi}_{r3}$	Monitor Station No. 3 Clock Error	6.7	m	61	m	—	⎫	$(m)^2$
$\delta\hat{f}_{r3}$		0.02×10^{-3}	mps	3×10^{-3}	mps	—	⎬ Discrete Form of Eq. (B.2-1)	$(mps)^2$
$\hat{x}_{fr3}$		0.19×10^{-3}	mps	0.16×10^{-3}	mps	10^4	⎭	$(mps)^2$
$\delta\hat{\mu}$	Gravitational Constant Uncertainty	3.99×10^7	m^3/sec^2	7.97×10^7	m^3/sec^2	∞	0	—
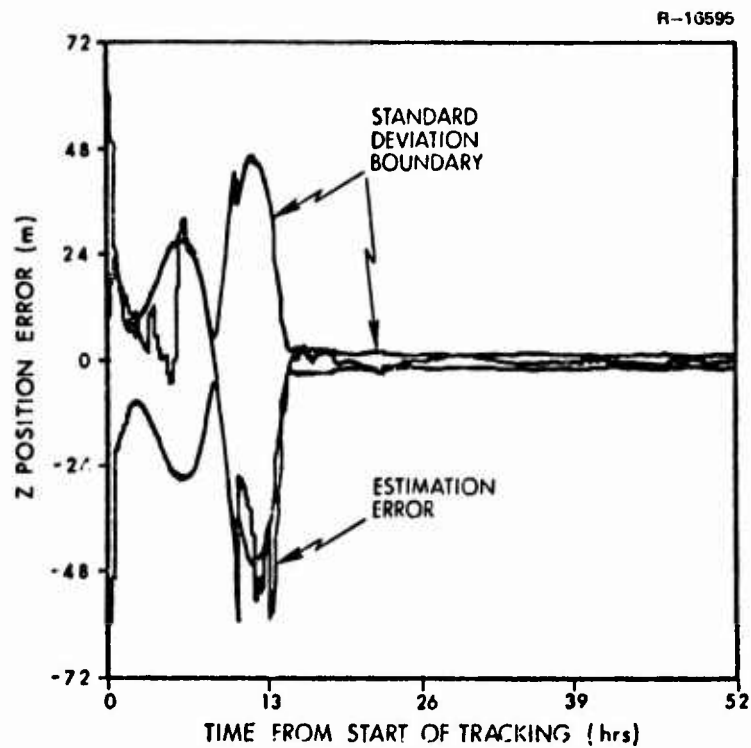
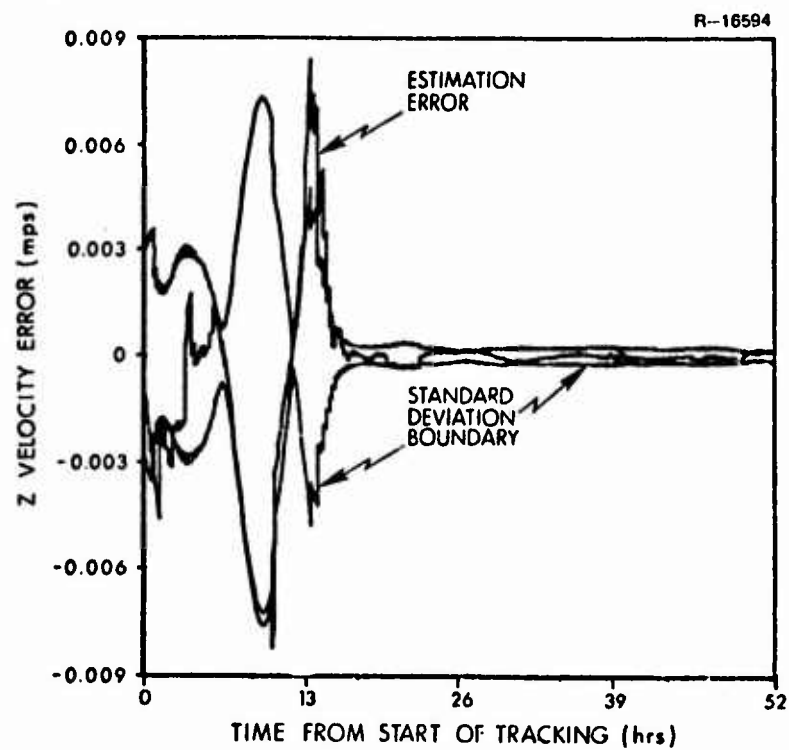Figure B.3-1   Satellite No. 4 Position Error

Figure B.3-2   Satellite No. 4 Velocity Error

136

of the position and velocity of Satellite No. 4. Satellite
No. 4 is tracked for the first five hours after start of
tracking and then again from the 14th and 16th hour after
the start of tracking. These tracking periods are repeated
every 24 hours. After the second period of tracking, the
estimation errors are well within the standard deviation
boundary, indicating that the filter has estimated the
satellite position and velocity accurately. Similar behavior
was noted for the other two error components. The behavior
of the filter in estimating the position and velocity of
Satellite No. 4 after the initial transient has died out is
illustrated more clearly in Figs. B.3-3 and B.3-4, respec-
tively. These results indicate that the steady state per-
formance of the tracking filter is well behaved and thus the
errors are properly modeled.

The errors in estimating the states of the clock
in Satellite No. 4 are illustrated in Figs. B.3-5, B.3-6,
and B.3-7 for the clock phase, frequency and flicker noise,
respectively. The clock phase and frequency error appear
to become stabilized after the second period of tracking as
was evident for the satellite position and velocity errors.
The flicker noise error does not become stabilized since
this state is driven by random disturbances or noise. How-
ever, the flicker noise error stays mostly within the fil-
ter's standard deviation boundary which indicates that the
error is bounded and thus properly modeled in the filter.

The uncertainty in estimating the solar radiation
force on Satellite No. 4 is illustrated in Fig. B.3-8.
Solar radiation force uncertainty is modeled as a random
Markov process and can only be estimated during periods of
visibility of the satellite from at least one tracking sta-
tion. Since the initial uncertainty was 2%, further reduc-
tions will not be noticed in these results.

137

R–16621
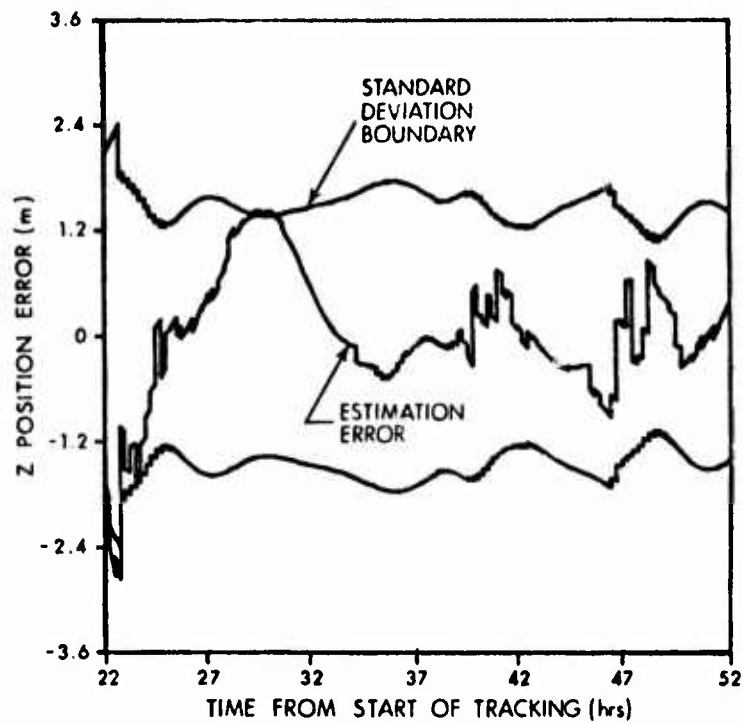

Figure B.3-3   Satellite No. 4 Position Error
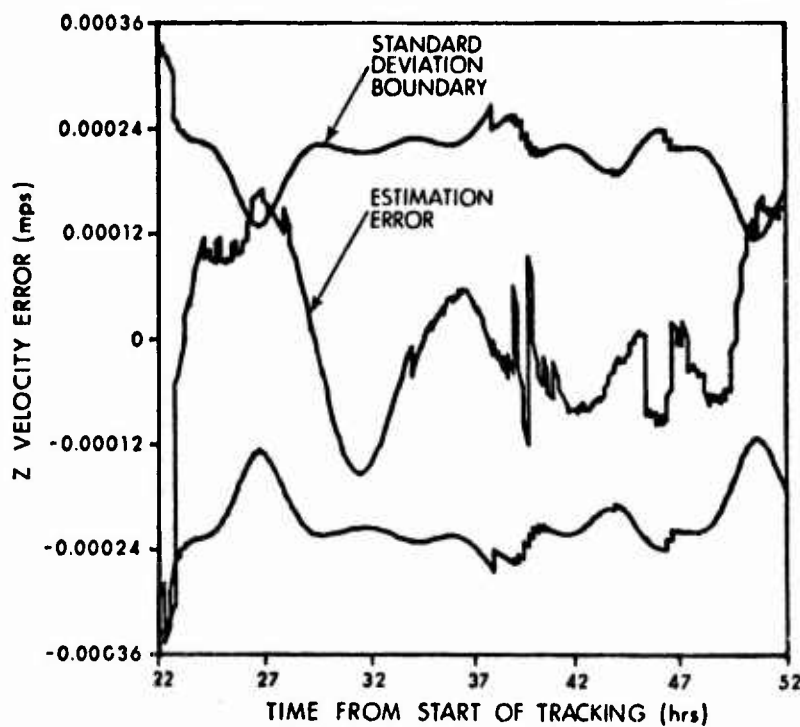
R–16620

Figure B.3-4   Satellite No. 4 Velocity Error

138
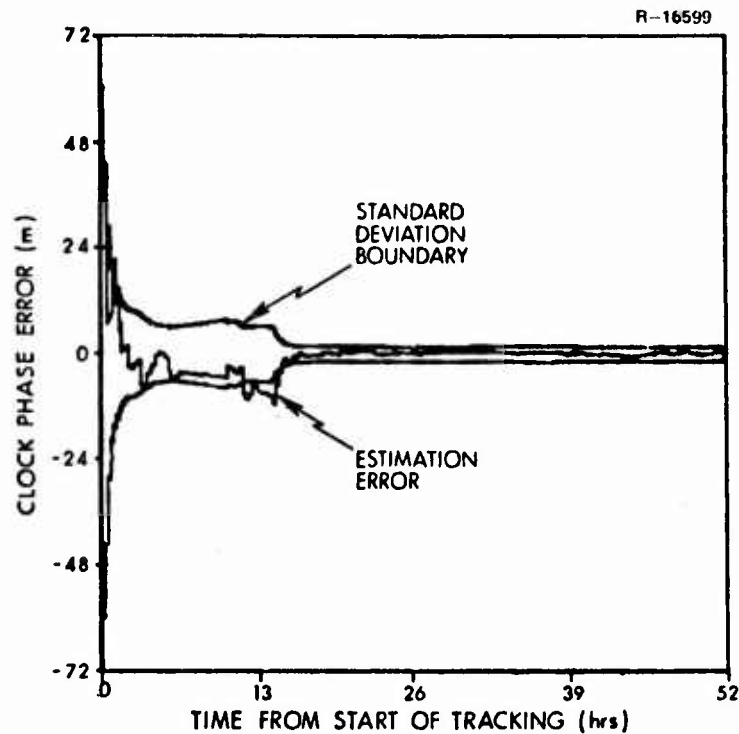
Figure B.3-5   Satellite No. 4 Clock Phase Error
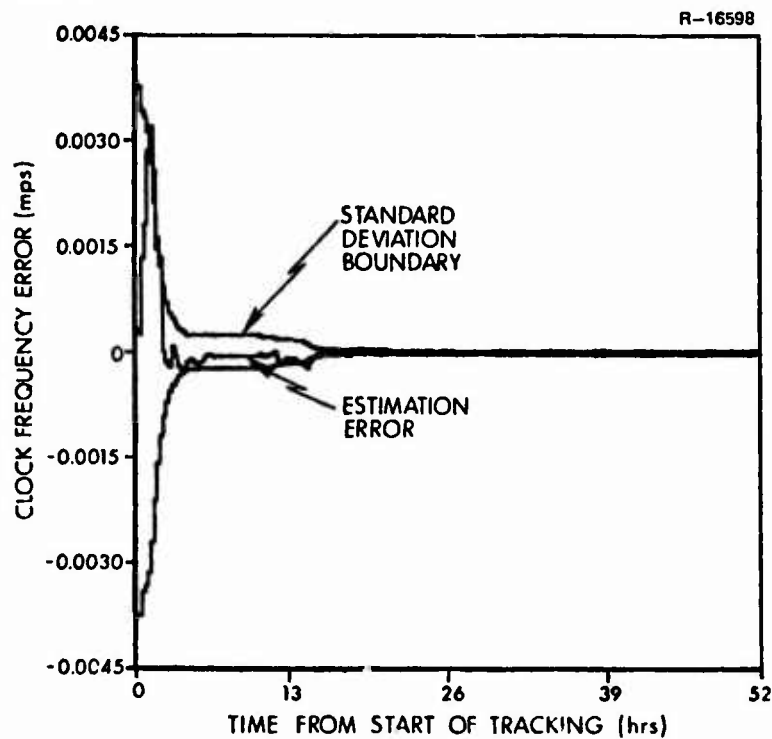
Figure B.3-6   Satellite No. 4 Clock Frequency Error

139
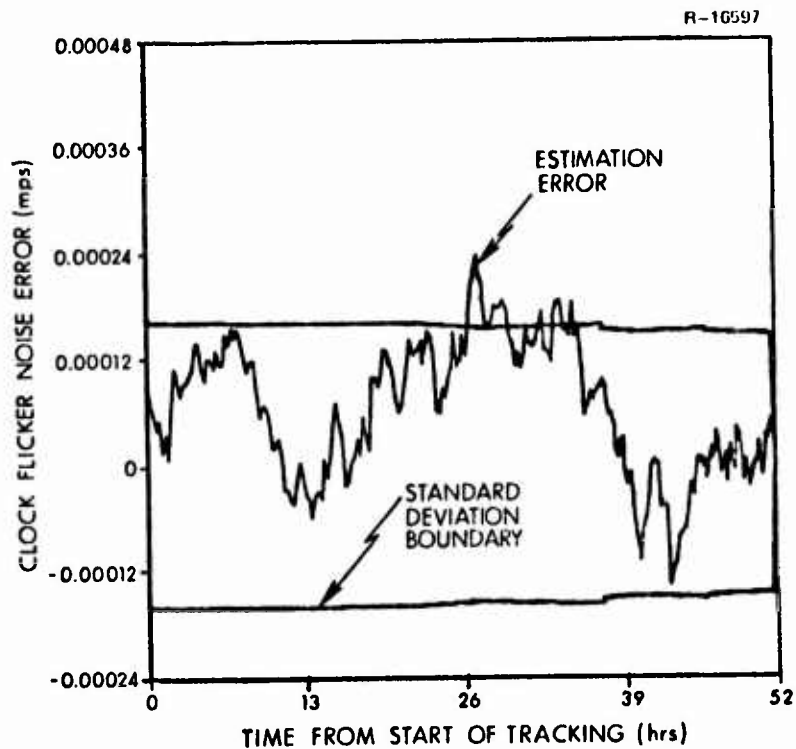
Figure B.3-7   Satellite No. 4 Clock
                Flicker Noise Error
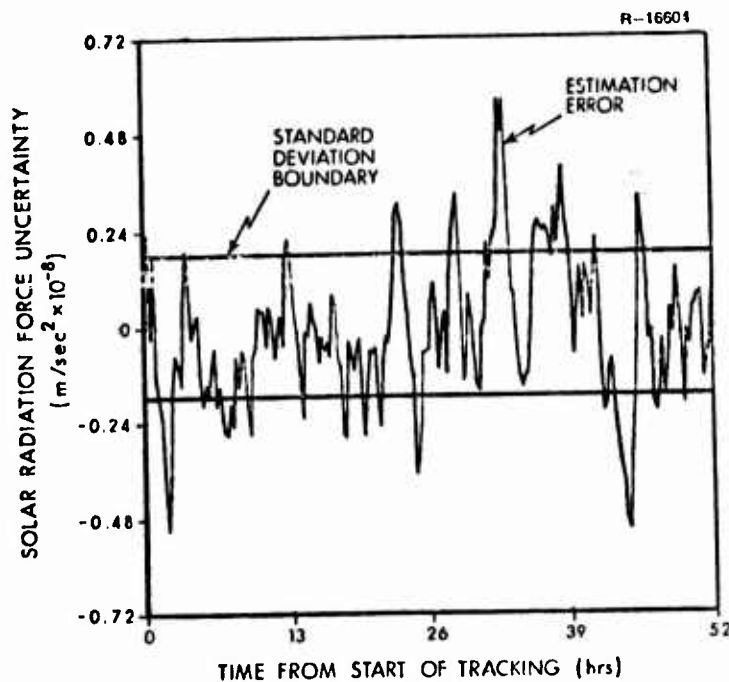
Figure B.3-8   Satellite No. 4 Solar Radiation
                Force Uncertainty

140

The uncertainty in the ground tracking station loca-
tions is modeled in the tracking filter as a bias. Typical
performance of the tracking filter in estimating station loca-
tions is illustrated in Fig. B.3-9, which shows the error in
estimating the Z-component of Monitor Station No. 3 location.
Similar performance results occur for the other components
of the location error and for the other tracking stations.
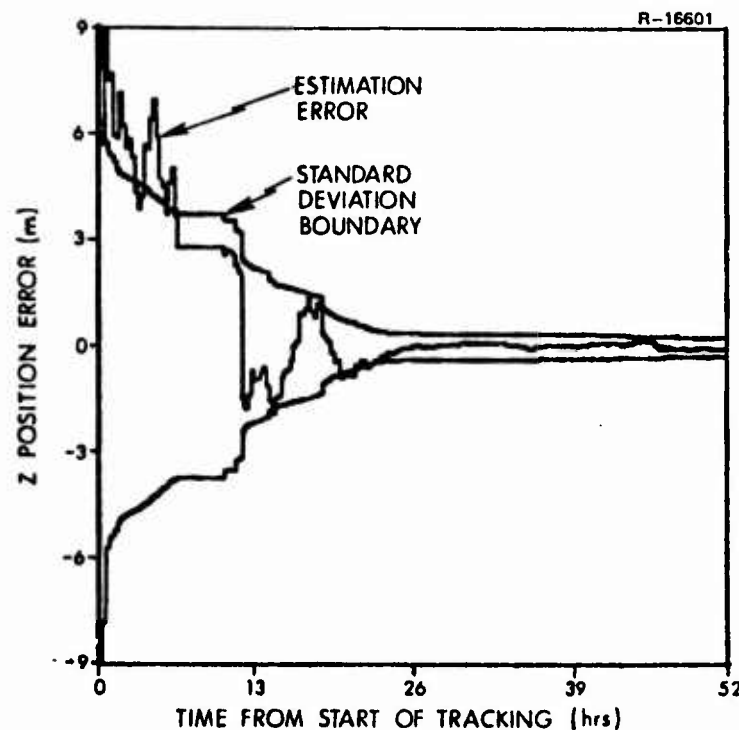
Figure B.3-9   Monitor Station No. 3 Location Error

The clocks in the monitor stations are the same as
the satellite clocks and exhibit similar behavior as illus-
trated in Figs. B.3-10, B.3-11, and B.3-12 for Monitor Sta-
tion No. 3. The estimation errors tend to be within the
standard deviation boundaries thus indicating that the fil-
ter is doing a good job of estimating the monitor station
clock errors. Similar behavior is evident with the other
monitor station clocks.

141
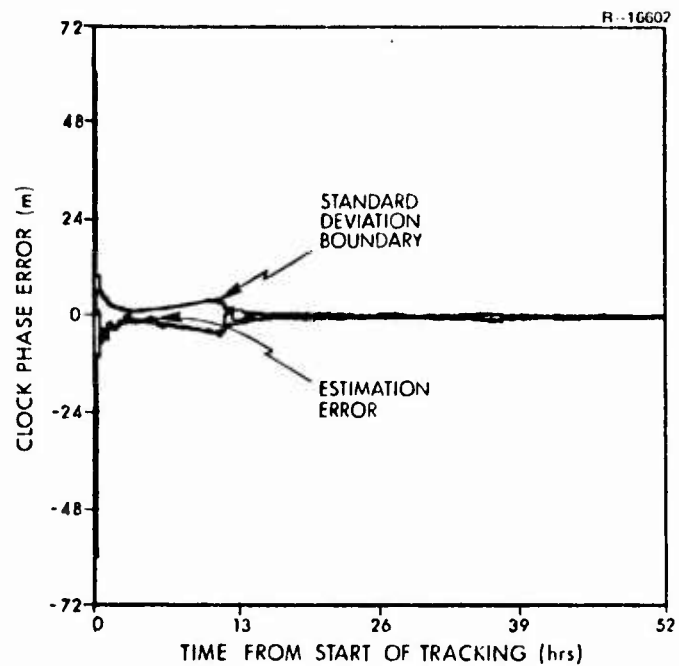
Figure B.3-10   Monitor Station No. 3
                     Clock Phase Error
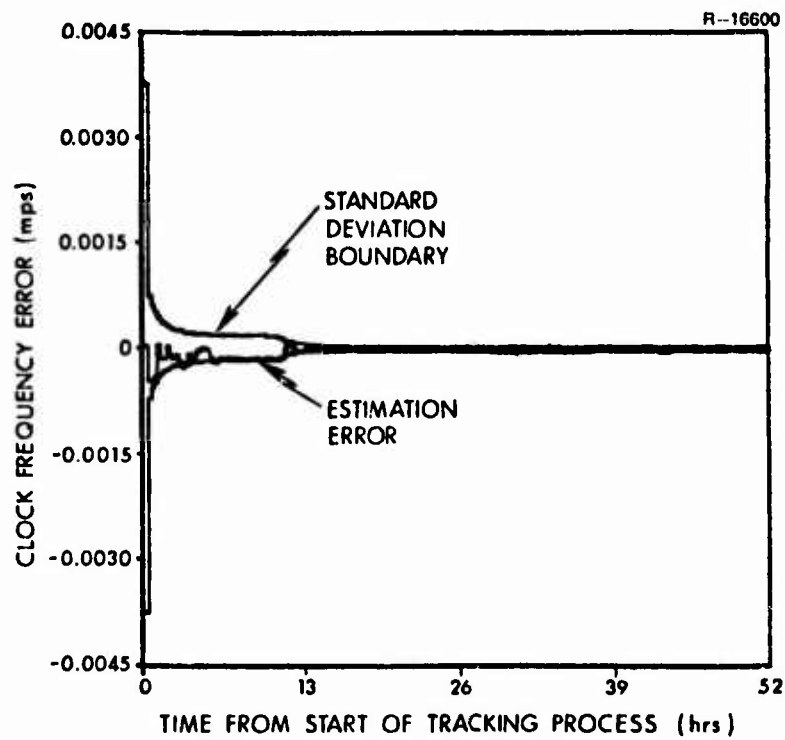
Figure B.3-11   Monitor Station No. 2
                     Clock Frequency Error

142
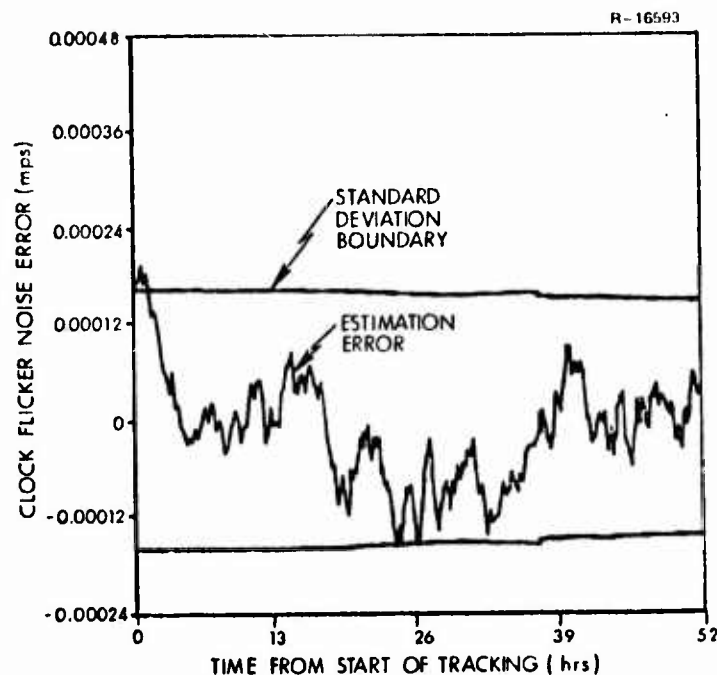
Figure B.3-12   Monitor Station No. 3
                        Clock Flicker Noise Error

The gravitational uncertainty influences all satellite orbits and is modeled as a bias. The error in estimating this uncertainty is illustrated in Fig. B.3-13. Because of the small initial uncertainty in this parameter, the filter does not significantly reduce the uncertainty during the simulation tracking period.

The performance of the tracking filter after 49 hours of tracking is summarized in Table B.3-1. The initial errors and their standard deviations in addition to the errors and filter statistics at 49 hours, are presented for comparison purposes. These results confirm those presented previously in this section in that there is no evidence of filter divergence indicating the tracking filter is operating properly.

The satellite position and velocity (Z-component) data transmitted by Satellite No. 4 to the users is

143
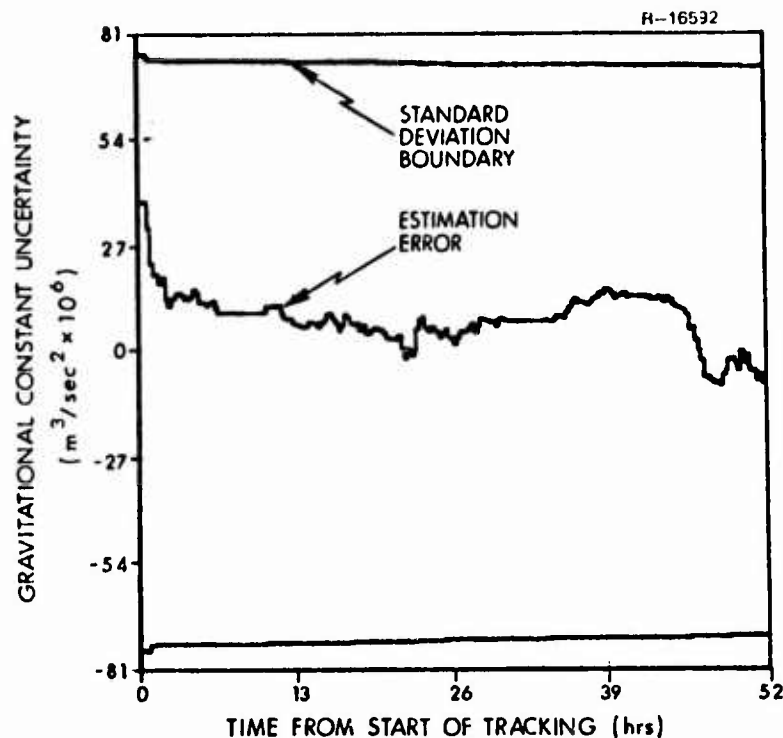
Figure B.3-13   Gravitational Constant Uncertainty

illustrated in Figs. B.3-14 and B.3-15, respectively. Also
shown in these figures is the corresponding estimation er-
ror of the tracking filter. Since this satellite is up-
loaded with data at the 105 min point each day, the satel-
lite data is effectively reset to correspond to that of the
tracking filter at that time. However, because there are
no measurement updates associated with the satellite data,
it tends to diverge slowly from the tracking filter esti-
mates after the uploading.

TABLE B.3-1

TYPICAL TRACKING FILTER PERFORMANCE AT TRACK INITIATION AND AFTER 49 HOURS OF TRACKING

SYMBOL	STATE DEFINITION	UNITS	INITIAL ESTIMATION ERROR	INITIAL FILTER STANDARD DEVIATION	49 HOUR ESTIMATION ERROR	49 HOUR FILTER STANDARD DEVIATION
$\delta\hat{\underline{R}}_{s4}$	Satellite No. 4 Position Error	m	19.1, -5.3, 11.4	61	0.94, 0.12, 0.43	0.9, 1.5, 1.2
$\delta\hat{\underline{V}}_{s4}$	Satellite No. 4 Velocity Error	mps	-0.005, 0.0053, -0.0012	0.003	-0.00003, 0.00012, 0.00006	0.00015, 0.00015, 0.00021
$\delta\hat{\phi}_{s4}$	Satellite No. 4 Clock Error	m	61	61	0.19	1.6
$\delta\hat{f}_{s4}$		mps	0.27×10^{-3}	3×10^{-3}	-0.003×10^{-3}	0.018×10^{-3}
$\hat{x}_{fs4}$		mps	0.09×10^{-3}	0.16×10^{-3}	0.024×10^{-3}	0.15×10^{-3}
$\delta\hat{SR}_{4}$	Satellite No. 4 Solar Radiation Force Uncertainty	m/sec^2	1.4×10^{-9}	1.8×10^{-9}	0.8×10^{-9}	1.8×10^{-9}
$\delta\hat{\underline{R}}_{G3}$	Monitor Station No. 3 Location Uncertainty	m	4, 10.7, 6.4	9	0.27, -0.12, -0.03	0.15, 0.24, 0.27
$\delta\hat{\phi}_{r3}$	Monitor Station No. 3 Clock Error	m	6.7	61	0.33	0.21
$\delta\hat{f}_{r3}$		mps	0.02×10^{-3}	3×10^{-3}	0.015×10^{-3}	0.02×10^{-3}
$\hat{x}_{fr3}$		mps	0.19×10^{-3}	0.16×10^{-3}	-0.015×10^{-3}	0.15×10^{-3}
$\delta\hat{\mu}$	Gravitational Uncertainty	m^3/sec^2	3.99×10^7	7.97×10^7	-0.55×10^7	7.62×10^7

145
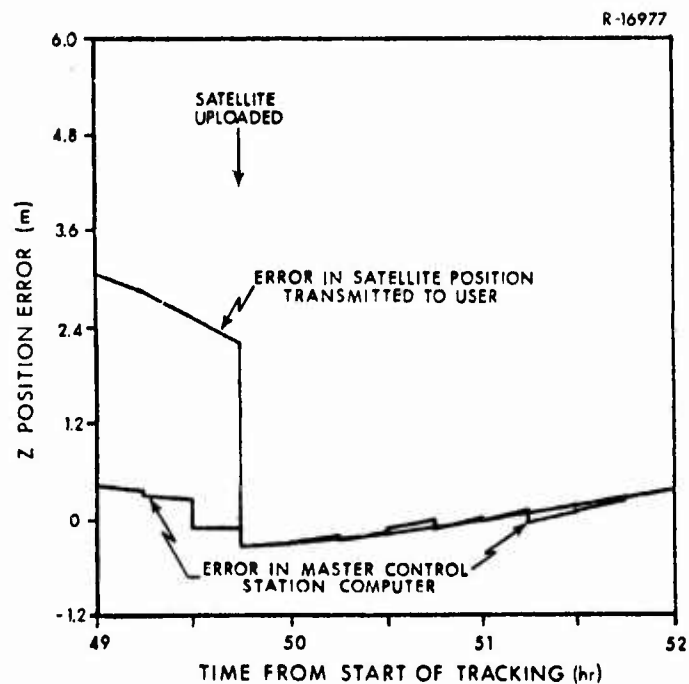
Figure B.3-14   Ground System Estimation and Satellite
Prediction Errors of Satellite No. 4
Z Position
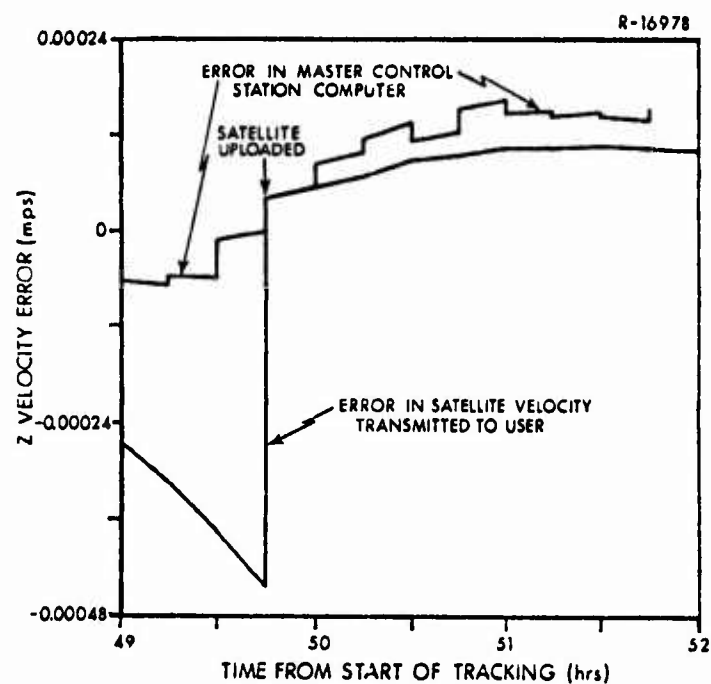
Figure B.3-15   Ground System Estimation and Satellite
Prediction Errors of Satellite No. 4
.Z Velocity

146

APPENDIX C

CLOCK ERROR MODELING

This appendix will summarize the basic approach taken in the modeling of the intrinsic stability of a time standard (clock); a more extensive treatment of this topic may be found in Ref. 3. Intrinsic stability is the characteristic behavior of the clock when it is operating in a benign environment. Thus, the model for intrinsic stability will provide a lower bound on the clock errors. Operation in a non-ideal environment will degrade the performance of the clock. A detailed discussion of environmentally-induced errors and their modeling is presented in Section 4.1.

C.1 FREQUENCY STABILITY

A clock or time standard is basically a frequency source coupled with a counter that accumulates the total elapsed phase as depicted in Fig. C.1-1. The performance of the time standard is directly related to the stability of the frequency source. Thus it is common to deal with frequency stability when discussing the performance of time standards. The following will consider a frequency source whose instantaneous output may be written as

$$V(t) = V_o \sin \left[2\pi f_o t + \delta\phi(t) \right] \qquad (C.1-1)$$

where it is assumed that the frequency fluctuations, $\delta\dot{\phi}(t)$ are very small, i.e.,

147
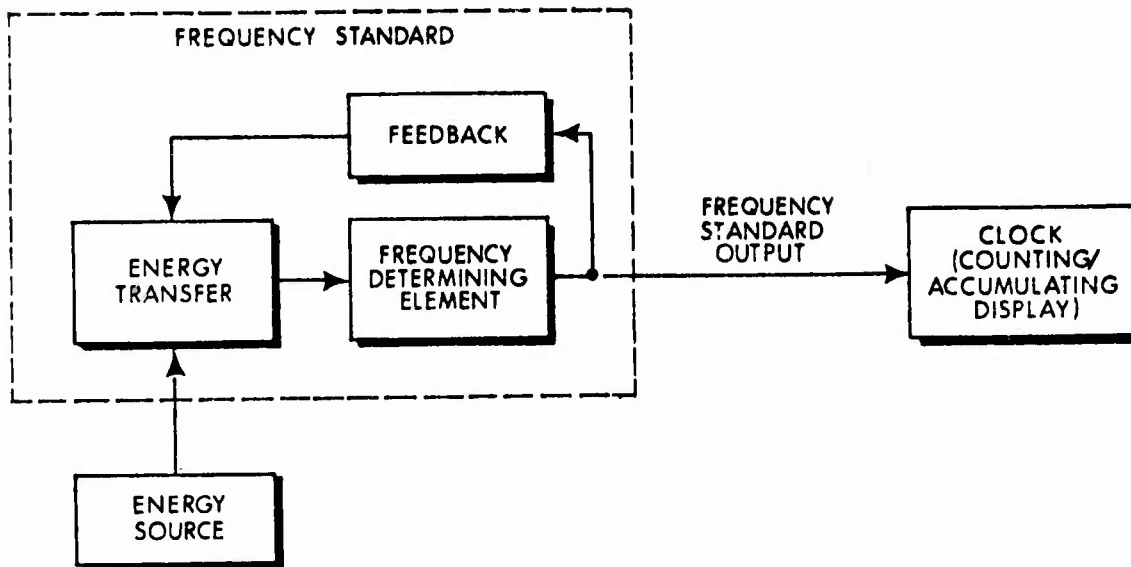
Figure C.1-1   Relationship Between a Frequency
Standard and a Clock

$$\left|\frac{\dot{\delta\phi}(t)}{2\pi f_o}\right| \quad << 1 \qquad\qquad (C.1-2)$$

The instantaneous phase, $\phi(t)$, is

$$\phi(t) = 2\pi f_o t + \delta\phi(t) \qquad\qquad (C.1-3)$$

with the instantaneous frequency

$$f(t) = f_o + \frac{1}{2\pi} \dot{\delta\phi}(t) \qquad\qquad (C.1-4)$$

The quantity of interest is the fractional frequency fluctuation $y(t) = \Delta f/f_o$ defined as

$$y(t) = \frac{f(t) - f_o}{f_o} = \frac{\dot{\delta\phi}(t)}{2\pi f_o} \qquad\qquad (C.1-5)$$

Two measures of frequency stability are now presented, one in the frequency domain and the other in the time domain. The frequency domain measure of frequency

148

stability is the two-sided power spectral density of the fractional frequency fluctuations, $S_y(\omega)$. The power spectral density may be defined as the Fourier transform of the autocorrelation function of $y(t)$ if it is assumed that $y(t)$ is stationary. This assumption has been verified in practice, hence

$$S_y(\omega) \equiv \int_{-\infty}^{\infty} R_y(\zeta)\ e^{-j\omega\zeta}\ d\zeta \qquad (C.1-6)$$

where

$$R_y(\zeta) = \underset{T \to \infty}{\text{Lim}}\ \frac{1}{2T} \int_{-T}^{T} y(t)\ y(t+\zeta)\ dt \qquad (C.1-7)$$

is the autocorrelation function of $y(t)$. (It has been implicitly assumed that both stationarity and ergodicity hold for Eq. (C.1-7) to be valid.) Equation (C.1-7) may also be written symbolically as

$$R_y(\zeta) = \left\langle y(t)\ y(t+\zeta) \right\rangle \qquad (C.1-8)$$

with $\langle \cdot \rangle$ denoting infinite time average.

The time domain measure of frequency stability most commonly used is the two-sample Allan variance defined as

$$\sigma_y^2(\tau) \equiv \left\langle \frac{(\bar{y}_{k+1} - \bar{y}_k)^2}{2} \right\rangle \qquad (C.1-9)$$

with

$$\bar{y}_k \equiv \frac{1}{\tau} \int_{t_k}^{t_k+\tau} y(t)\ dt, \qquad t_{k+1} = t_k+\tau, \quad k=0,1,2,\dots \qquad (C.1-10)$$

being the average fractional frequency fluctuation over the averaging interval .

It has been shown (Ref. 9) that a relationship exists between $S_y(\omega)$ and $\sigma_y^2(\tau)$ for a certain class of frequently encountered noise processes. If $S_y(\omega)$ is restricted to a power law spectral density, i.e.,

$$S_y(\omega) = \sum_{n=-1}^{2} h_n \, \omega_n \qquad 0 < \omega \leq \omega_h \qquad \text{(C.1-11)}$$

then conversions between $S_y(\omega)$ and $\sigma_y^2(\tau)$ are possible with the aid of the expressions given in Table C.1-1. The physical characteristics of the power law spectral density terms (with $-1 \leq n \leq 2$) are indicated in the table.

TABLE C.1-1

RELATIONSHIPS BETWEEN TIME AND
FREQUENCY DOMAIN STABILITY MEASURES

TYPE OF NOISE PERTURBING THE OSCILLATOR	SPECTRAL DENSITY OF FREQUENCY FLUCTUATIONS $S_y(\omega)$	TWO-SAMPLE ALLAN VARIANCE $\sigma_y^2(\tau)$
White Phase Noise	$h_2\, \omega^2$	$\dfrac{h_2\, 6\, \omega_h}{\tau^2}$
Flicker Phase Noise	$h_1|\omega|$	$\dfrac{h_1}{\tau^2}\left[9 + 6\ \ln(\omega_h\tau) - 2\ \ln 2\right]$
White Frequency Noise	h_o	h_o/τ
Flicker Frequency Noise	$h_{-1}/|\omega|$	$h_{-1}\ 4\ \ln 2$

$\omega_h \tau \gg 1$

These relationships between the time and frequency domain stability measures have direct application in time

150

standard error modeling. When time standard error models are expressed in state-space notation, the process noise in the model (see Table C.1-1) is characterized by its spectral level; i.e., the appropriate h-coefficient. For typical time standard applications, the low frequency terms (with $n \leq 0$) dominate and time domain stability measures (i.e., the Allan variance) are used exclusively. Hence, knowledge of $\sigma_y^2(\tau)$ for differing values of τ affords an estimate of the h_i.

The typical method of presenting time domain stability data is via a fractional frequency stability or "sigma-tau" plot. Figure C.1-2 is typical and will be utilized to obtain error model parameters for the example
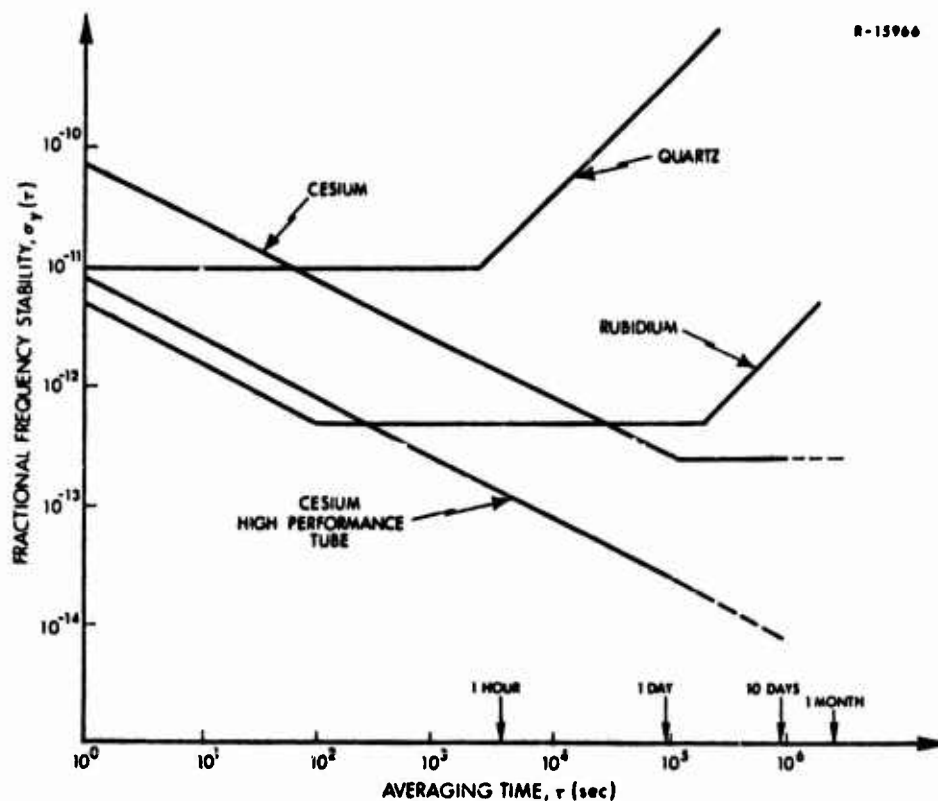

Figure C.1-2   Typical Fractional Frequency Stability Plot

151

quartz crystal oscillator, the Hewlett Packard (HP) 10544A.
From the figure, it can be seen that flicker frequency
noise($\sigma_y(\tau) \sim$ constant) is the dominant noise term for this
quartz oscillator. The portion of the quartz curve with
$\sigma_y(\tau) \sim \tau$ is indicative of "aging" in the device.

The preceding discussion is only a brief outline
of frequency stability; a more complete discussion may be
found in Refs. 3 and 9.

C.2 FLICKER NOISE MODEL

As noted in Section C.1, flicker noise is the dom-
inant error source for the quartz crystal oscillator under
consideration. This section will outline the development
of a model for flicker noise; Ref. 3 contains a more com-
prehensive derivation. The flicker noise model to be de-
veloped will be linear, for ease of inclusion in a Kalman
filter estimation algorithm or associated error covariance
analysis. It will also be an approximation since the ob-
served power spectral density ($1/|\omega|$) cannot be realized
exactly by a finite dimensional linear system. (Only power
spectral densitites which vary as even powers of ω can be
treated exactly.)

Since its most natural description is in the fre-
quency domain, the methodology outlined below will be to
attempt to approximate the power spectral density of flicker
noise ($S_y(\omega) = h_{-1}/|\omega|$) as closely as possible subject to
the constraint that only a finite dimensional linear sys-
tem may be used. The first step in the approximation is
to pass a known random process through a linear frequency
domain "shaping filter" to obtain the desired random pro-
cess (i.e., flicker noise). This requires the application
of a fundamental result of linear system theory.

152

Consider a time invariant linear system with output $y(t)$ and input $w(t)$, which is a sample function of a known random process. It can be shown that the power spectral densities of the input and output ($S_w(\omega)$ and $S_y(\omega)$, respectively) are related by Eq. (C.2-1),

$$S_y(\omega) = |G(j\omega)|^2 S_w(\omega) \qquad (C.2-1)$$

where $G(j\omega)$ is the system transfer function.

In this discussion it will be assumed that the input random process is white noise and the desired output process should approximate flicker noise $\left[\text{i.e.}, S_w(\omega) = q' = \text{constant and } S_y(\omega) \simeq h_{-1}/|\omega| \text{ over several decades of angular frequency, } \omega \right]$. From the above it is evident that the flicker noise model transfer function $G_F(j\omega)$ should satisfy:

$$|G_F(j\omega)|^2 = h_{-1}/(q'|\omega|) \qquad (C.2-2)$$

Equation (C.2-2) provides the characteristics of the shaping filter required to continue with the development of the flicker noise model. Since Eq. (C.2-2) cannot be realized exactly (it is not an even power of ω), an approximation is required. The approximation to Eq. (C.2-2) proposed by Barnes and Jarvis (Ref. 10) is now given.

Consider approximately Eq. (C.2-2) by the transfer function

$$G_F(j\omega) = G_o \prod_{i=1}^{N} \frac{j\omega + \alpha_i}{j(\omega/\beta) + \alpha_i} \qquad (C.2-3)$$

where $\alpha_{i+1} = \alpha_i/\beta^2$ and β is a constant less than unity. A log-log plot of Eq. (C.2-3) for the N-stage flicker noise model transfer function is given in Fig. C.2-1.

153
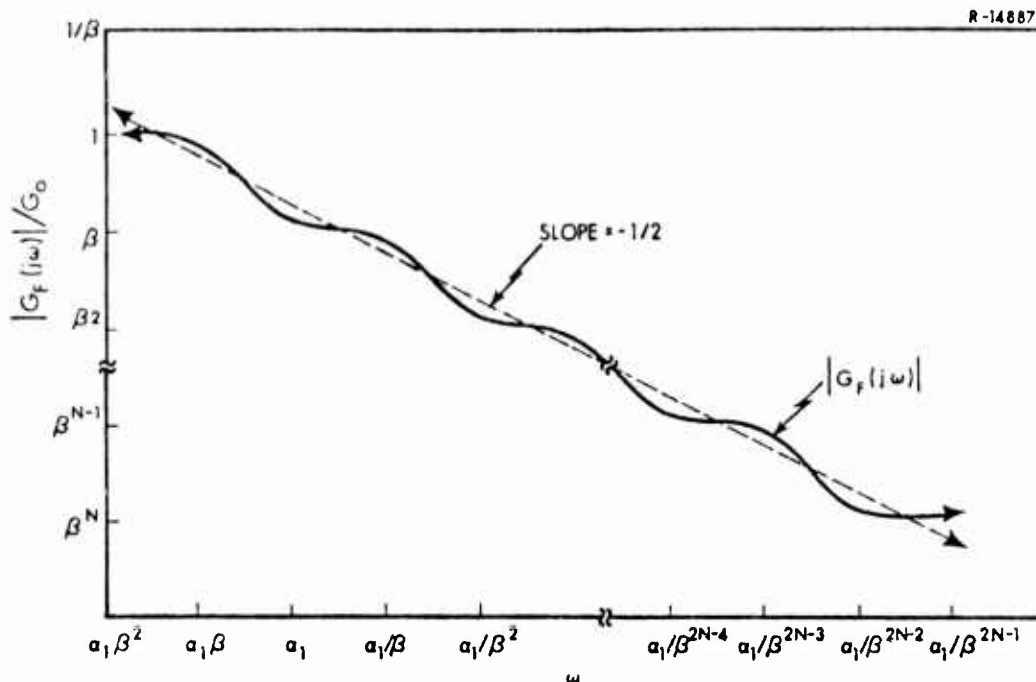
Figure C.2-1   General N-Stage Flicker Noise
Model Transfer Function

The transfer function of Eq. (C.2-3) has four dis-
tinct parameters which may be varied as requirements dic-
tage. α_1 locates the lower end of the frequency interval
(for a fixed β) over which the approximation is valid. This
can be seen by reference to Fig. C.2-1 in which the approxi-
mating interval is

$$\omega_\ell = \alpha_1 \ \beta^{3/2} < \omega < \alpha_1/\beta^{2N-3/2} = \omega_h \qquad (C.2-4)$$

The width of the approximation interval varies as β^{-2N}
while the precision of the approximation increases as β^2
tends toward unity. G_o adjusts the magnitude of the trans-
fer function to provide the correct flicker noise spectral
level. In any application, the choice of values for α_1, β,
N and G_o will characterize the flicker noise model.

154

For error modeling purposes, a time domain model for flicker noise is required. The transfer function of Eq. (C.2-3) can be associated with the differential system

$$(a_N D^N + \ldots + a_0) y = (b_N D^N + \ldots + b_0) w$$

(C.2-5)

where D^i is the differential operator, $D^i(\cdot) \equiv d^i(\cdot)/dt^i$. Equating the input-output transfer function of the system defined by Eq. (C.2-5) with the flicker noise model transfer function (setting $s = j\omega$) yields

$$G_F(s) = \frac{b_N s^N + \ldots + b_0}{a_N s^N + \ldots + a_0} = \prod_{i=1}^{N} \frac{s + \alpha_i}{(s/\beta) + \alpha_i}$$

(C.2-6)

The coefficients b_i and a_i can be obtained by equating

$$b_N s^N + \ldots + b_0 = \prod_{i=1}^{N} (s + \alpha_i)$$

(C.2-7)

and setting

$$a_i = b_i / \beta^i$$

(C.2-8)

The constant parameter G_o has been absorbed into the input term, w, for this discussion, that is,

$$E\left[w^2\right] \equiv q_f = q'\left|G_o\right|^2$$

(C.2-9)

Zadeh and Desoer (Ref. 11) give the realization shown in Fig. C.2-2 for Eq. (C.2-5). Typically, this time domain realization of the flicker noise approximation will be used as a noise input at the frequency level in a time standard error model. In this case, the output y is the

155
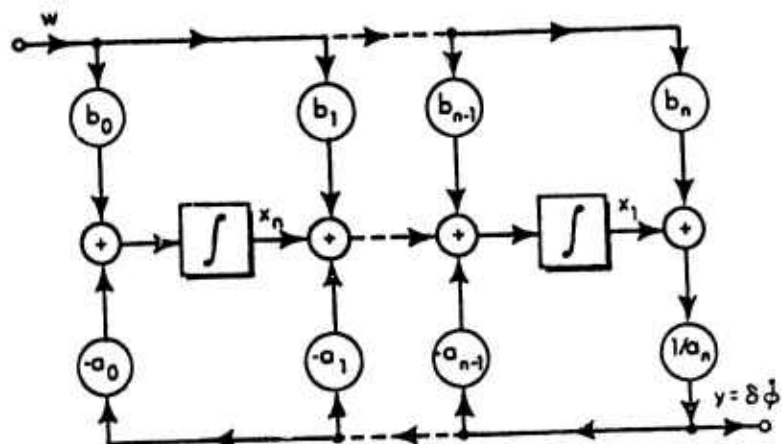
Figure C.2-2   Time Domain Realization of Flicker
Noise Transfer Function

input to the phase error ($\delta\phi$) integrator or

$$\dot{\delta\phi} = y$$

The state equations can then be written (with reference to
Fig. C.2-2) as

$$\dot{\underline{x}} = F \, \underline{x} + \underline{g} \, w \tag{C.2-10}$$

with

$$\underline{x} = \begin{bmatrix} \delta\phi \ x_1 \ldots \ x_N \end{bmatrix}^T \tag{C.2-11}$$

$$
F = \begin{bmatrix}
0 & 1/a_N & 0 & 0 & \cdots & 0 \\
0 & -a_{N-1}/a_N & 1 & 0 & \cdots & 0 \\
0 & -a_{N-1}/a_N & 0 & 1 & \cdots & 0 \\
\vdots & \vdots & \vdots & \vdots & \ddots & \vdots \\
0 & -a_1/a_N & 0 & 0 & \cdots & 1 \\
0 & -a_0/a_N & 0 & 0 & \cdots & 0
\end{bmatrix} \tag{C.2-12}
$$

and

$$\underline{g} = \frac{1}{a_N} \begin{bmatrix} b_N \\ a_N \, b_{N-1} - a_{N-1} \, b_N \\ a_N \, b_{N-2} - a_{N-2} \, b_N \\ \vdots \\ a_N \, b_0 - a_0 \, b_N \end{bmatrix}$$

(C.2-13)

C.3   MODELING OF INTRINSIC STABILITY

Intrinsic stability will be treated as the performance of the oscillator in an environmentally favorable (benign) situation.   In practice, it is common to maintain as favorable an environment as possible when measuring the fractional frequency stability of an oscillator (see Fig. C.1-2).   The two sources of error which arise for a quartz crystal oscillator in a benign environment are flicker noise and aging.

Aging is a nearly linear change in resonance frequency with time.   The a priori magnitude of this frequency drift cannot be determined.   However, by observing its effects over a long period of time (days), the aging rate can be measured.   This behavior can be adequately modeled as a random bias.   The maximum (3σ) aging rate for the HP 10544A is stated as 5.79×10^{-15}/sec.

In Section C.2, a model for flicker noise was developed.   The input to the model was white noise with a

157

spectral level, q_f, which is dependent upon the parameters of the model. If G_o in Eq. (C.2-3) is chosen such that

$$|G_F(j\omega)|^2 \simeq 1/|\omega| \tag{C.3-1}$$

then $q' = h_{-1}$ [from Eq. (C.2-2)] and q_f can be evaluated as

$$q_f = h_{-1}|G_o|^2 \tag{C.3-2}$$

In Ref. 3 it is shown that a choice of N=2, $\alpha_1 = 10^{-2}$ and $\beta = 10^{-1}$ results in a flicker noise model which is valid over the approximation interval

$$2 \text{ sec} \leq \tau < 2 \times 10^4 \text{ sec} \tag{C.3-3}$$

This interval is compatible with the observed flicker noise region. For Eq. (C.3-1) to be satisfied, with this choice of N, α_1 and β, requires that $|G_o|^2 = 3.16 \times 10^3$. Hence, the spectral level of the white noise driving the flicker noise model is calculated as

$$q_f = 3.16 \times 10^3 \, h_{-1} \tag{C.3-4}$$

A value for h_{-1} may be obtained from Table C.1-1 and Fig. C.1-2 as

$$h_{-1} = \frac{\sigma_y^2(\tau)}{4 \ln 2} = \frac{(1 \times 10^{-11})^2}{2.77} = 3.66 \times 10^{-23} \tag{C.3-5}$$

The state equations of the flicker noise model for the HP 10544A crystal oscillator are described by the state vector,

$$\underline{x} = \left[\delta\phi, \ x_{1_f}, \ x_{2_f} \right]^T \tag{C.3-6}$$

and the system matrices

$$F = \begin{bmatrix} 0 & f_1 & 0 \\ 0 & f_2 & 1 \\ 0 & f_3 & 0 \end{bmatrix} \qquad \text{(C.3-7)}$$

where

$$f_1 = 1.0 \times 10^{-2}$$
$$f_2 = -1.01 \times 10^{-1} \text{ sec}^{-1}$$
$$f_3 = -1.0 \times 10^{-4} \text{ sec}^{-2}$$

and

$$g = \begin{bmatrix} g_1 \\ g_2 \\ g_3 \end{bmatrix} \qquad \text{(C.3-8)}$$

where

$$g_1 = 1.0 \times 10^{-2}$$
$$g_2 = 9.09 \times 10^{-1} \text{ sec}^{-1}$$
$$g_3 = 9.90 \times 10^{-3} \text{ sec}^{-2}$$

The spectral level of the white driving noise is

$$q_f = 1.14 \times 10^{-19} \qquad \text{(C.3-9)}$$

APPENDIX D

PROPAGATION PATH MODELS

The propagation of radio frequency energy from a transmitter to a receiver both located close to the earth's surface is subject to many disturbances, most significant of which are the earth's surface and atmosphere. There are a number of mechanisms by which propagation of radio frequency energy can take place, but for the frequencies of interest in this report (L-band, 1.6 GHz), the primary mechanism is tropospheric waves.

Energy propagated via tropospheric waves travels between the transmitter and receiver within the earth's troposphere, which is that portion of the earth's atmosphere within 15 km of the surface. There are several paths that this wave can take between the transmitter and receiver, depending upon their separation. These paths lie in two regions: within line-of-sight and beyond line-of-sight.

The energy loss in the propagation of radio waves is the subject of this appendix. In particular, models of energy loss along the various propagation paths (path losses) that were used in the development of the results in Section 3.1.3 are discussed. Models of these losses within line-of-sight are discussed in Section D.1 while those for beyond line-of-sight are discussed in Section D.2. In addition, a model of path loss common to both regions is discussed in Section D.3. A typical example of propagation path energy loss using these models is presented in Section D.4.

D.1 WITHIN LINE-OF-SIGHT

If the transmitter and receiver are within line-of-sight of each other, then the radio wave can travel two paths. One is the direct path between the transmitter and the receiver, while the other is a result of reflection from the earth's surface. Models of these two paths are presented below.

D.1.1 Direct Path

The loss in energy through the direct path is due to spreading of the energy over an ever-increasing (with distance) spherical surface area. This is also called the inverse square distance loss or free space loss. This loss is if modeled as follows (Ref. 15):

$$L_d = \left(\frac{\lambda}{4\pi d}\right)^2 g_t g_r \qquad\qquad (D.1-1)$$

where

L_d is the direct path loss

λ is the wavelength of radio wave

d is the distance between the transmitter and receiver antennas in same units as λ

g_t is the transmitter antenna gain in direction of receiver

g_r is the receiver antenna gain in direction of transmitter

This is the only loss that would be present in free space, where there are no objects to reflect the radio wave or otherwise influence it. This is the basic loss to which the other losses due to reflections, etc., discussed below are referenced.

D.1.2 Reflected Path

When either the transmitter or receiver is close to the earth's surface, the wave will be reflected by the earth as illustrated in Fig. D.1-1. The loss, L_r, in this reflected path relative to the free space loss is modeled as follows (Ref. 29):

$$L_r = \left[2 \sin \left(\frac{2\pi \, h'_r \, h'_t}{\lambda d} \right) \right]^2 \qquad (D.1-2)$$

where

h'_t is the <u>effective</u> height of the transmitter antenna above the reflecting plane.

h'_r is the <u>effective</u> height of the receiver antenna above the reflecting plane.

This model assumes the earth has a perfectly smooth surface for reflection. The reflecting plane is tangent to the earth's surface at the point of reflection. It is important to note the distinction between <u>effective</u> antenna heights used in Eq. (D.1-2) and actual values. Near the horizon, the actual values may differ significantly from the effective values.
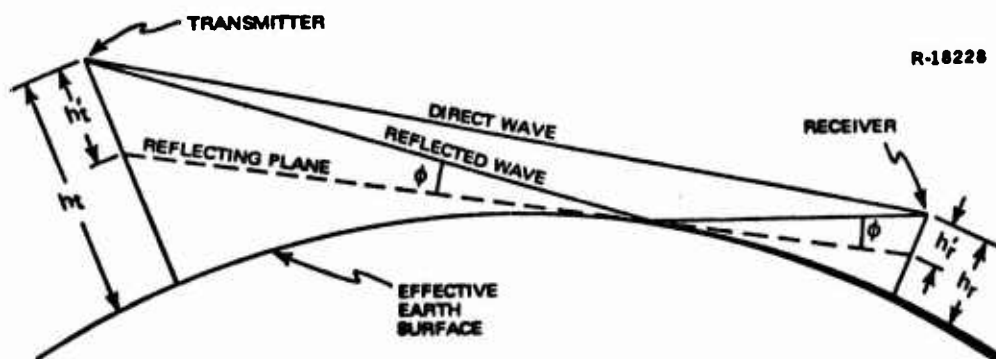

Figure D.1-1   Line-of-Sight Propagation

The path of a radio wave is bent as it passes through the atmosphere. In order to be able to represent these paths as straight lines, an "effective earth's radius" is used in the computations of effective antenna heights. This effective earth's radius is a function of antenna height and the earth's surface refractivity (zero altitude) as follows (Ref. 30):

$$a = a_o \left[1 + \frac{a_o}{n(h)} \frac{\partial n(h)}{\partial h} \right]^{-1} \qquad (D.1-3)$$

$$n(h) = 1 + N_S \exp \left[- 0.139\ h \right] \qquad (D.1-4)$$

where

a is the effective earth radius in km

a_o is the actual radius of the earth in km

N_S is the earth's surface refractivity (300×10^{-6})

h is the height of the lowest antenna in km

The reflected wave causes reinforcement of the direct wave, accounting for the factor of two in Eq. (D.1-2). Partial cancellation may also occur, especially where the separation between transmitter and receiver antennas in relation to their heights, is not large. These effects will be illustrated in Section D.4.

D.2 BEYOND LINE-OF-SIGHT

If the transmitter and receiver are beyond the line-of-sight relative to one another, the direct and reflected waves do not exist. However, some energy is propagated beyond line-of-sight by the phenomenon of diffraction and by scattering of the radio waves in the upper troposphere, usually identified as tropospheric scatter or forward scatter.

Models of the losses occurring in these two paths are presented in the sections below.

D.2.1 Diffraction Loss

Radio waves are bent around the earth by the phenomenon of diffraction. This phenomenon occurs when the direct path of the radio wave approaches tangency to the earth's surface. The effect of diffraction around the earth's curvature is to make possible transmission of radio waves to well beyond the horizon, but with an additional loss relative to free-space loss. This additional loss or attenuation, called diffraction loss, depends upon the separation and heights of transmitter and receiver antennas, electromagnetic ground constants, earth radius, the radio frequency and polarization of the radio wave. No simple relation exists which expresses diffraction loss in these various factors. Available data is empirical (Ref. 29). The diffraction loss computations for this study assumed a smooth earth surface, horizontal wave polarization and average earth surface properties (i.e., $\varepsilon = 15$, $\sigma = 0.005$ mhos/m). Diffraction loss was assumed to start at the line-of-sight separation, which is standard practice in propagation loss calculations, providing a smooth transition across the line-of-sight boundary.

D.2.2 Tropospheric Scatter

Well beyond the horizon, a propagation path between a transmitter and receiver can exist due to scattering of the radio wave by atmospheric turbulence or incoherent reflections in the upper troposphere. This propagation mode is usually termed forward scatter or tropospheric scatter. The quantity of energy propagated in this mode is small

164

relative to free-space propagation, and subject to large
variations with time. Again, no simple equation relating
this forward scatter characteristic[*] to the various factors
of influence is available. However, a long-term median trans-
mission loss due to forward scatter can be computed based on
empirical data (Ref. 29).

For propagation paths extending only very slightly
beyond line-of-sight, diffraction will be the dominant propa-
gation mechanism and scattering can be neglected. Conversely,
for long paths, the diffraction field may be much weaker than
the scattered field, and thus the diffraction mechanism can
be neglected. In intermediate cases, both mechanisms have
to be considered and the results combined as discussed in
Ref. 29.

D.3 ATMOSPHERIC ATTENUATION

At the GPS navigation signal frequencies (L-band,
1.6 GHz), attenuation of the radio waves due to absorption
or scattering by constituents of the atmosphere and by par-
ticles in the atmosphere may be significant. At these fre-
quencies, the attenuation is due mainly to water vapor and
oxygen. This atmospheric absorption attenuation or loss
relative to free space loss is given by (Ref. 29)

$$L_a = 10^{0.009\,d} \qquad\qquad (D.3\text{-}1)$$

where

    L_a is the atmospheric loss relative to free space

    d is the distance between transmitter and
       receiver in km.

---

[*]Hereafter referred to as a loss relative to free space loss.

This loss occurs throughout the troposphere and thus is included in all propagation path loss computations for this study. Note that at 100 km, this atmospheric attenuation is less than 1 dB, but at 1000 km it is 9 dB.

D.4 PROPAGATION PATH LOSS

The total loss in transmitted energy of a radio wave is the product of the losses in the various paths that the wave can follow. It is standard practice to express this loss in decibels; thus, the total loss is expressed as the sum of the individual path losses, each expressed in dB. The free space propagation path loss is the basic loss to which all other losses discussed in this appendix are referenced. That is, these other losses (i.e., reflected, diffraction, scatter and atmospheric attenuation) occur in addition to the basic direct loss.

Within line-of-sight, the total propagation path loss in dB is

$$L_p = L_d + L_r + L_a \qquad dB \qquad (D.4-1)$$

where

L_p is the total propagation path loss in dB

L_d is direct wave or space loss in dB [Eq. (D.1-1)]

L_r is the reflected wave loss in dB [Eq. (D.1-2)]

L_a is the atmospheric attenuation in dB [Eq. (D.3-1)]

Beyond line-of-sight, the total propagation path loss is

$$L_p = L_d + L_{diff} + L_{fs} \qquad dB \qquad (D.4-2)$$

166

where

> L_{diff} is the diffraction loss (relative to
> free space loss) in dB
>
> L_{fs} is the forward scatter loss (relative
> to free space loss) in dB

As discussed in Section D.2.2, the values of the diffraction
loss and forward scatter loss are complex functions of
transmitter-receiver separation, expressed empirically.

      A typical propagation path loss curve is illus-
trated in Fig. D.4-1. The top of this curve is +6 dB above
the free space loss, reflecting the factor of two in Eq.
(D.1-2); that is, the reinforcement of the direct wave by
the reflected wave. The "spikes" are the result of the par-
tial cancellations discussed earlier. The propagation path
loss results presented in Section 3.1.3 (i.e., Fig. 3.1-1)
are worst case in that the minimum loss is used, which is
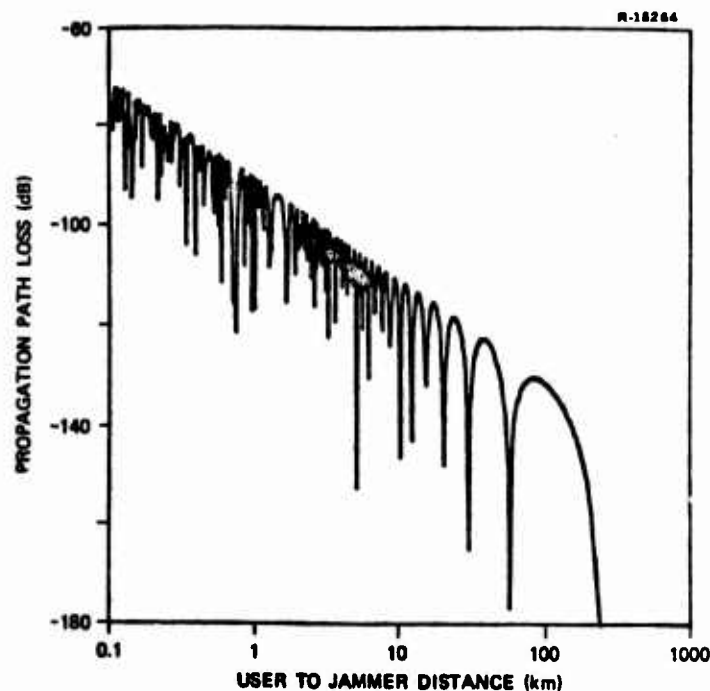the top part of the curve in Fig. D.4-1.

Figure D.4-1   Typical Propagation Path Loss

167

REFERENCES

1. Pyle, R.H. and Roy, K.J., "Investigation of the Performance of Army Users of the NAVSTAR Global Positioning System," The Analytic Sciences Corporation, AFAL-TR-74-294, November 1974.

2. Duiven, E.M. and LeSchack, A.R., "Global Positioning System Simulation Development and Analysis," The Analytic Sciences Corporation, TR-428-2, December 1974.

3. Mealy, G.L., "Sensor Data Bank Development: Time Standard Error Models and Data File," The Analytic Sciences Corporation, AFAL-TR-75-65, June 1975.

4. Hellwig, H., "Atomic Frequency Standards: A Survey," Proc. IEEE, Vol. 63, February 1975, pp. 212-229.

5. Gelb, A., Ed., Applied Optimal Estimation, M.I.T. Press, 1974.

6. Osterdock, T., Private communication on October 21, 1974, with Gregory L. Mealy, concerning the perfomance of the Hewlett Packard 10544A crystal oscillator.

7. Hafner, E., Private communication on March 6, 1975, with Gregory L. Mealy, concerning performance of crystal oscillators.

8. D'Appolito, J.A., "The Evaluation of Kalman Filter Designs for Multisensor Integrated Navigation Systems," The Analytic Sciences Corporation, AFAL-TR-70-271, January 1971.

9. Barnes, J.A., et al., "Characterization of Frequency Stability," IEEE Transactions on Instrumentation and Measurement, Vol. 20, May 1971, pp. 105-120.

10. Barnes, J.A. and Jarvis, S., Jr., "Efficient Numerical and Analog Modeling of Flicker Noise Processes," National Bureau of Standards (U.S.) Technical Note 604, June 1971.

REFERENCES (Continued)

11. Zadeh, L.A. and Desoer, C.A., *Linear System Theory: The State Space Approach*, McGraw-Hill Book Co., 1963.

12. Kraus, J.D., *Antennas*, McGraw-Hill Book Co., August 1950.

13. Kraus, J.D., *Radio Astronomy*, McGraw-Hill Book Co., 1966.

14. Potter, P.D., "Antennas" in *Space Communication*, A.V. Balakrishnan, ed., McGraw-Hill Book Co., 1963.

15. Jasik, H.J., ed., *Antenna Engineering Handbook*, McGraw-Hill Book Co., 1961.

16. Widrow, B., Mantey, P.E., Griffiths, L.J., and Goode, B.B., "Adaptive Antenna Systems," *Proc. IEEE*, Vol. 55, December 1967, pp. 2143-2159.

17. Tuteur, F.B., "The Optimum Detector for Nonisotropic Noise," General Dynamics/Electric Boat Research Progress Report No. 38, September 1968.

18. Van Trees, H.L., "Notes on Array Processing," M.I.T., July 1971.

19. Reinhard, K.L., "Adaptive Antenna Arrays for Coded Communications Systems," Ohio State University Research Foundation, RADS-TR-74-102, May 1974.

20. Mayhon, J.T. and Ricardi, L.J., "Physical Limitations on Interference Reduction by Antenna Pattern Shaping," M.I.T. Lincoln Laboratory, Technical Note 1974-34, June 1974.

21. Shor, S.W.W., "Adaptive Technique to Discriminate Against Coherent Noise in a Narrow-Band System," *J. Acoust. Soc. Am.*, No. 39, January 1966, pp. 74-78.

22. Roberts, E.L., et al., "Automatic Steerable Null Antenna Processor," Martin-Marietta Aerospace, ECOM-0061-1, August 1974.

23. Roberts, E.L., et al., "Steerable Null Antenna Processes," Martin-Marietta Aerospace, ECOM-0206-1, August 1974.

REFERENCES (Continued)

24. "User System Segment for the NAVSTAR Global Position-
    ing System, Phase I," U.S. Air Force Space and Missile
    Systems Organization, SS-US-101B, Code ID07868,
    30 September 1974.

25. Wozencraft, J.M. and Jacobs, I.M., Principles of Com-
    munications Engineering, Wiley and Sons, New York,
    1965.

26. Spilker, J.J. Jr., et al., "Defense Navigation Satel-
    lite Special Study — Final Report," Stanford Tele-
    communications, Inc., SAMSO TR-74-92, April 1974.

27. Cahn, C.R., et al., "TIMATION Modulation Study,"
    Magnavox Research Laboratories, Report No. R-4439,
    August 1972.

28. "System Specification for the Global Positioning
    System, Phase I," U.S. Air Force Space and Missile
    Systems Organization, SS-GPS-101B, Code ID 07868,
    1 July 1974.

29. Rice, P.L., et al., "Transmission Loss Predictions
    for Tropospheric Communications Circuits," NBS,
    TN-101, May 1965.

30. Bean, B.R. and Thayer, G.D., "Models of the Atmos-
    pheric Radio Refractive Index," Proc. IRE, Vol. 47,
    No. 5, May 1959, pp. 740-755.

31. Duiven, E.M., "NAVSTAR Global Positioning System
    User Performance Study Results," The Analytic Sciences
    Corporation, Report No. TR-428-5, 1 May 1975.

32. Brammer, R.F., Himes, J.G., and Shields, J.D., "Evalu-
    ation of GPS Tactical Missile Guidance," The Analytic
    Sciences Corporation, Report No. TR-625-2, 30
    September 1975.